

Development of Machine Vision Based Workstation for Laser Micromachining

SATVIK JAGADEESH

A Thesis

in

The Department

of

Mechanical, Industrial and Aerospace Engineering

Presented in Partial Fulfilment of the Requirements for the Degree of Master of Applied Science
(Mechanical Engineering) at

Concordia University

Montreal, Quebec, Canada

May 2018

© Satvik Jagadeesh, 2018

Concordia University

School of Graduate Studies

This is to certify that the thesis prepared

By: Satvik Jagadeesh

Entitled: "Development of Machine Vision Based Workstation for Laser Micromachining"

and submitted in partial fulfilment of the requirements for the degree of

Master of Applied Science (Mechanical Engineering)

Complies with the regulations of the University and meets the accepted standards with respect to originality and quality.

Signed by the final Examining Committee:

_____ Chair

Dr. T. Kwok

_____ Examiner

Dr. A. Bhowmick

_____ Examiner

Dr. J. Dargahi

_____ Supervisor

Dr. S. Narayanswamy

Approved by _____

Chair of Department or Graduate Program Director

_____ 2018

Dean of Faculty

ABSTRACT

Development of Machine Vision Based Workstation for Laser Micromachining

Satvik Jagadeesh

Today, laser based micromachining technologies enable the most advanced material manufacturing. Since it has wide range of applications in Microelectronics, medical device, aerospace etc., the accuracy of the process is of utmost significance. The current project proposes a machine vision assisted workstation for laser micromachining. The machine vision system not only has the ability to control the Laser path but also has the ability to locate the starting point of machining. The system was designed and developed from basic components, while MATLAB was used to control the laser direction, and to image the specimen.

To analyse the limitations of the developed system, a rectangular shape was machined. Subsequently, known magnitudes of translational and rotational movements were given to the specimen. The images of machined area were captured before and after transformation. MATLAB algorithm was used to process the images to find the initial point of machined area on the transformed specimen. The laser beam is then guided to that point and the machining is repeated. The specimen was measured under microscope to find the error between the former and latter machined paths. Translational and angular errors were measured for various transformations.

In this study, the challenges and corresponding possible solutions that are encountered in machining complex geometries are addressed. The study proposes mathematical function based and image processing based algorithms to find the machining coordinates and function-based approach was found to be more efficient for complex geometries. Furthermore, the effect of process parameters on the overall quality of the manufacturing are discussed. The COMSOL software was used to model all the effect of laser parameters on the roughness, depth and thickness of machined path. To validate the numerical model, experiments were conducted for different process parameters the results are in good agreement with a simulation results.

The simulated model can be used to estimate the effect of the process parameters before the machining. Since the laser beam can be controlled on the geometry of the specimen and the study demonstrates the minimum possible error, this system can be applied to manufacture and repair wide range of microstructures.

Acknowledgements

I would sincerely express my gratefulness to Dr. Sivakumar Narayanswamy, my supervisor, and advisor, whose diligent encouragement, constant financial support, unfaltering faith and friendship have been an important part of my research throughout my graduate studies at Concordia University.

I extend my deepest thanks to my uncle Dr. Puttaswamy Manjunath for his continuous support and motivation that I have always been garnering. This accomplishment would not have been possible without him.

I am thankful and appreciate my fellow graduate student Mr. Hamid Ebrahimi Orimi for his continuous encouragement, as well as unselfish willingness to help me in the technical issues related to my project. I also like to thank my fellow graduate student Mr. Vinodh Krishna Carlapatti for his support during hard times and for his valuable suggestions for shaping my thesis.

Finally, I must express my very profound gratitude to my parents and brother for providing me unfailing support and continuous encouragement throughout my years of study. Thanks to all the people who have been with me from start to end of my thesis.

Table of Contents

ABSTRACT.....	iii
Acknowledgements.....	iv
List of figures.....	vii
List of tables.....	xi
Nomenclature.....	xii
Chapter 1. Introduction.....	1
1.1 What is Machine vision?.....	2
1.2 Evolution of Machine vision:.....	2
1.3 Techniques related to machine vision;.....	5
1.3.1 Image processing.....	6
1.3.2 Computer graphics.....	6
1.3.3 Pattern recognition.....	7
1.3.4 Artificial intelligence.....	7
1.4 Components of machine vision.....	7
1.4.1 Camera:.....	7
1.4.2 Camera Software.....	8
1.4.3 Optics.....	8
1.4.4 Lighting.....	9
1.5 Different types of machine vision:.....	12
1.5.1 1D Vision system.....	13
1.5.2 2D Vision system:.....	13
1.5.3 3D Systems:.....	15
1.6 Resolution and accuracy requirements.....	18
1.7 Different applications of Machine vision.....	20
1.8 Laser based Manufacturing.....	23
1.8.1 Properties of the laser.....	23
1.8.2 Types of lasers used for manufacturing.....	24
1.8.3 Laser micromachining.....	25
1.9 Machine vision in laser based manufacturing.....	29
1.10 Problem Identification and motivation.....	33

1.11	Objectives and scope.....	33
1.12	Organisation of the thesis.....	34
1.13	Summary	35
Chapter 2.	Materials and Methods.....	36
2.1	Laser	36
2.2	Opto Mechanical Components.....	36
2.3	Camera and lens	39
2.4	Silicon wafer	40
2.5	Software for control	40
2.6	Interferometer.....	40
2.7	Experimental Setup	40
2.8	Design of experiments.....	45
2.9	Summary	47
Chapter 3.	Preliminary Results and Analysis of Errors.....	49
3.1	Angular shift.....	50
3.2	Translational Shift.....	51
3.3	Error reduction strategies	55
3.4	Summary	56
Chapter 4.	Coordinate Extraction of Curved Shapes.....	58
4.1	Function based approach:.....	58
4.2	Image based approach	60
4.3	Experimental results.....	62
4.4	Summary	66
Chapter 5.	Texturing complex geometry – Experiments and Simulation	68
5.1	Finite element simulation	68
5.2	Physics explanation	69
5.3	Experimental results.....	70
5.4	Simulation results.....	78
5.5	Summary	81
Chapter 6.	Conclusion and Future Works	82
6.1	Conclusion.....	82
6.2	Future Works.....	83
References	85

List of figures

Figure 1.1 Evolution of Machine vision	3
Figure 1.2 Examples of computer vision algorithms from 1970s (a) line labelling (b) articulated body model (c) optical flow (d) intrinsic images[2]	4
Figure 1.3 Examples of computer vision algorithms from the 1980s (a) pyramid blending (b) shape from shading[2].....	4
Figure 1.4 Examples of computer vision algorithms from the 1990s (a) face tracking (b) image segmentation[2].....	5
Figure 1.5 (a) face Recognition (b) multi-view reconstruction [2].....	5
Figure 1.6 Recent examples of computer vision algorithms (a) Image-based modelling (b) Tone mapping[2].....	6
Figure 1.7 (a) Feature-based recognition (b) Region-based recognition [2]	7
Figure 1.8 Back lighting[3].....	9
Figure 1.9 Axial Diffuse lighting[3]	10
Figure 1.10 Structured light[3]	10
Figure 1.11 Dark field illumination[3].....	11
Figure 1.12 Bright-field illumination[3].....	11
Figure 1.13 Diffused dome lighting[3]	12
Figure 1.14 Strobe light used in high speed inspections[4]	12
Figure 1.15 1D vision system[5].....	13
Figure 1.16 Area scan system[6]	14
Figure 1.17 Line scan system[7].....	14
Figure 1.18 Passive 3D imaging[5]	15
Figure 1.19. Single camera with structured lighting[5]	16
Figure 1.20 Comparison of Analog and digital camera[8]	18
Figure 1.21 Comparison of different camera interfaces[8].....	18
Figure 1.22 Framework of the strip glove system[9].....	20
Figure 1.23 Digital images and corresponding intensity profiles from (a) sample 1 with a new tool, and (b) sample 2 with a worn tool[12].....	21

Figure 1.24 Photogrammetric measurement of type B pilot case: optical markers, reference crosshead and reference bars[14].....	22
Figure 1.25 a) Fresh tool Image b) Tool with region of interest c) Tool status as seen under machine vision[17] 23	
Figure 1.26 Schematic showing the operating principle of a Q-switch in a solid-state laser[18].	25
Figure 1.27 Coloured aluminium produced by femtosecond laser pulses. (a) Photograph of the gold aluminium; the gold appearance is independent of viewing angle. (b)– (d) SEM images showing micro- and nano-scale structural features of the gold aluminum.[20]	26
Figure 1.28 CO ₂ laser-induced peeling of glass strips from a borosilicate slide[38].	28
Figure 1.29 Freeform stainless steel sheet work-piece with a laser mark[43].....	29
Figure 1.30 The school badge marked and Marked numerals on the eggshell [44]	29
Figure 1.31 A view of the building chamber of the SLM system prototype used for the experimental activity; (b) side view of the IR camera setup[46].....	30
Figure 1.32 Schematic of the measurement system setup[47].....	31
Figure 1.33 Experimental setup for laser machining and depth measurements[50].....	32
Figure 1.34 Stereo vision laser galvanometric scanning system[52].....	32
Figure 2.1 Temporal profile of the laser power[53]	36
Figure 2.2 Laser micromachining experimental setup.....	37
Figure 2.3 Schematic of the Laser micromachining set up[54]	38
Figure 2.4 Schematic of the scanning length associated with the galvo mirror rotation[53]. .	38
Figure 2.5 Wyko NT1100 Optical Profiling System[55].....	41
Figure 2.6 Schematic of the mc-Si samples textured under three different overlap values, (a) 0%; (b) 30%; and (c) 60%.....	42
Figure 2.7 X and Y DC motors voltages to machine 3mm circle with 30 percent overlap	43
Figure 2.8 Experimental set up for machine vision	44
Figure 2.9 Servomotor and the sample holder	44
Figure 2.10(a) Sample before rotation (b) Sample rotated 30 degrees	46
Figure 3.1 Measured 4mmX8mm sample for errors.....	49
Figure 3.2 Angular errors Vs Angle of rotation of 4mmX8mm sample.....	50
Figure 3.3 Translation Errors Vs Angle of rotation of 4mmX8mm sample.....	51

Figure 3.4 Measured 4mmX6mm sample for errors.....	52
Figure 3.5 Distance moved in X Direction Vs Angular errors	53
Figure 3.6 Distance moved in X direction Vs Translation errors	53
Figure 3.7 Distance moved in Y direction Vs Angular errors	54
Figure 3.8 Distance moved in Y direction Vs Translation errors	55
Figure 3.9 Focussed and out of focus images	56
Figure.4.1 Microfluidic channel without interpolation.....	58
Figure 4.2 Schematic of the developed algorithm for curved shapes	59
Figure.4.3 Equidistant points after interpolation	60
Figure.4.4. Image based coordinate extraction	61
Figure.4.5 Irregularities in the extracted curves	61
Figure 4.6 Machined circle of 4mm diameter with zero overlap.....	62
Figure 4.7 Sine wave with a magnified section	62
Figure 4.8 Coordinates of the circle - Function based approach (a) & Image based approach (b) with 60% overlap	63
Figure 4.9 Interferometry images of the Sine curve - Function based approach (a) & Image based approach (b) with 60% overlap.....	63
Figure 4.10 Machined microfluidic channel in Image based approach with zero overlap.....	64
Figure 4.11 Machined microfluidic channel in function based approach with zero overlap....	64
Figure 4.12 Sinusoidal function in Function based approach with (a) 0% overlap (b) 30% overlap and (c) 60% overlap	65
Figure 4.13 Sinusoidal function in Image based approach with (a) 0% overlap (b) 30% overlap and (c) 60% overlap.....	65
Figure 4.14 Roughness vs percentage of overlap for Circle.....	66
Figure 4.15 Roughness vs percentage of overlap for Sinusoidal function	66
Figure 5.1. Adaptive mesh close to the laser spot at 3 microseconds.....	70
Figure 5.2 Roughness (Ra) Vs Laser power in (W) for different percentage X overlaps at 10 KHz	71
Figure 5.3 Roughness (Ra) Vs Laser power in (W) for different percentage Y overlaps at 10 KHz	72

Figure.5.4.Roughness (Ra) Vs Laser power in (W) for different percentage XY overlaps at 10 KHz	72
Figure 5.5 Roughness (Ra) Vs DAQ frequency in (Hz) for different percentage X overlaps at 4.8 W laser power	73
Figure 5.6 Roughness (Ra) Vs DAQ frequency in (Hz) for different percentage Y-overlaps at 4.8 W laser power	74
Figure.5.7 Roughness (Ra) Vs DAQ frequency in (Hz) for different percentage XY-overlaps at 4.8 W laser power	74
Figure 5.8 Interferometric image data for different DAQ frequency with 0% overlap with Laser power at 3.68W	75
Figure 5.9 Interferometric image data for different laser powers with 0% overlap at 10 KHz DAQ frequency.....	76
Figure 5.10 Depth (μ) Vs DAQ frequency in (Hz) for different percentage X overlaps at 3.68 W laser power	76
Figure 5.11 Depth (μ) Vs DAQ frequency in (Hz) for different percentage X overlaps with DAQ frequency at 10 KHz	78
Figure 5.12. 2D Axisymmetric simulation result for 2 KHz and 4.8 W laser power	79
Figure 5.13 2D simulation results of 0 overlap for 10 KHz and 4.8 W laser power	79
Figure 5.14. Experimental results of 0 overlap for 10 KHz and 4.8 W laser power	80
Figure 5.15 Simulation result for depth with 1 KHz sampling rate of laser at 4.87W, 0% overlap	80

List of tables

Table 2.1 List of experiments and the variables	48
Table 5.1 The depth of machined area for three different sampling rates from the experiment and simulation.....	80
Table 5.2 The depth of machined area for three different power from the experiment and simulation with DAQ frequency at 10 KHz	81

Nomenclature

f	Focal length of lens	mm
λ	Wavelength of the laser	nm
D	Diameter of laser before the lens	mm
d	Laser spot diameter	μ
φ	Rotation angle of the galvomirror.	degree
L	Length of laser scan	mm
α	Galvo scanner motor angle in x direction	degree
β	Galvo scanner motor angle in y direction	degree
O_v	Overlap	--
Op	Overlap percentage	--
Q	Heat flux	Wm^{-2}
k	Thermal conductivity	$WK^{-1}m^{-1}$
ρ	Density	$kg.m^{-3}$
Cp	Specific heat capacity	$Jkg^{-1}K^{-1}$
A	Cross section area of the material	mm^2
T	Temperature	K
x	Distance between the heat sources	mm
X_0	Laser spot position	mm
v	Surface normal velocity	$m.s^{-1}$
H_s	Enthalpy of sublimation	$Wm^{-2}K^{-1}$
h	Plank's constant	m^2kgs^{-1}

Chapter 1. Introduction

The implementation and usage of industrial automation is undergoing major and rapid changes. This change is driven by the need for industry both to remain competitive in their cost structure and to increase the levels of quality and consistency in the products that are produced. The drive towards increased productivity and improvement of quality in the manufacture of industrial products has led to great efforts to match the manufacturing equipment to these requirements. Whereas material processing has been rationalized in a primary phase, current efforts are mainly concerned with the following areas: Visual inspection, Process control and monitoring, Handling and assembly.

There are many possible uses for image sensors in these areas. The sensors' tasks range over a wide area and within different fields of application. The opportunities for the use of image processing are especially good in the processes in which human performance as regards speed, reliability, objectivity and accuracy are insufficient, and where technical and organizational alternatives lead to essentially higher expense. This aspect applies in the case of visual inspection because of unreliability and lack of objectivity of the human inspector. Another important factor, which makes the use of vision systems almost unavoidable, is high-speed production, which does not permit a human check in process real time.

Today, industries can implement automation at a reasonable price, through advances in sensor technology, networking capabilities, microprocessor design, open architecture for machine controls, Internet applications in machine control, and standardized software. During the past few years, the acquisition cost of vision inspection systems has dropped to levels that permit most companies to purchase and implement the systems. In addition, with the advent of faster computer processors, the vision system is software controlled, and thus the applications are increased. Vision systems provide means by which continuous and total autonomous inspection can be achieved during production. Today's vision systems can easily control guidance of automated manufacturing support components such as robots, as well as interface to sensors and output to auxiliary devices.

1.1 What is Machine vision?

“Machine vision is concerned with the automatic extraction, analysis and understanding of useful information from a single image or a sequence of images. It involves the development of a theoretical and algorithmic basis to achieve automatic visual understanding.” - The British Machine Vision Association and Society for Pattern Recognition.[1] According to the Automated Imaging Association (AIA), machine vision encompasses all industrial and non-industrial applications in which a combination of hardware and software provide operational guidance to devices in the execution of their functions based on the capture and processing of images. Though industrial computer vision uses many of the same algorithms and approaches as academic/educational and governmental/military applications of computer vision, constraints are different.

The main aim of a machine vision system is to generate a model of the real world from images. Since images are two-dimensional projections of the three-dimensional world, the information is not directly available and must be recovered. To recover the information, knowledge about the objects in the scene and projection geometry is required. Industrial vision systems demand greater robustness, reliability, and stability compared with an academic/educational vision system and typically cost much less than those used in governmental/military applications. Therefore, industrial machine vision implies low cost, acceptable accuracy, high robustness, high reliability, and high mechanical and temperature stability.

1.2 Evolution of Machine vision:

The evolution of machine vision over the past five decades is shown in Figure 1.1. The beginnings of machine vision were developed in the late 1940s and early 1950s with initial research into artificial intelligence. This is also when the military began applying image analysis. This concept did not become industrialized until the 1960s and 70s. At this point, Massachusetts Institute of Technology developed an image analysis system that could control a robotic arm for applied industrial uses. Several line-labelling algorithms were developed at that time. The topic of edge detection was also an active area of research; the early work in simultaneous recovery of 3D structures and camera motion also began around this time[2].

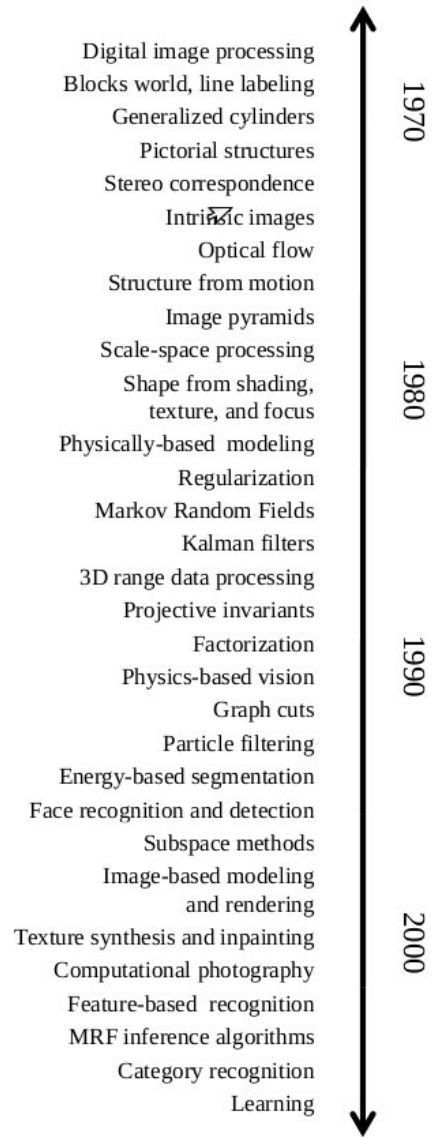


Figure 1.1 Evolution of Machine vision[2]

In the 1980s, a lot of attention was focused on developing sophisticated mathematical techniques for performing quantitative image and scene analysis. Machine vision took off and saw great expansion on the industrial level. At this point, research into better edge and contour detection was active some of which are shown in Figure 1.2 and Figure 1.3. During this period, grey scale machine vision algorithms, single board image processors, and cameras for industrial applications became commercially available. Machine vision became popular in a production line in many industries[2].

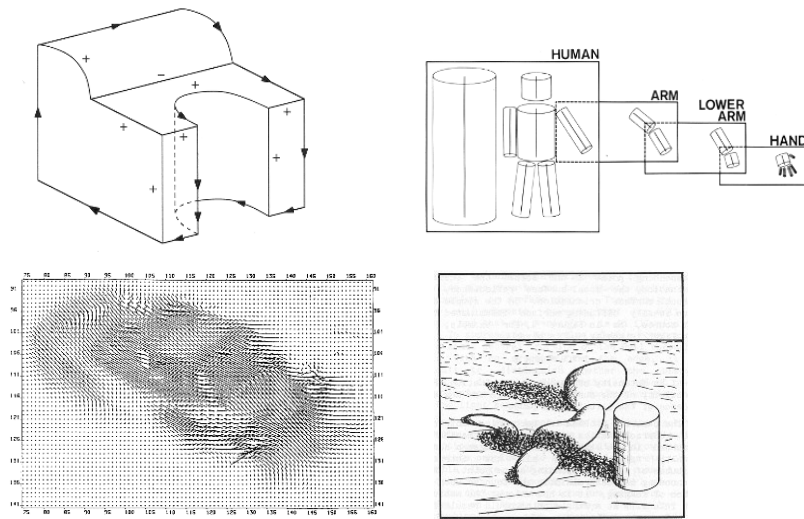


Figure 1.2 Examples of computer vision algorithms from 1970s (a) line labelling (b) articulated body model (c) optical flow (d) intrinsic images[2]

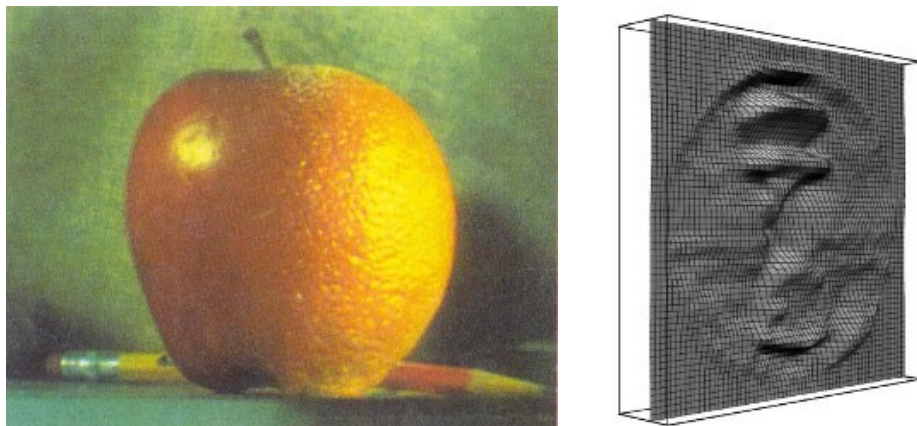


Figure 1.3 Examples of computer vision algorithms from the 1980s (a) pyramid blending (b) shape from shading[2]

The 1990s brought a boom of growth to the machine vision industry. The advancement of computer technology was the main driver behind this expansion. Multi-view stereo algorithms that produce complete 3D surfaces (as illustrated in Figure 1.4 and Figure 1.5) were also an active topic of research in this period. Processing chips made it possible to create smart cameras, which not only collect the image data, but they can also extract information from these images without using a computer or other external processing unit. Tracking algorithms also improved a lot, including contour tracking using active contours[2].

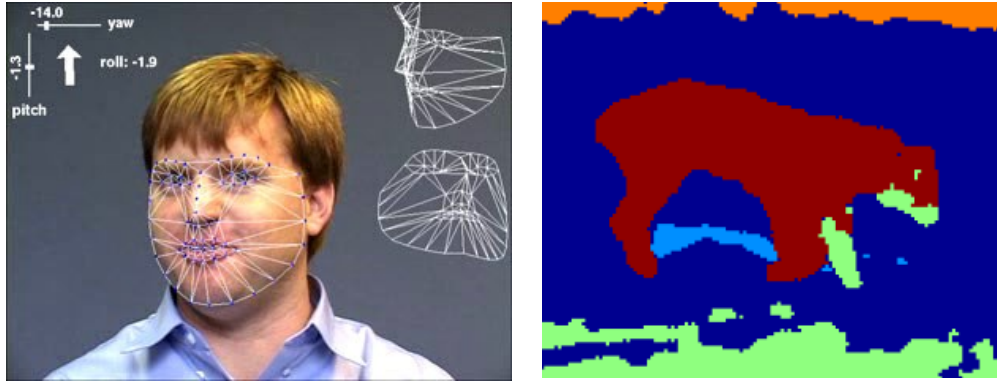


Figure 1.4 Examples of computer vision algorithms from the 1990s (a) face tracking (b) image segmentation[2]

In the 2000s and continuing in present day, the machine vision industry continues to see growth. The availability and affordability of digital camera systems greatly increased the accuracy and abilities of machine vision. Because of these advances in technology, machine vision has ceased being a futuristic idea and is now widely accepted and used within the manufacturing industry for applications including quality assurance and control.[2]

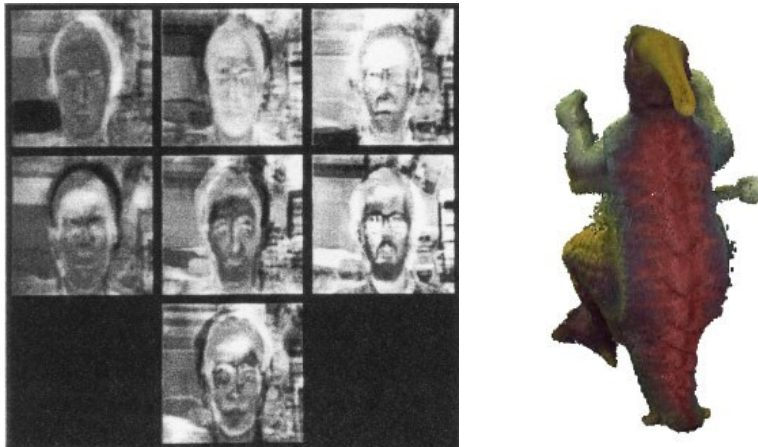


Figure 1.5 (a) face Recognition (b) multi-view reconstruction [2]

1.3 Techniques related to machine vision;

Techniques developed from different areas are used for recovering information from images. In this section, we briefly describe some fields that are closely related to machine vision.

1.3.1 Image processing

Image processing techniques are used to transform captured images into other images. The task of required information recovery is left to the user. It includes some other important topics such as image enhancement, image compression, and correcting blurred or out-of-focus images. On the other hand, machine vision algorithms are also extensively used to take images to produce other types of outputs such as representations for the object contours in an image. Thus with minimal human interaction, the information from the image can be recovered. Image processing algorithms are useful in early stages of a machine vision system. They are usually used to improve particular information and suppress noise.[3]

1.3.2 Computer graphics

Computer graphics generates images from basic geometric features such as circles, lines, and free-form surfaces. This technique plays an important role in the visualization and virtual reality. On the other hand, machine vision is just the contrary, which involves estimating the geometric primitives and other features from the image, as shown in Figure 1.6. Thus, computer graphics is the creation of images, and machine vision is the analysis of images. In the recent years, these two fields have been growing closer. Machine vision is using curve and surface representations and several other techniques from computer graphics, and computer graphics is using many techniques from machine vision to enter models into the computer for creating realistic images. Graphic visualization and virtual reality are bringing these two fields closer.[3]

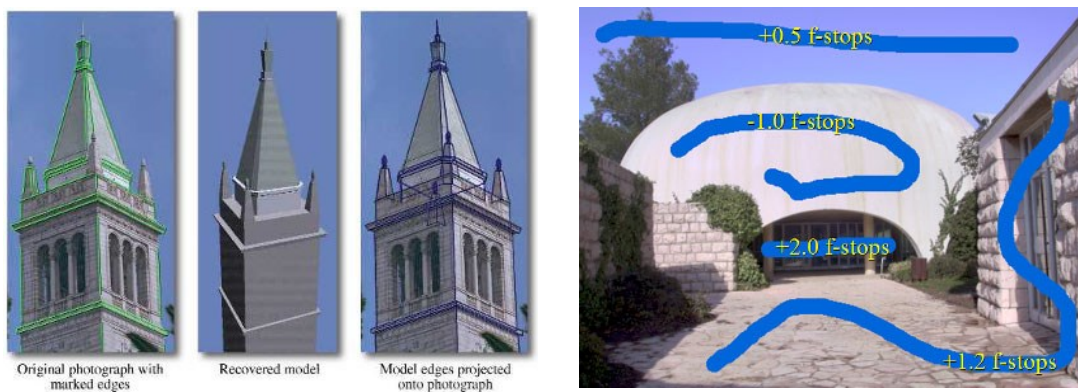


Figure 1.6 Recent examples of computer vision algorithms (a) Image-based modelling (b) Tone mapping[2]

1.3.3 Pattern recognition

As illustrated in Figure 1.7, pattern recognition classifies numerical and symbolic data. Techniques from pattern recognition play an important role in machine vision for recognizing objects. Many industrial applications rely heavily on pattern recognition.[3]



Figure 1.7 (a) Feature-based recognition (b) Region-based recognition [2]

1.3.4 Artificial intelligence

Artificial intelligence is a concept of designing systems that are intelligent and studying computational aspects of intelligence. After the captured images have been processed to obtain features, artificial intelligence is used to analyze scenes by computing a symbolic representation of the contents of the scene. Artificial intelligence briefly described in three stages: perception, cognition, and action. Perception translates signals from the world into symbols, cognition manipulates symbols, and action translates symbols into signals that effect changes in the world. Many techniques from artificial intelligence play important roles in all aspects of computer vision. Therefore, computer vision is often considered a subfield of artificial intelligence.[3]

1.4 Components of machine vision

The components of machine vision system include,

1.4.1 Camera:

The job of the image acquisition device in a machine vision system is to receive a pattern of illumination from an optical system, which is a true representation of its spatial and temporal

variations and convert this varying photon signal into a varying electrical signal. It requires combination of an image sensor with electronics. The device should meet the electrical, optical, mechanical and environmental requirements of the system in which it operates. This combination is called a camera.

The operation and performance of a camera is largely constrained by the image sensor in it. The detailed understanding of sensor characteristics can help in choosing the cameras suitable for particular tasks.

1.4.2 Camera Software

In general, there are two different selections for imaging software: camera-specific software development kits (SDKs) or third-party software. SDKs include application-programming interfaces with code libraries and they consist of simple image viewing and acquisition programs that do not require any coding and offer simple functionality. With third-party software, camera standards (GenICam, DCAM, GigE Vision) are important to ensure functionality. Third party software includes NI LabVIEW™, MATLAB® and OpenCV. Often, third-party software is able to run multiple cameras and support multiple interfaces, but it is ultimately up to the user to ensure functionality.[4]

1.4.3 Optics

The lens collects the light reflected from the part being observed, and forms an image on the camera sensor. The proper lens allow us to see the required area of the scene, in other words the field-of-view (FOV) and to place the camera at a suitable working distance from the object. The working distance is defined as the distance from the front of the camera to the part being inspected. From the FOV, the focal length of the lens can be estimated by considering the working distance and the camera specifications. The focal length is distance behind the lens where parallel light rays are brought to a focus. Common focal lengths for lenses in machine vision are 12 mm, 16 mm, 25 mm, 35 mm and 55 mm. When the calculations are done for specific applications, the estimated focal length will probably not exactly match any of these common values. We typically pick a small focal length and then adjust the working distance to get the desired FOV.[5]

1.4.4 Lighting

Lighting is one of the important factor for the successful machine vision. Machine vision systems create images by observing the reflected light from the object. A lighting technique involves a light source and its position in the set up with respect to the object and the camera. A particular lighting technique can improve an image such that it removes some features and enhances other features, by selectively choosing a part of the object, which hides surface details to allow measurement of its edges. Most common lighting varieties include:

1.4.4.1 Back lighting

Backlighting (Figure 1.8) improves the object's outline for specific applications that need only external or edge measurements. Back lighting helps to detect shapes and makes dimensional measurements more reliable.[6]

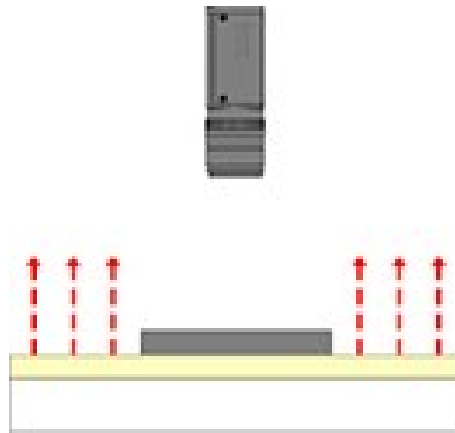


Figure 1.8 Back lighting[6]

1.4.4.2 Axial diffuse lighting

Axial diffuse lighting pairs light into the optical path from the side (coaxially). Schematic of axial diffuse lighting is depicted in Figure 1.9 where a semi-transparent mirror illuminated from the side, directs the light downwards on the object. The part reflects the light back to the camera through the semi-transparent mirror.[6]

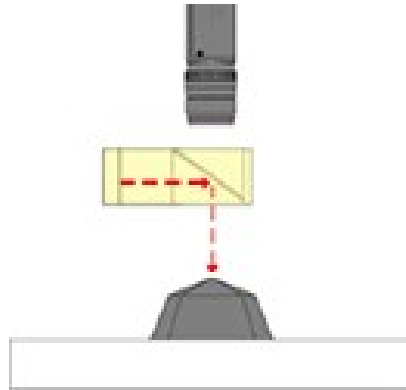


Figure 1.9 Axial Diffuse lighting[6]

1.4.4.3 Structured light

Structured light is the projection of a light pattern on the surface or grid, or complex shapes at known angle onto an object as illustrated in Figure 1.10. It has lot of applications involving surface inspections, acquiring geometrical dimensional information and calculating volume. This is contrast-independent lighting system.[6]

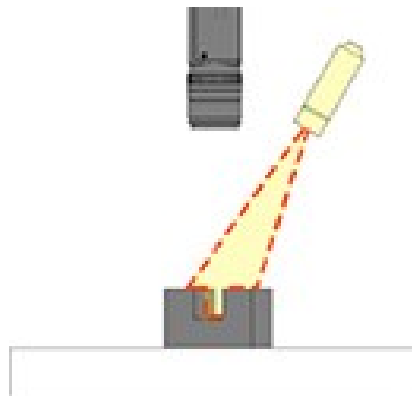


Figure 1.10 Structured light[6]

1.4.4.4 Dark-field illumination

Directional lighting more easily exposes surface defects, which includes dark-field and bright-field illumination. Dark-field illumination, illustrated in Figure 1.11 is generally preferred for low-contrast applications. In dark-field illumination, specular light is reflected away from the camera. The dispersed light from the object surface containing useful information such as surface texture and topography are reflected back into the camera.[6]

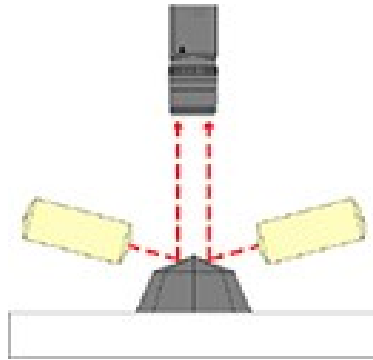


Figure 1.11 Dark field illumination[6]

1.4.4.5 **Bright-field illumination**

Bright-field illumination ideally used for high-contrast applications. Schematic of bright field illumination is shown in Figure 1.12. Highly directional light sources such as high-pressure sodium and halogen may produce sharp shadows, which results in inconsistent illumination throughout the entire field of view. Shiny or reflective surfaces requires more diffused light source to provide uniform illumination in the bright field.[6]

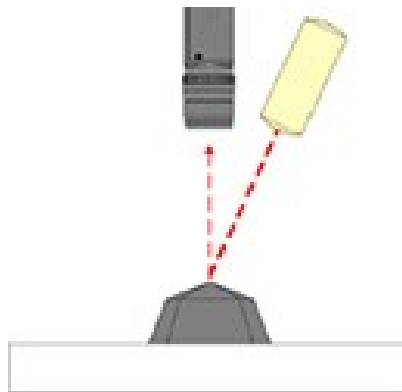


Figure 1.12 Bright-field illumination[6]

1.4.4.6 **Diffused dome lighting**

Diffused dome lighting, shown in Figure 1.13, it provides uniform illumination on all the features of interest, and can mask irregularities that are not of interest, which may be confusing to the scene.[6]

1.4.4.7 Strobe lighting

Strobe lighting, shown in Figure 1.14 is used in high-speed applications to capture moving objects for examination. Using a strobe light blurring of the scene can be avoided. In strobe mode, the lighting will be switched on only as and when required. The feedback unit receives a signal when a strobe is required.[6]

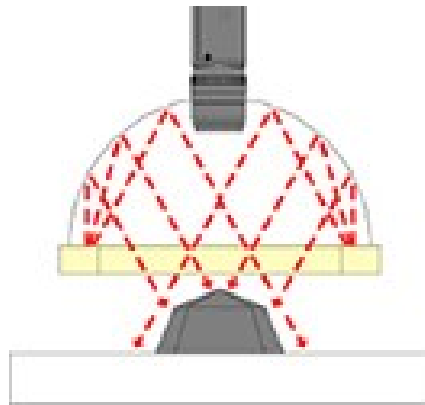


Figure 1.13 Diffused dome lighting[6]

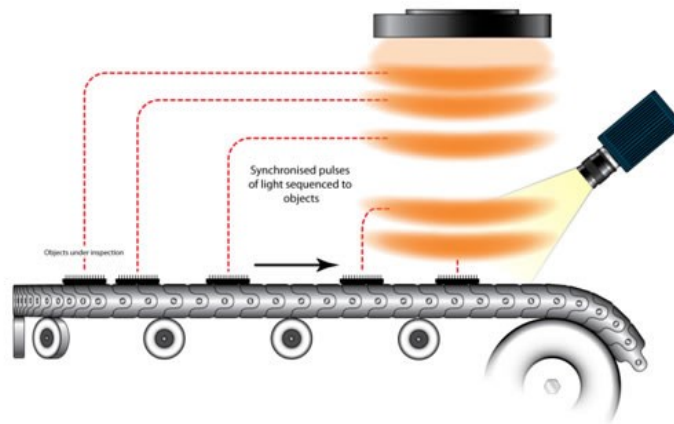


Figure 1.14 Strobe light used in high speed inspections[7]

1.5 Different types of machine vision:

Based on the type of image acquisition, machine vision systems are broadly categorised into 1D, 2D and 3D vision systems.

1.5.1 1D Vision system

Schematic of a 1D-vision system is shown in Figure 1.15. This vision system examines a digital signal one line at a time instead of viewing at a whole scene at once, such as assessing the variation between recently acquired group of lines and an earlier group. This system normally detect defects on materials manufactured in a continuous process, such as paper, metals, plastics, and other rolled sheets or goods.

1.5.2 2D Vision system:

This system captures a digital 2-dimensional image in various resolutions, as depicted in Figure 1.16 and Figure 1.17, which are generally used in the industrial applications. They are subdivided into area scan and line scan systems.

1.5.2.1 Area scan system:

Area scan system contains cameras with a large sequentially arranged array of pixels that capture an image of a given scene in a single exposure. They are general-purpose cameras, which offer easier positioning and setup. Area scan systems are best suited for the applications where the object is stationary.

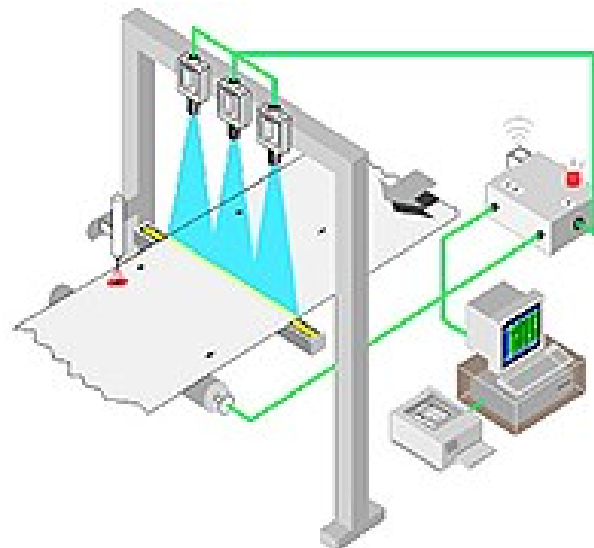


Figure 1.15 1D vision system[8]

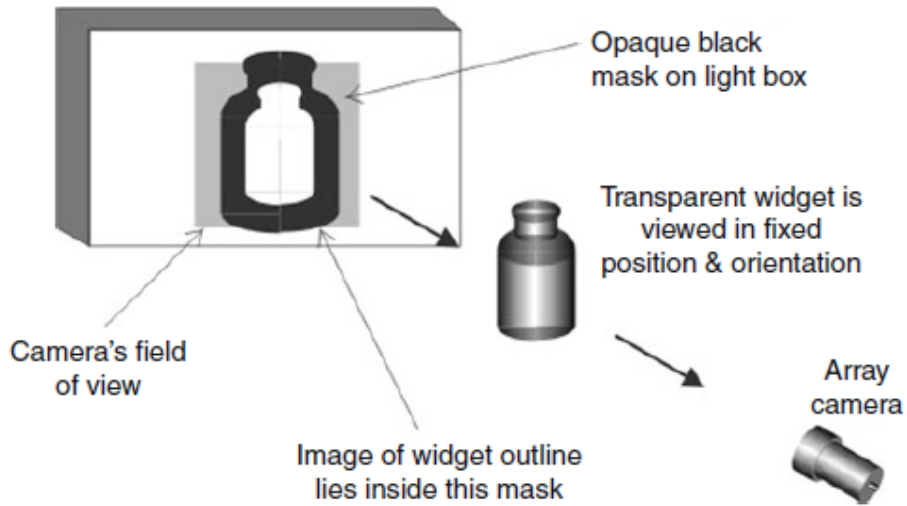


Figure 1.16 Area scan system[9]

Area scan cameras have the fixed resolution, which allows simplified installation. They are best suited for the applications where the cameras or objects' movements are not desired or practical. They also provide greater flexibility, as a single image can be divided into multiple regions of interest to look for specific features rather than processing the entire image.

1.5.2.2 Line scan system:

In the line scan systems, cameras contain a single row of pixels, which constantly scan the moving objects. In the process, discrete pixels are read into a horizontal register arranged in parallel and are converted into digital values. These digital values will be stored and processed by the computer. Line scan systems are most commonly used in high-speed processing applications.

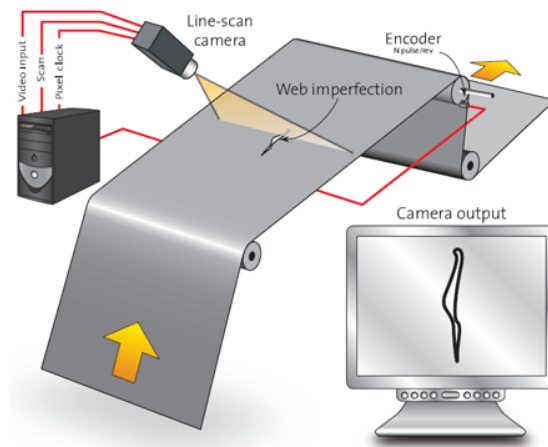


Figure 1.17 Line scan system[10]

To capture image of the entire surface of circular or cylindrical parts may require multiple area scan cameras positioned around the object. However, a single line scan camera captures the entire surface by rotating the part in front of it. These systems can fit more easily into confined spaces and the system requires minimum illumination. They can provide higher resolution than traditional area scan cameras. Synchronization of camera motion, object motion and image acquisition timing are critical for line scan cameras.

1.5.3 3D Systems:

3D machine vision systems typically contain multiple cameras or one or more laser displacement sensors.

1.5.3.1 *Passive Imaging:*

The most commonly used 3D systems utilizes stereo imaging in which two or more cameras are used to capture different images of a scene from different directions. This is illustrated in Figure 1.18. In this system, the area of the image captured and optical parameters of each different camera must be adjusted with a goal that triangulation techniques can be utilized to decide the relation between pixels in each image.[8]

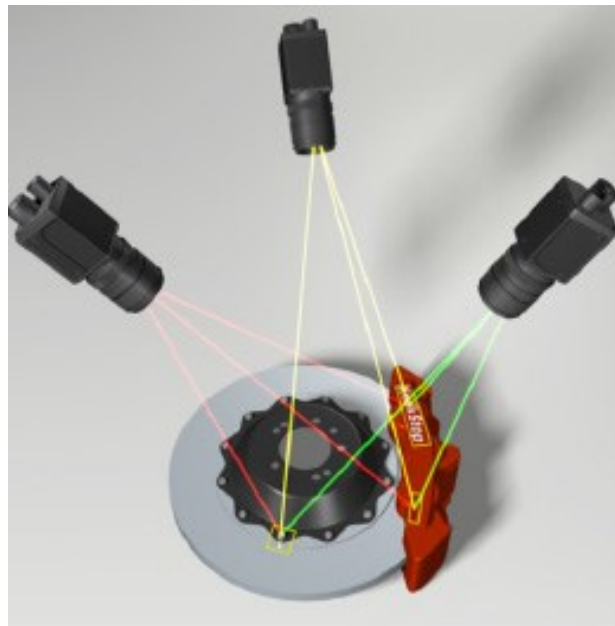


Figure 1.18 Passive 3D imaging[8]

1.5.3.2 Structured lighting:

Laser light is used in such systems as source of structured lighting. To generate a 3-dimensional surface of an object, a camera is used to capture the reflected coherent light from the object surface. Since the geometrical combination of the laser and the camera are known, the coordinates of the projected laser beam can be easily found out by triangulation, as shown in Figure 1.19.

As the object or laser/camera system moves across the field of view of the object to be measured, its geometrical coordinates in X, Y, and Z direction are measured. Measured coordinates are used to create a point cloud, which represents the outer surface geometry of the object. This point cloud can be extrapolated on to a plane to create a depth map consisting of 2D image that replaces the intensity values with depth data.[8]

Based on the type of camera and the interfaces used in the system, machine vision systems are divided into following types.

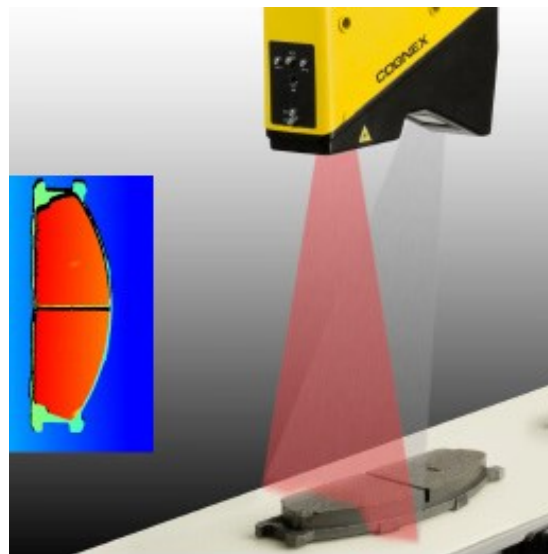


Figure 1.19. Single camera with structured lighting[8]

1.5.3.3 Analog and digital cameras:

In real-time, continuously changing electronic signals are communicated by analogue cameras. The amplitude and frequency of this transmitted signal is then read by an analogue output device as video information. The resulting image information directly depends on the quality of the analogue video signals and the way they are interpreted. Typically, analogue cameras are less

expensive and they are less complicated, which make them cost-effective and easy solutions for common video applications.

On the other hand, digital cameras transmit binary data in the form of electronic signals. Even though the voltage equivalent to the light intensity for a given pixel is continuous, the analogue to digital conversion method discretizes this and assigns a grayscale value between zero (black) and 2^N-1 , where N is the number of bits of the encryption. An output device then converts the binary information into image data. There will not be any change in the video signals in a path between camera and the output device. This results in less noise and no error in transmission of signal. In addition, digital cameras offer higher resolution and higher frame rates. The Figure 1.20 describes the major differences between digital and analogue cameras.

Since the output signal is discrete for the digital cameras, there will be little loss in the information during the transmission process. Based on the amount of data to be transferred, distance at which image-processing unit is placed and the number of devices to be connected, various camera interfaces are used. They are as follows,

- Capture boards or frame grabbers:
- Fire wire
- Camera Link
- GigE (GigE Vision Standard)

USB (Universal Serial Bus) - These boards contain an analogue to digital converter to digitize the analogue signal for image processing. Basic acquisition software is included with these boards to save, open and view the images. Comparison of different digital camera interfaces are shown in Figure 1.21.

1.5.3.4 Standalone Vision System

Standalone vision systems are practical and can be effectively configured. These systems come finished with the camera sensor, processor, and communications. Some additionally coordinate lighting and self-adjusting optics. In most cases, these systems are compact and sufficiently moderate to be installed all through the manufacturing plant. By utilizing standalone vision

systems at key process, defects can be found earlier in the production and equipment issues can be recognized more rapidly.

Analog Cameras	Digital Cameras
Vertical resolution is limited by the bandwidth of the analog signal	Vertical resolution is not limited; offer high resolution in both horizontal and vertical directions
Standard-sized sensors	With no bandwidth limit, offer large numbers of pixels and sensors, resulting in high resolution
Computers and capture boards can be used for digitizing, but are not necessary for display	Computer and capture board (in some cases) required to display signal
Analog printing and recording easily incorporated into system	Signal can be compressed so user can transmit in low bandwidth
Signal is susceptible to noise and interference which causes loss in quality	Output signal is digital; little signal loss occurs during signal processing
Limited frame rates	High frame rates and fast shutters

Figure 1.20 Comparison of Analog and digital camera[4]

Digital Signal Options	FireWire 1394.b	Camera Link®	USB 2.0	USB 3.0	GigE
					
Data Transfer Rate:	800 Mb/s	3.6 Gb/s (full configuration)	480 Mb/s	5Gb/s	1000 Mb/s
Max Cable Length:	100m (with GOF cable)	10m	5m	3m (recommended)	100m
# Devices:	up to 63	1	up to 127	up to 127	Unlimited
Connector:	9pin-9pin	26pin	USB	USB	RJ45/Cat5e or 6
Capture Board:	Optional	Required	Optional	Optional	Not Required
Power:	Optional	Required	Optional	Optional	Required (Optional with PoE)

Figure 1.21 Comparison of different camera interfaces[4]

1.6 Resolution and accuracy requirements

Accuracy, repeatability, and resolution are three main key points by which any measurement tool is assessed.

Accuracy is the degree of conformity between a measured quantity and a known standard or specification that specifies the true value of the quantity. Accuracy is a qualitative idea i.e., one in which a process is based on physical properties. Often accuracy is confused with precision, which defines as the degree of closeness in the independent test results, which are obtained by applying same procedures under same experimental conditions. It is an indication of the uniformity or reproducibility of a result.[11]

Repeatability of a measurement is the degree of variation in the repeated measurements of the same quantity under same operating conditions from their mean value.

Resolution refers as the ability to see the smallest optical features (pixels) as two different entities in an optical system. It depends on many factors,

- Number of pixels on the image sensor
- Magnification
- Quality of the optics used to capture the image

Accuracy, repeatability and resolution are inter related in one or the other way.

Accuracy of measurement process cannot be calculated efficiently without checking its repeatability. If the process cannot generate repeatable measurements that system can never be accurate. In addition, in some cases we might achieve the repeatability of the process without being accurate. So in order to overcome this, it is necessary to perform the object measurement to ensure the proper quality control and repeatable measurements must be calibrated to make them accurate resulting in obtaining true measurements.

Once the scene is captured by the camera, the video signals are digitized and the resulting image data will be stored in the computer memory and can be accessed by the image processor. Resolution of the image is defined as the number of pixels in the image and the number of bits of data used by the computer memory to store the brightness information describes the depth of the image. Each pixel has a numerical value from 0 to 255, where 0 represents black, 255 represents white and in between values represent the different shades of grey. These values are assigned during digitization of signals by considering the average brightness of area at which the pixels are

occupied in the original analogue image. Imaging with lower resolution sometimes results in temporal error caused due to time delay between transmission of pixel and digitizing its value.

By increasing the resolution of the image in other words by adapting increased number of pixels on the camera sensor, measurements can be made more accurately. Increased resolution results in reduced temporal errors and all required information from the scene can be effectively captured.

1.7 Different applications of Machine vision

Peng Chena et.al proposed a machine vision based data glove with certain encoded features on its surface. The sensors attached on the glove was replaced by the machine vision device, which captures the codes on the glove to obtain the hand motion data. Conformal geometric algebra was introduced to handle the complex geometrical transformations in the strip glove motion there by tracking the motion of the strip glove[12]. This is illustrated in Figure 1.22.

Franci Lahajnar et.al presented a machine vision based automated visual inspection system for the plates of the electric cookers. The dimensions of the different sized electric plates are defined by using two cameras with tele centric lenses by applying subpixel edge detection techniques[13].
Bulanon, D.M. et.al developed a real time machine vision system to guide a harvesting robotic manipulator for red Fuji apples. The system has the capability to locate the ripened fruit in different lighting conditions[14].

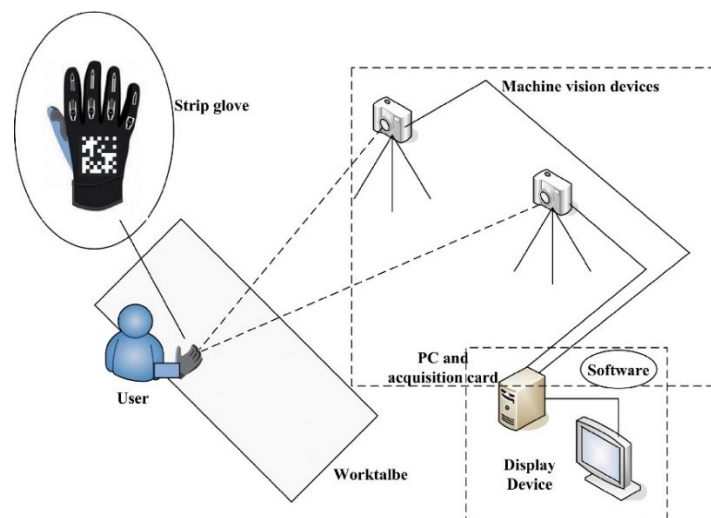


Figure 1.22 Framework of the strip glove system[12]

C. Bradley and Y. S. Wong proposed a machine vision based model, as shown in Figure 1.23 to estimate the cutting tool condition i.e., the degree of tool wear by extracting three parameters from video camera images of the machined surface. They have analyzed intensity histogram, image frequency domain content and spatial domain surface texture to estimate the degree of wear on the tool.[15]

To prevent the flaws in the products due to usage of worn-out tools, measuring the variations in topography on a grinding wheel is an important task in precision manufacturing. J. C. Su. Y. S. Trang proposed a method of measuring the wear on the grinding wheel using machine vision. This method makes the 3 D topography of the grinding wheel into the 2D contour of the grinding wheel, which simplifies the wear measuring procedures compared to traditional methods[16].

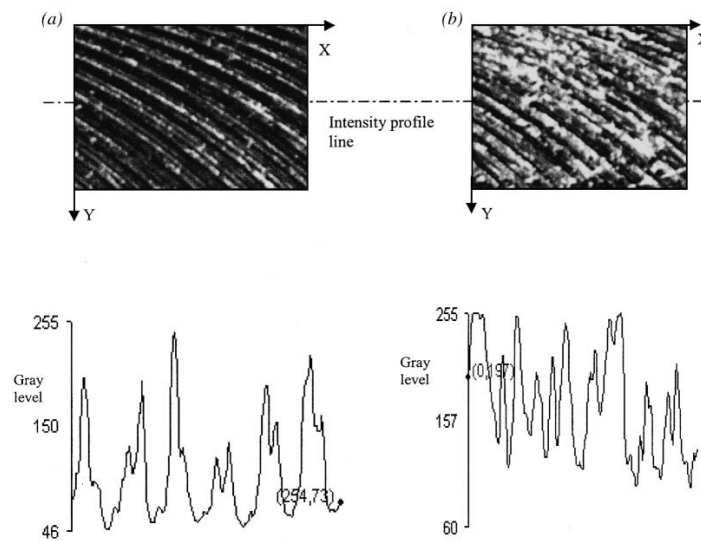


Figure 1.23 Digital images and corresponding intensity profiles from (a) sample 1 with a new tool, and (b) sample 2 with a worn tool[15]

Large raw parts consumes long time for alignment with the tool before machining process starts. A. Mendikute et.al proposed an automated alignment solution based on the 3D vision technology. The targets at the representative points of the surfaces to be machined are located first, the extrinsic parameters of the camera at each photograph (position and orientation) are calculated, and then proceeded for the alignment of the part in machine axes by using stereo photogrammetry[17]. The system proposed by Mendikute et al. is shown in Figure 1.24.

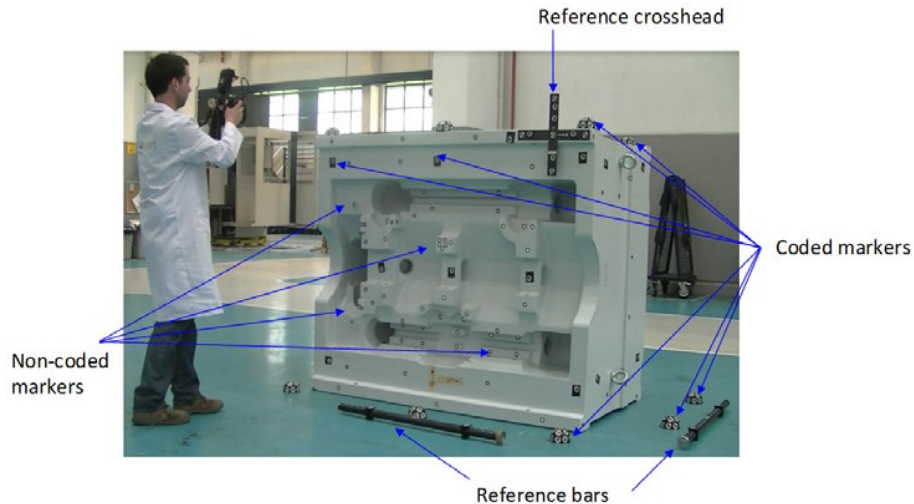


Figure 1.24 Photogrammetric measurement of type B pilot case: optical markers, reference crosshead and reference bars[17]

Y D Chethan et.al presented a method to measure the surface roughness of the turned Nimonic75 material using coated carbide tool at different spindle speed and feed rates. Turned surface images were acquired using machine vision camera. The histogram distributions of an illuminated region of interest (ROI) from turned surface images were analyzed to assess changes in the frequency of the histogram, which quantify the surface roughness.[18]

F Luk et.al developed a method for surface roughness measurement using machine vision system in the production environment. They employed a microcomputer-based vision system to analyze the pattern of scattered light from the surface to derive a roughness parameter[19].

The automation of the manufacturing process plays an important role in improving productivity. For this, monitoring systems are extremely necessary in manufacturing. Y D Chethan et.al proposed a new method by using machine vision to estimate the tool status in cutting inserts to determine the time of replacement. This is depicted in Figure 1.25. By analyzing the binary images, the features representing the state of cutting tool in terms of wear area, perimeter of the tool and compactness are studied. Based on the extracted features, the time of replacement of the tool will be decided[20].

This project is mainly concerned with the laser-based manufacturing. In the following section, introduction to lasers and laser based manufacturing will be overviewed with reference to literature.

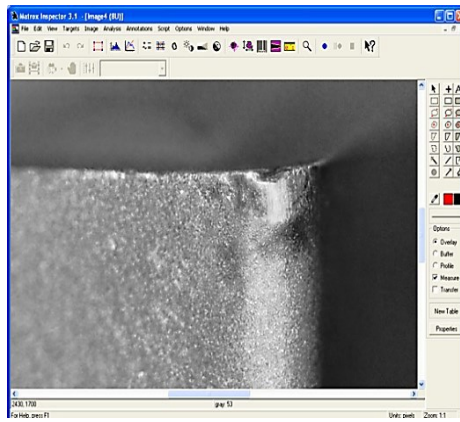


Figure 1.25 a) Fresh tool Image

b) Tool with region of interest

c) Tool status as seen under machine vision[20]

1.8 Laser based Manufacturing

LASER is an acronym for Light Amplification by Stimulated Emission of Radiation. The laser differs from ordinary source of light in the emission of radiation. In lasers, the photons are emitted by stimulated emission, which are characterized with the properties of same wavelength, phase, direction and polarization. The ability to amplify light in the presence of a sufficient number of excited atoms results in optical gain that is the basis for the laser operation[21].

1.8.1 Properties of the laser

Monochromaticity - The energy of a photon determines its wavelength through the relationship $E=hc/\lambda$ where c is the speed of light, h is Planck's constant and λ is the wavelength. In an ideal laser, all photons emitted with the same energy, thus the same wavelength.

Coherence - Besides the same wavelength, the photons that form a laser beam are all in phase. Coherence is that all the individual waves of light, which are moving together in time and space. Correlation between the waves at a point, at different instants or along the path of a beam at a single instant, is defined as temporal coherence. Correlation between different points (but not along the path) is called spatial coherence.

Directionality – The photons traveling parallel to the cavity walls will be reflected from both mirrors. Therefore, the multiple reflection produces a collimated light. Any photon that is out of optical axis will be lost and thus all the emitted photos are unidirectional.

Brightness or Radiance- It is defined as the amount of light leaving the source per unit surface area per unit solid angle. Because of its high radiance, a laser beam can be projected over great distances.

Ability to focus - Focusing of laser beams enables high intensity at the focusing spot. Laser power and the spot size are the crucial parameters for laser material processing. With very low divergence, minimum possible spot diameter that can be achieved from a Laser is equal to about its wavelength.

High power - The achieved photon density at the output depends on the density of excited atoms in active medium and volume of active medium. Higher photon density results in higher laser power. Very high powers of lasers are can be achieved by different methods of pulse generation/pulse compression techniques.

1.8.2 Types of lasers used for manufacturing

Lasers can be divided into two main categories: continuous wave (CW) and pulsed. The exact wavelength of the laser beam determined by the characteristics of the laser medium. Lasing medium can be either gas, liquid or solid.

Continuous-wave lasers produce an uninterrupted, continuous beam of light with a very stable output power. Long pulse lasers also come in this category. In continuous laser, machining of material takes place by heating and melting of the material. As heating and melting is the key phenomenon behind continuous laser machining, this type of machining always results in recast layer and high heat affected zone. Due to low quality of machining, continuous lasers are not considered for most of the industrial and research purposes.

In pulsed lasers, the laser beam is emitted periodically. We define pulsed lasers as devices that produce pulses in the range of 0.5 to 500 ns. The laser pulses with high energies and shorter pulse width can be produced by using any of these mechanisms as Q switching, mode locking, Cavity damping and gain switching. The schematic of the operating principle of Q switch in solid-state laser is shown in the Figure 1.26.

Pulse laser based machining can be divided into two metal removal methods, pyro lithic (thermal) and photo lithic processes[22]. Pyro lithic process is associated with Nano and micro second pulses. In pyro lithic process material is removed by rapid heating, melting and partial evaporation of the heated volume of the material. On the other hand, photo lithic process is the phenomenon of material removal associated with ultrafast laser pulses as Pico and femtosecond lasers.

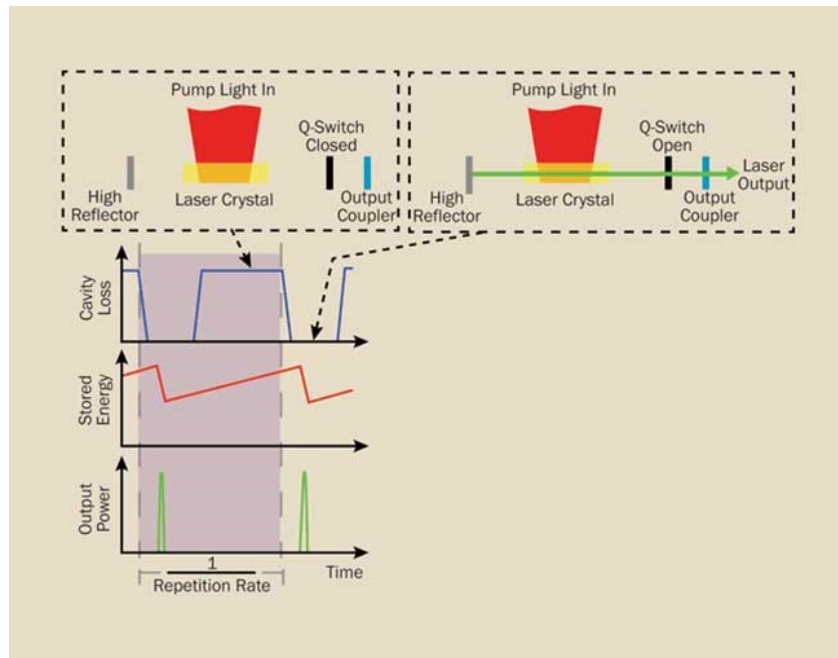


Figure 1.26 Schematic showing the operating principle of a Q-switch in a solid-state laser[21].

In photo lithic processes, the photon energy is sufficient to break chemical bonds in material removal. Ultrafast lasers are generally defined as lasers that produce pulses in the range of 5 fs to 100 ps. In industrial applications, amplified ultrafast pulses are increasingly used in materials processing applications that require ablation or materials modification without any residual thermal effect and/or on a submicron spatial scale. Many other laser based manufacturing processes are mentioned in the literature that includes. The current project is concentrated to laser micromachining. In the following section, the applications of lasers in Micromachining are explained with reference to the literatures.

1.8.3 Laser micromachining

Surface texturing - Micromachining of the complex structure has been a challenging research topic for researchers in micro fabrication like MEMs, biomedical devices, aerospace etc. There are

various potential applications of laser-textured surfaces based on modified material properties. The textured surfaces displaying structural color can perform as a permanent paint that might be used for decorative purposes. Vorobyev et al. presented a technique, illustrated in Figure 1.27 to provide controllable modification of optical properties of metals from the UV to THz spectral range via surface structuring on the nano-, micro-, and submillimeter-scales.[23]

Furthermore, the method proposed by Yao et al. facilitates decorating different regions of the surface with different types of ripples whose orientation can be varied based on the polarization of laser [24]. The high level of light absorption in the textured surfaces can be effective in solar cells applications[25] and in stealth technology such as sonar and radar systems[26]. Hwang et al. proposed a method for dramatic enhancement of solar-driven thermoelectric devices that lead to a step forward in solar energy harnessing[27]. In addition, Nayak et al. created self-assembled micro/nano structures to trap the efficient light on the silicon surface; the method could reduce the light reflection for the entire solar spectrum[26]

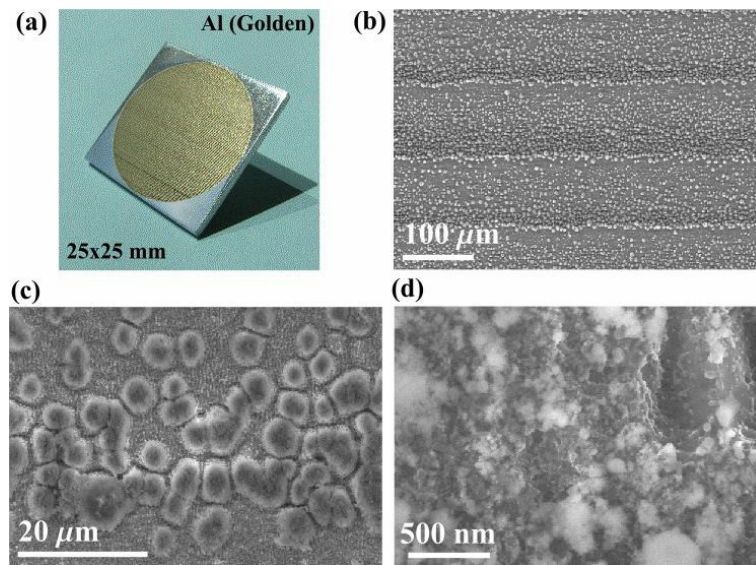


Figure 1.27 Coloured aluminium produced by femtosecond laser pulses. (a) Photograph of the gold aluminium; the gold appearance is independent of viewing angle. (b)–(d) SEM images showing micro- and nano-scale structural features of the gold aluminium.[23]

Fabrication of Super hydrophobic surfaces by laser texturing have significant impact in various applications that comprise anti-icing, anti-corrosion, self-cleaning, and drag reduction. Anti-icing investigation which is presented in Kietzig et al. research, posits that grooves oriented (by laser micro machining) in the sliding direction significantly decrease friction in the low velocity range

compared to scratches and grooves randomly distributed over a surface[28]. Zorba et al. presented the investigation on water repellency and self-cleaning properties[28]. Vorobyev et al. described a method for modifying the surface wetting properties[29].

Biomedical applications of laser-textured surfaces comprise biocompatibility [30][31] the evaluation in Liang et al shows micro-patterns not only accelerated the cell adhesion and proliferation, but also oriented their growth[28] and Yang et al. method provide fast approach to generate the microstructure with biocompatible deposition which can enhance the biocompatibility of metallic device [32]. Besides, few researchers [33][34] have studied cell adhesion reduction and improvement depending on the types of cells.

Other applications of textured surfaces include thermal radiation[32], the proposed method by Yang et al. improved the maximum thermal emissivity at different temperatures two times more, besides they found that the thermal emissivity enhancement factor is a function of the wavelength [32]. Enhanced photodiode performance can be another application, which is presented in[32], Carey et al. fabricated the photodiodes with a broad spectral response ranging from the visible to the near infrared[35]. Other applications include, Magnetic data recording media, X-ray generation, and reduced wear in mechanical parts [36]. Durbin, S.M et al. employed high-energy laser pulses at ultraviolet wavelengths to selectively remove industrial oil-based organic contaminants from micro cavities in steel based components in the production line environment[37].

According to the aforementioned, lasers have been widely applicable in metallic materials machining. Lately, lasers have been employed for the nonmetallic materials such as ceramics, composites, and semiconductors (e.g., silicon, silicon carbide, etc.) machining [38]. The capability of pulsed lasers, to accurately machine microstructure of materials such as ceramics and semiconductors (e.g., silicon) has caused a considerable interest in understanding the parameters controlling, the limitations and the capabilities of this process [38]. Amount of studies have been done to investigate the laser-based micromachining [39][40].

Surface patterning - H Y Zheng and T Lee proposed a material removal method in glass by continuous peeling off the glass strips with CO₂ laser beam. The proposed mechanism, shown in

Figure 1.28, involves the material expansion and contraction produced by a laser induced localized heating–cooling cycle[41].

A.Mathis et.al proposed a method to machine both curved surface profiles and curved trenches in micron scales on diamond and silicon samples[42]. Nadeem Hasan Rizvi used the laser ablation in conjunction with the mask projection technique to produce complex microstructures such as micro channels, ramps and contoured surfaces[43]. S.Ameer-Begb et.al used femtosecond laser pulses at 790 and 395 nm with the combination of galvoscaners mirror system for the ablation of high quality microchannel in Pyrex, fused silica and silicon for micro chemical applications[44]. Yuncan Ma et.al fabricated micro channels inside the silicon along the direction of the laser beam using femtosecond laser.

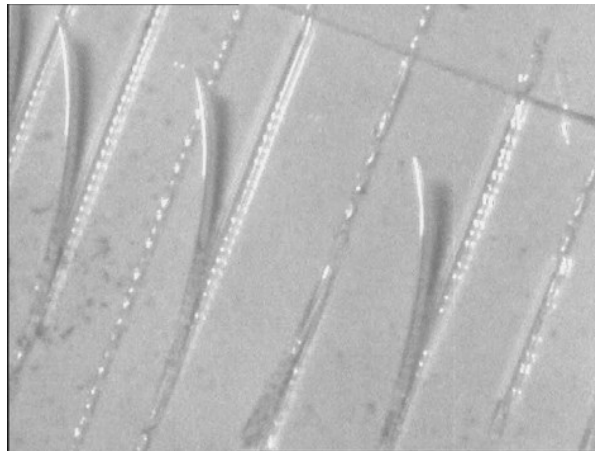


Figure 1.28 CO₂ laser-induced peeling of glass strips from a borosilicate slide[41].

StefanRusu et.al compared the effect of laser engraving on the titanium alloy for the microstructural and functional differences between surfaces using femtosecond and nano second lasers. They found out that Femtosecond laser engraving forms amorphous structures, composed of spherical particles. They conducted X-ray diffractometry to detect internal stresses modification occurred for nano and femtosecond laser markings[45].

JanezDiaci et.al developed a method for laser engraving on the tilted, curved and freeform work piece surface. This technique is shown in Figure 1.29. They implemented a camera and laser system in such a way that the system measures the 3D surface of the workpiece before processing[46]. Ming-Fei Chen et.al used CO₂ laser marking system to code on the eggshell

indicating the freshness of the eggs and the expiry date (Figure 1.30). They also analysed the depth of marking and the effect of heat-affected zone on the egg theca[47].

This project aims to develop a machine vision system for laser micromachining. In the following section, different laser based manufacturing processes which uses machine vision will be discussed with reference to literatures.

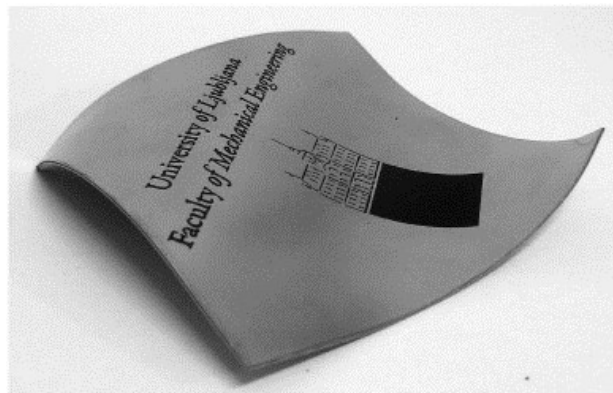


Figure 1.29 Freeform stainless steel sheet work-piece with a laser mark[46]

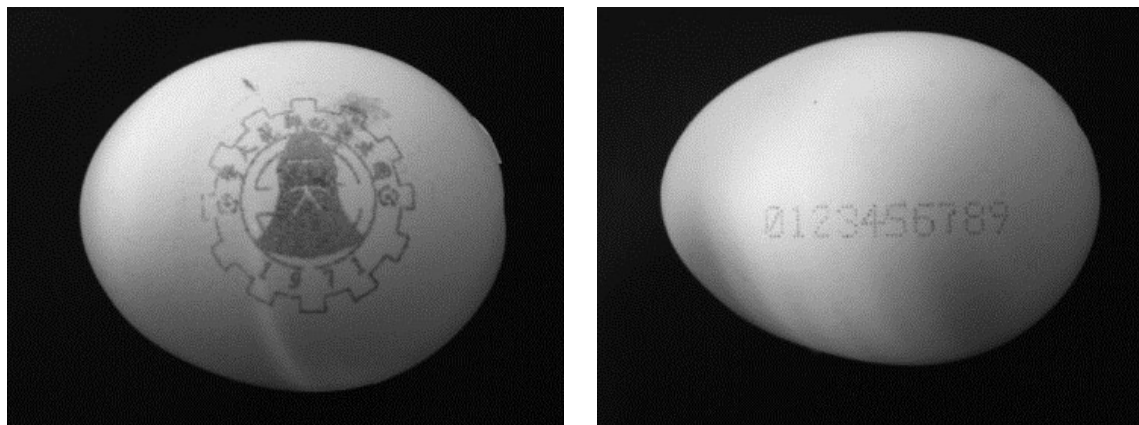


Figure 1.30 The school badge marked and Marked numerals on the eggshell [47]

1.9 Machine vision in laser based manufacturing

In recent years, Additive Manufacturing, commonly known as 3D printing, has experienced immense growth as an industry. Laser Powder Bed Fusion (LPBF) machines operate by spreading a thin layer of metal powder over a build plate using a recoater blade. After powder spreading, a

laser beam is used to selectively melt the powder in locations corresponding to a 2D slice of a 3D part. Luke Scime et.al developed an approach for in-situ monitoring and analysis of powder bed images in (LPBF) additive manufacturing. An algorithm was developed that is capable of autonomously detecting and classifying consequential anomalies related to the powder spreading stage of the process in an LPBF machine[48].

Despite increased technological advancement in the metal additive manufacturing, several possible source of defects are to be addressed to achieve the stability of the process especially in the presence challenging materials. M. Grasso et.al presented an online method to monitor the defects in Selective laser melting (SLM) an additive manufacturing (AM) process. The method involves the acquisition of the infrared images with data mining approach for feature extraction and monitoring the powder bed fusion process for difficult to process materials like zinc and its alloys. The method detects the unstable behaviours by analysing the salient properties of the process plume to detect unstable melting conditions. The schematic of the building chamber of SLM system is shown in the Figure 1.31.[49]

Yaoyu Ding developed a laser-based machine vision based measurement system for laser forming. The system measures the 3D profile of the deformed surface after laser forming. It works on the principle of laser triangulation. Based on the 3D profile data the vertical displacement curve and transverse shrinkage can be calculated[50](Figure 1.32).

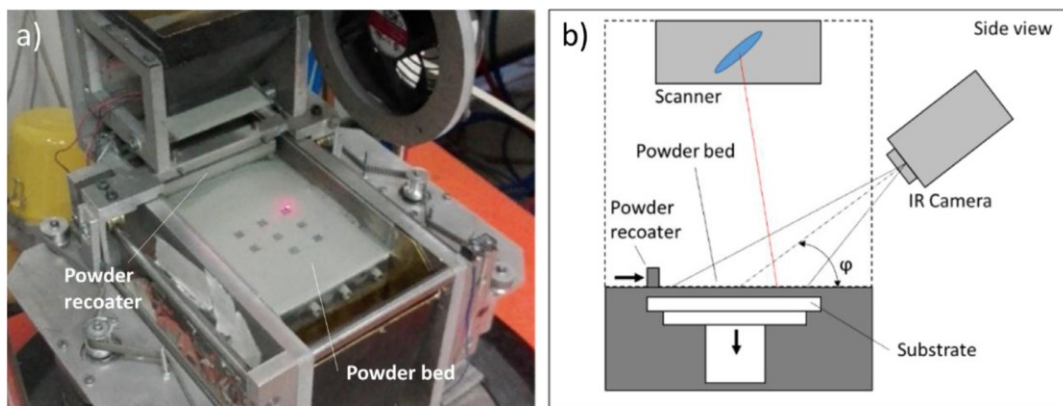


Figure 1.31 A view of the building chamber of the SLM system prototype used for the experimental activity; (b) side view of the IR camera setup[49]

Hofmann et al. and Hugger et al. first applied the three-dimensional tracking with stereo cameras to analyze spatters in laser welding with beam oscillation. They compared spatter formation during

welding of different steel and aluminum alloys. They showed significant differences in the spatter sizes and velocities for different grades of steel[51].

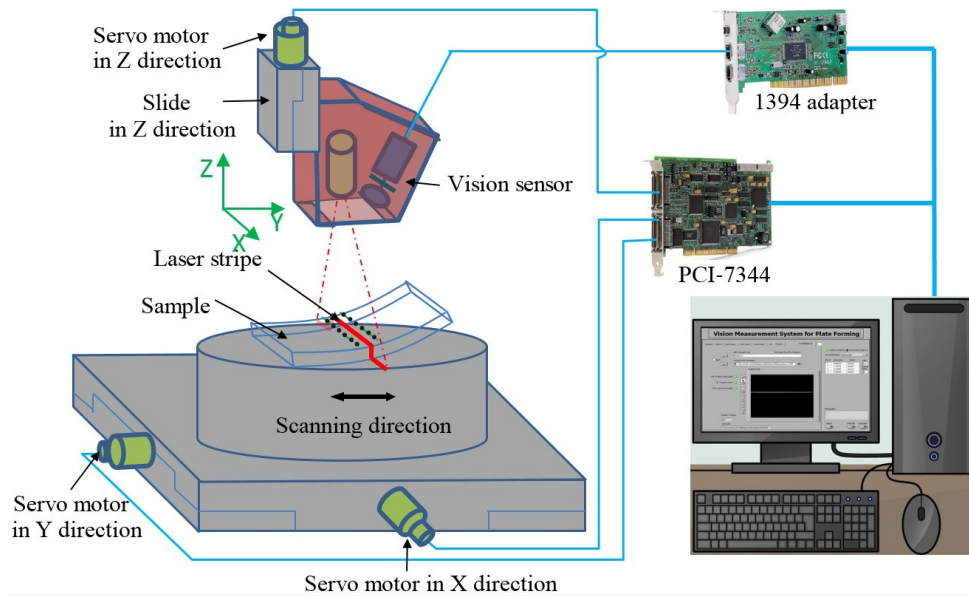


Figure 1.32 Schematic of the measurement system setup[50]

Mueller et al. used an industrial camera to evaluate spatter sizes during remote laser welding of fillet welds with laser beam oscillation. They showed that beam oscillation had a positive effect on welding with higher velocities as it reduced the number of spatters with a diameter larger than 300 microns[52]. M. Schweier et.al proposed an automated machine vision based approach to analyse the spatter formation in the Laser welding with beam oscillation. The spatters emitted during the welding were tracked by analyzing the sequence of images by means of Kalman-filter-based multi hypothesis tracking. By image processing, discrete time information on the properties of the spatter such as orientation, velocity and size were found out.[51]

Chao-Ching Ho.et.al developed a low cost online inspection system to monitor and estimate the depth of laser-drilled hole using machine vision. Through image acquisition and analysis of the laser machining process, the laser-induced plasma region was transformed into a pixel value. By analysing the images, they obtained a correlation between the cumulative pixels and the depth of the hole. The developed experimental set up with machine vision is as shown in the Figure 1.33[53].

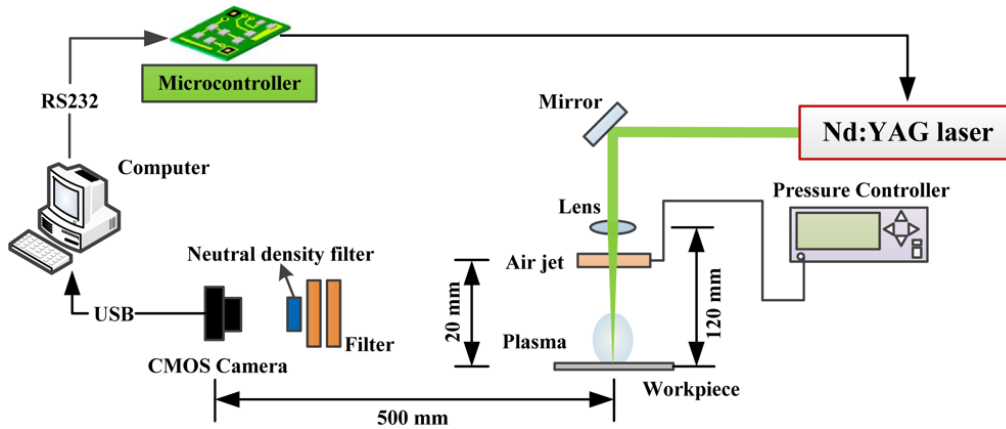


Figure 1.33 Experimental setup for laser machining and depth measurements[53]

Morgan Nilsen et al. proposed a dual vision and spectroscopic approach to trace narrow gap butt joints during laser welding. The system consists of a camera with suitable illumination and a miniature spectrometer. They developed an image-processing algorithm for the captured images to estimate the laser spot position relative to the joint position. The laser-induced plasma plume has been acquired by the spectrometer, and based on the measurements of the intensities of selected lines of the spectrum, the electron temperature signal has been calculated and correlated to variations of process conditions.[54]

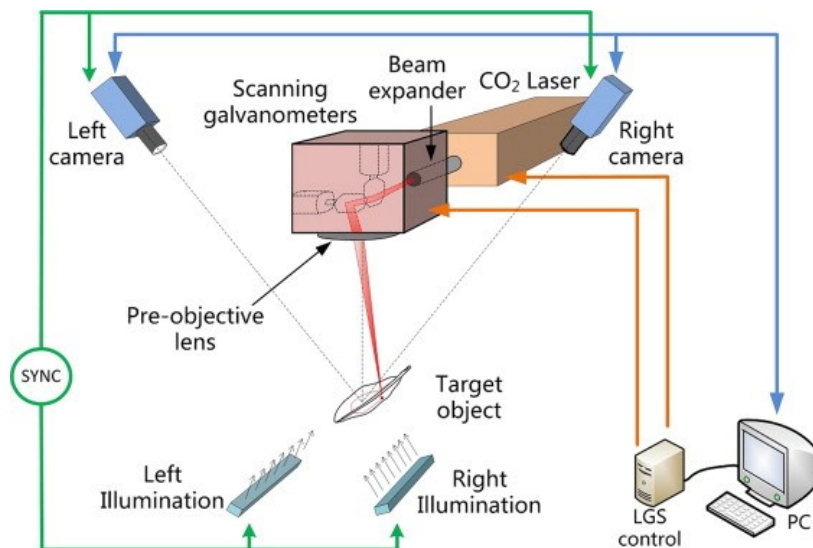


Figure 1.34 Stereo vision laser galvanometric scanning system[55]

Li Qi et al. developed a stereo vision laser galvanometric scanning system to machine the 3D structures using the laser. They obtained the 3D geometry of the object by the stereo cameras and

the obtained geometric coordinates are used to guide the scanning galvanometers for 3D-shape adjusted laser processing. They also developed a calibration method for the repeatability of the process. The experimental set up with stereo vision and scanning system is shown in the Figure 1.34[55]

1.10 Problem Identification and motivation

With the comprehensive study of the machine vision and laser micromachining and their applications, it is observed that there are minimal efforts towards addressing the accuracy and repeatability of the laser micromachining. Especially in the manufacturing and repair of microstructures, the accuracy is at most important. The effective utilization of vision system diminishes the different types of errors that can occur during micromachining process. The currently available machine vision systems to monitor the miniature structure manufacturing are very expensive and they are equipment specific. This gives a motivation to develop a cost effective machine vision system, which can be used as a standalone device for different applications. Therefore, an attempt was made to develop a machine vision assisted laser micromachining workstation, in the Laser Metrology and Micromachining Laboratory (LMML) of Concordia University, where significant amount of research is being performed in the field of peening using a high repetition rate and low energy laser.

1.11 Objectives and scope

Primary goal of this thesis is to develop a machine vision assisted laser micromachining workstation. To accomplish the objective, the scope of this research work would include

- To develop an experimental setup for machine vision and laser micromachining.

Error analysis

- To develop algorithms for the coordinate extraction of the required geometry to be machined.
- Processing of the images captured before and after the transformation of the specimen to extract the transformed coordinates.

- Analyzing the errors that occur during laser micromachining of the geometrically transformed specimen.

Coordinate extraction of curved shapes

- Comparison of the mathematical function based and image processing based algorithms to find the machining coordinates.
- Analysing the effect of different process parameters on the quality of laser micro machined surface.
- Development of simulation model for laser micromachining in COMSOL software package.

1.12 Organisation of the thesis

This thesis consists of six chapters. In the first chapter, literature review on the basics, evolution, and machine vision applications in laser micromachining are overviewed. Based on the literature review, research problem was identified and the objectives defined.

Second chapter deals with the materials used for conducting the experiments with their technical details, design of experiments, development of algorithms and the total number of experiments conducted are described.

In the third chapter, preliminary results for the errors in the laser micromachining of transformed sample from its initial position are discussed. A rectangular sample was machined on the silicon wafer specimen for the analysis. Translational and angular errors are analyzed for varied movements of the sample in vertical and horizontal directions and in rotation. Causes for the occurrence of errors and the possible measures to correct them are addressed.

Fourth chapter gives the over view of the extraction of coordinates of curved shapes. Two different approaches for coordinate extraction such as Image based approach and Function based approach are discussed. To estimate the capability of both approaches, curved shapes with different slopes are machined with different percentage overlaps. The results are analyzed to decide the best approach for efficient coordinate extraction.

Fifth chapter involves the development of simulation model in COMSOL software package for the texturing of complex geometry. Experimental works are done by laser texturing of a rectangular sample with different process parameters and the results are compared with the simulation results. In addition, in the Sixth chapter, the conclusion and future works are presented.

1.13 Summary

In this chapter, a brief study was carried out on the evolution of machine vision, components; different types; different applications of machine vision. Accuracy and resolution requirements, laser based manufacturing, machine vision applications in laser micromachining are overviewed. Based on the literature review, research problem was identified and the objectives were defined. The brief structure of the thesis was also explained.

In the next chapter, the important materials and methods necessary for the design and conducting the experiments, total number of experiments with different variable parameters will be discussed.

Chapter 2. Materials and Methods

In this chapter, different materials that are used for conducting the experiment and analysing the results are discussed.

2.1 Laser

PRISMA Nd: YVO₄ 1064-16V a solid-state laser was used for micromachining process. It is a Q-switched laser with both continuous and pulsed output. It has a wavelength of 1064 nm and an adjustable frequency range of 10-100 KHz with constant pulse duration of 14 ns in TEM₀₀ mode. The output power was set by varying the diode current.

It is shown in Figure 2.1 peak power varies with pulse repetition rate of the laser. That is, the maximum peak power is achieved when pulse repetition rate is minimum. In the present work, it is 10 KHz. In the Figure 2.1, 't' is the pulse width, is the duration at which the laser pulse is emitted and 'R' is the pulse repetition rate of the laser. Machining was performed with laser frequency of 10 KHz and an average power of 3.1 W to 4.9 W. These parameters were maintained constant throughout the experimental process.

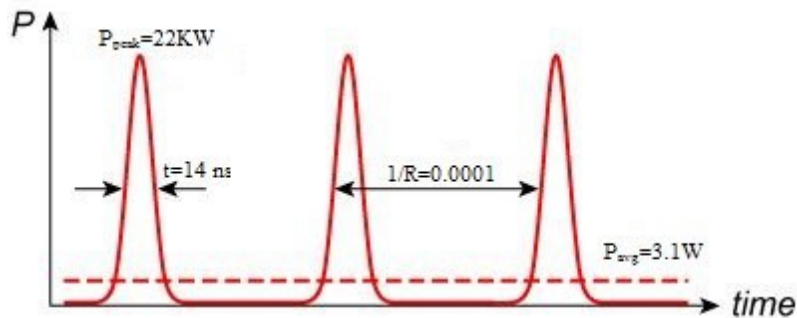


Figure 2.1 Temporal profile of the laser power[56]

2.2 Opto Mechanical Components

The optical setup required for machining process consists of a telescopic lens attached to the laser aperture, galvoscaner, converging lens and a fixture to hold the samples. The laser beam from the telescopic lens should pass through the galvoscaner and the converging lens at their centre so that maximum scanning range can be achieved. It is very important fact to be considered that all the

optics should be at the same height. Figure 2.2 shows the experimental setup of the micro machining process.

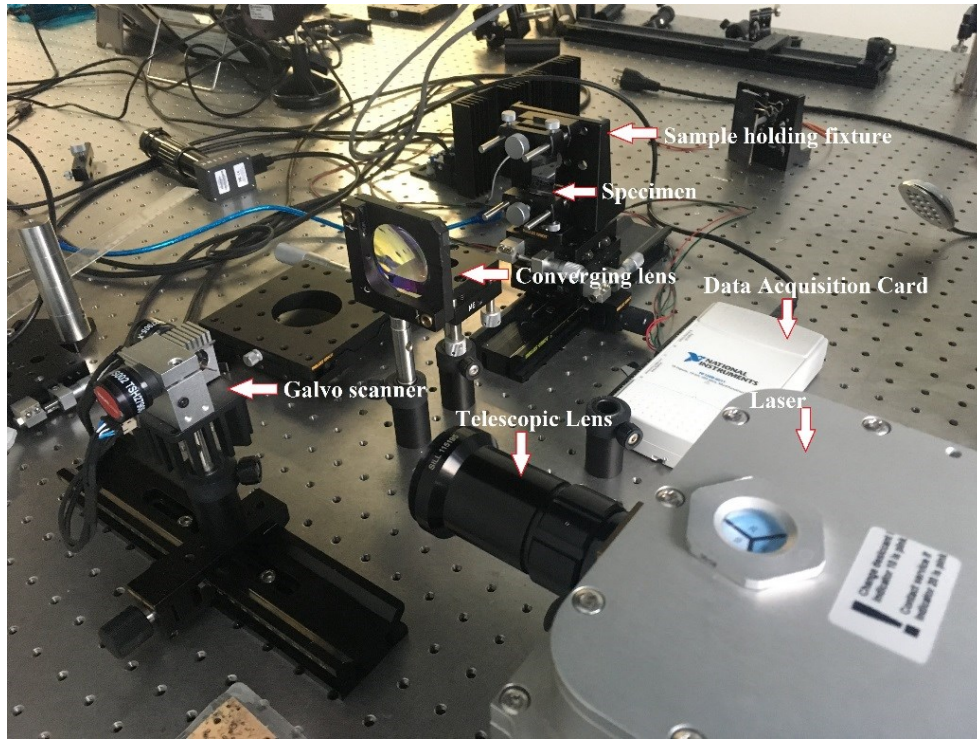


Figure 2.2 Laser micromachining experimental setup

A telescopic lens with 6X magnification is attached to the aperture. The laser beam diameter can be varied from 0.8 mm to 5 mm. According to equation 2.1, to attain minimum spot size (d) the laser beam diameter (D) from the telescopic lens should be set at the maximum limit, which is 5 mm.

$$d = 1.27f\lambda/D \quad \text{Eq. 2.1}$$

where, ' f ' is the focal length and ' λ ' is the wavelength of the laser. A 150 mm focal length lens was used to reduce the laser beam diameter from 5 mm to 40 microns. With fixed values of λ at 1064nm and D at 5mm, it is clear that only possible way to reduce the spot diameter (d) is by using a lower focal length lens. If we use the lens with a focal length less than 150mm, the lens has to be brought closer to the galvoscaner, which results in the reduction of the scanning range. Hence, from all these factors 40 microns was concluded to be the least possible spot size ' d ' for this setup. Figure 2.3 shows the schematic of the laser micromachining set up.

In order to control the movement of laser on the specimen, THORLABS GVS002 galvoscanners were used. The system consists of two silver-coated mirrors each attached to a servo DC motor. The servomotors are controlled with a NI6211 USB DAQ card. The angular position of the mirrors depends on the analog input voltage to the motor. Hence, the motor's position to the desired angle can be controlled. The analog voltage for the system ranges between -10 to +10 and the corresponding range of motion of each motor is in between -12° to $+12^{\circ}$. Hence, we have total 24° of motion, which provides a resolution $1.2^{\circ}/V$. The DAQ is fitted out with two analog outputs, which provide the desired set points for motors. Schematic of the scanning length associated with the galvo mirror rotation is shown in Figure 2.4.

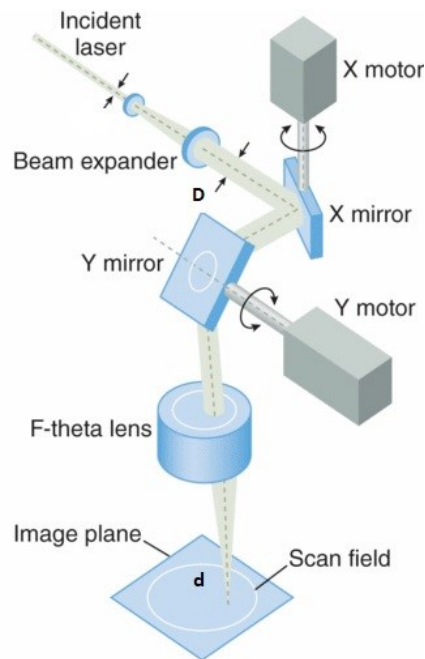


Figure 2.3 Schematic of the Laser micromachining set up[57]

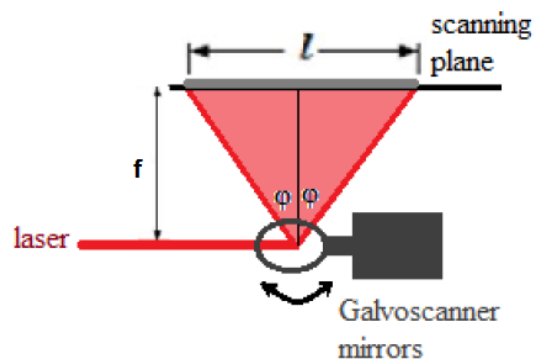


Figure 2.4 Schematic of the scanning length associated with the galvo mirror rotation[56].

In order to find the rotation speed of the galvoscaner, Equation 2.2 was used. By using this equation, the degree equivalent of the pulse pitch, which defines the scanning speed, is calculated.

$$L = 2f \cdot \tan \varphi \quad \text{Eq. 2.2}$$

From Equation 2.2, L is the scanning length, f is the distance between the galvoscaner and the lens, and φ is the rotation angle of the galvomirror. $\varphi = \text{Arctan} (L/2f)$ Where $f = 1.5 \times 10^5 \mu\text{m}$ (distance from galvo mirrors to converging lens) therefore, $\varphi = \text{Arctan} (L/3 \times 10^5)$. For instance, considering the designed experimental setup with a 0% overlap, the pulse pitch is calculated from Equation 2 to be $L = 40 \mu\text{m}$ therefore, degree equivalent of $40 \mu\text{m}$ is:

$$\varphi = \text{Arctan} (40/3 \times 10^5) = 7.6 \times 10^{-3}^\circ \text{ and voltage} = 6.3 \times 10^{-3} \text{ volt}$$

Therefore, in order to obtain a texture pattern with 0% overlap, the corresponding value of the pulse pitch is 6.3×10^{-3} volt. From this proportionality, we can find that:

$$1 \mu\text{m} \sim 1.6 \times 10^{-4} \text{ volt.}$$

SG 90 9G micro servo motor with an operating speed of 0.1second/600 was used in the experimental setup. The sample was attached with a special fixture to the servomotor to change the angular positions of the sample as and when required. Servo can rotate approximately 180 degrees (90 in each direction). Beam splitter was used to capture images of the reflected specimen surface.

2.3 Camera and lens

PixeLINK industrial machine vision camera with 2.3 Megapixels (1920×1200), 165 frames per second at full resolution, USB 3.0, CMOS (global shutter), 1/1.2", with an effective pixel size of $5.86 \times 5.86 \mu$ was used for the imaging.

In the present work, the images were captured with camera's full resolution i.e. 2.3Megapixels with an exposure of 3 Seconds, Gain of 6dB, 90% saturation and white balance in the ratio of 1.5 : 1 : 3(R:G:B). All these camera parameters are maintained constant throughout the experimental works. The InfiniProbe™ MS C-mount Variable Magnification Lens is attached to the camera which provides high resolution and low distortion images. It has a 0 – 4X range focusing from ∞

to 16mm. With the resolution of 1920×1200 at a distance of 65mm from the imaging plane, the field of view for this setup is 37.8mmX23.53mm.

2.4 Silicon wafer

The samples used in this work were p-type (Boron-doped) multicrystalline silicon (mc-Si) wafers with resistivity of 0.02 Ω -cm and thickness of 700 micron. These wafers were cut into 20mm × 50mm rectangular pieces and laser micro machining was carried out on these specimens.

2.5 Software for control

MATLAB algorithms has been developed to control the output voltage of the DAQ card and there by controlling the galvo mirror positions. Processing of the captured images before and after machining was also done in MATLAB. Arduino was used to control the rotation of micro servomotor. This helped in rotating the specimen automatically to exact angles for the repetitive micromachining. While capturing the image, PixeLink Software Development Kit (SDK) was used to control the different features of the camera such as gain, exposure and orientation.

2.6 Interferometer

WYKO NT1100 interferometer was used to determine the surface profile and roughness of the samples. (Figure 2.5). This instrument works on the principle of optical phase-shifting and white light vertical scanning interferometry. Three-dimensional, non-contact and surface profile measurements can be carried out. It employs Wyko Vision® software running under Microsoft® Windows XP®. It has a vertical measurement range from 0.1nm to 1mm. The uniformity of the machined surface was determined by observing measured data such as the surface profile, depth of machining and the roughness pattern.

2.7 Experimental Setup

The primary aim is to design a machine vision system for precision laser micromachining. To guide the laser beam on the substrate, a MATLAB algorithm has been developed to convert the desired coordinates of the geometry to the galvoscaner's motors angle. Based on the area to be

machined the maximum and minimum analog input voltages are calculated. Equation 2.3 represents the relation between the maximum displacement and the DC motor angle.

$$\alpha = \tan^{-1}\left(\frac{x}{f}\right), \beta = \tan^{-1}\left(\frac{y}{f}\right) \quad \text{Eq. 2.3}$$

where x and y are the coordinates in x and y directions and f is the focal length of the lens. The MATLAB algorithm is programmed in such a way that, it must have competence to get the different percentage of overlap and repetition rate.

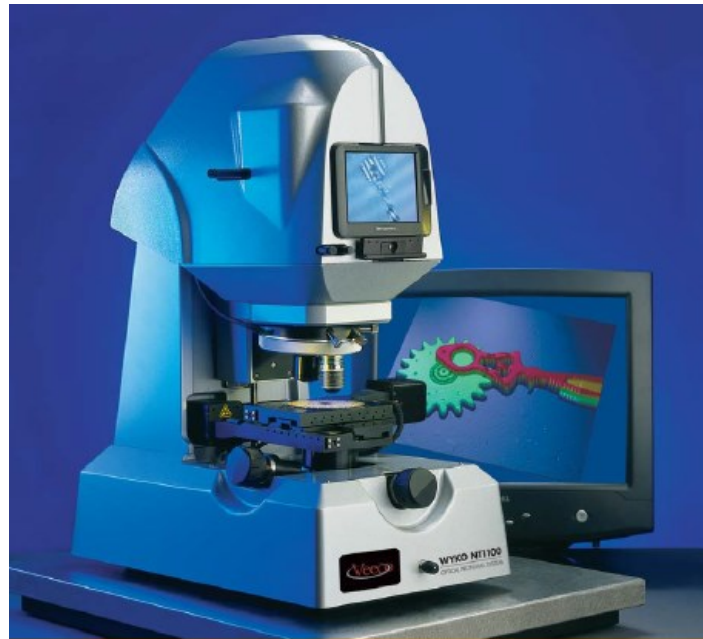


Figure 2.5 Wyko NT1100 Optical Profiling System[58]

Using Eq.2.3, we calculated the set of motor angles, which later converted into the DC motors voltages by multiplying $0.83V/^\circ$ coefficient. Once the desired voltages were calculated, the series of voltage values were imported to the data acquisition (DAQ) card. Different overlaps were calculated by using the equation 2.4.

$$Ov = d * (1 - Op) \quad \text{Eq. 2.4}$$

where Ov is the overlap, d is the spot diameter of the laser and Op is the percentage overlap. Initially the dimensions of the specimen and the corresponding path functions are defined. When the laser spot movement is only in the x or y direction, the distance between the two adjacent spots

is constant. However, if the machining path follows the complex geometry, the slope of the curve must be obtained at each instant during machining in order to find the distance between each spot and the overlap calculations. With the present algorithm, the slope of the path function was extracted. Based on the extracted slope, x and y steps of the laser movement has been calculated and converted into the voltages. These analog voltages were sent to the DC motors by using DAQ card with specified sampling rate for machining.

Figure 2.6 illustrates the voltage of X and Y DC motors for 30 percent overlap when the repetition rate of laser and sampling rate of DAQ are 10K. Once the desired voltages were calculated, the series of voltage values were imported to the data acquisition (DAQ) card. Since, the purpose of the micromachining in this work is to machine the curved and complex shapes also; the presented algorithm has the capability of machining curved structures. Figure 2.7 shows the voltages of X and Y DC motors to machine a 3 mm circle with 30 percent overlap. It can be observed that, to have 30 percent overlap for machining a circle of the 3 mm, the number of laser spots N should be 672 based on the following calculation (Eq. 2.5)

$$N = \frac{2 \times \pi \times r}{D \times (1 - Op)} = \frac{2 \times \pi \times 3mm}{0.04mm \times (1 - 0.3)} = 672 \quad \text{Eq. 2.5}$$

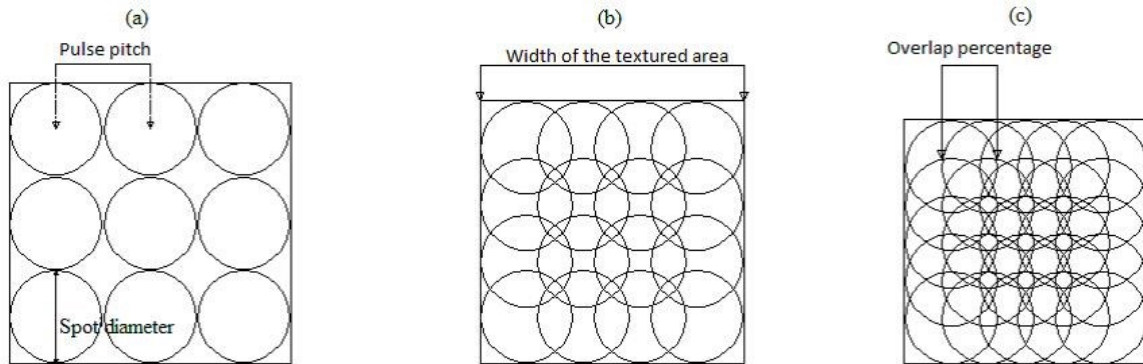


Figure 2.6 Schematic of the mc-Si samples textured under three different overlap values, (a) 0%; (b) 30%; and (c) 60%.

Figure 2.7 shows the developed algorithm that could find the laser displacement in x and y directions for different complex curves. With the presented algorithm, the slope of the path function was extracted. Based on the extracted slope the x and y steps of the laser movement was calculated.

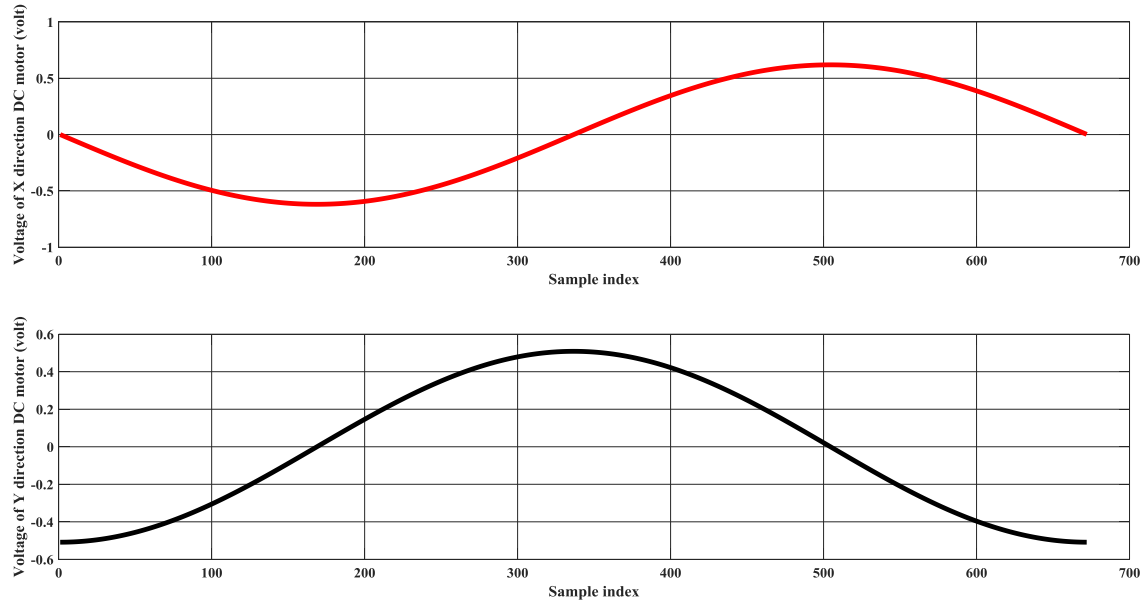


Figure 2.7 X and Y DC motors voltages to machine 3mm circle with 30 percent overlap

The above-described algorithm is to control the laser for machining. Other set of algorithms were developed in the MATLAB for coordinate extraction using image-processing technique. The experimental setup for the machine vision consists of a camera, lens, source of light, beam splitter and white screen. The camera is attached with a C mount lens with variable magnification from 0 to 4X. The laser light, converging lens, beam splitter and the sample are arranged in the straight line as shown in the Figure 2.8. Camera, beam splitter and the screen are arranged on the other axis exactly perpendicular to the laser axis. The distance between the camera lens and the beam splitter is fixed at 35mm. The distance between the screen and beam splitter is fixed at 105mm and the distance between the sample and beam splitter is fixed at 90mm. The idea is to capture the image by utilizing the reflected light rays from the sample and the screen that converges at the beam splitter.

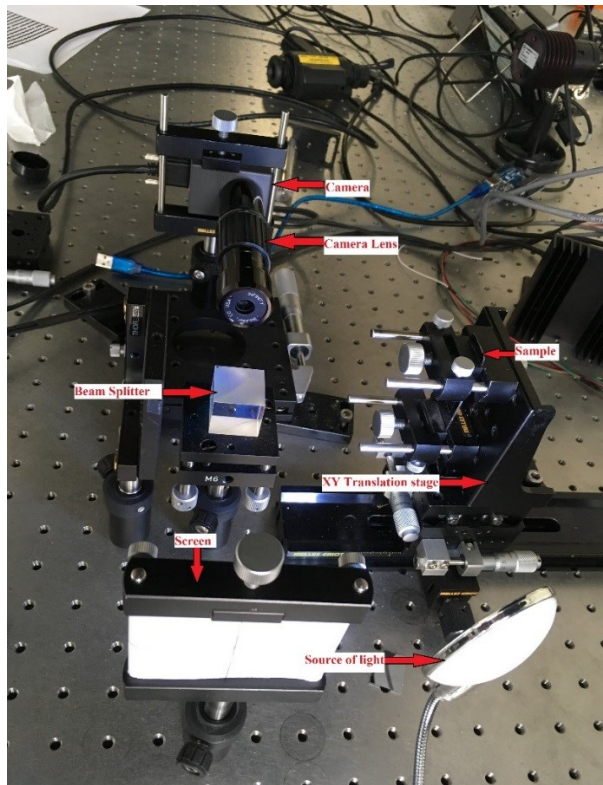


Figure 2.8 Experimental set up for machine vision

Arduino controlled micro servomotor is shown in the Figure 2.9. The sample is fixed to the servomotor through the special fixture. The input to the motor in terms of angles are given through the Arduino software.

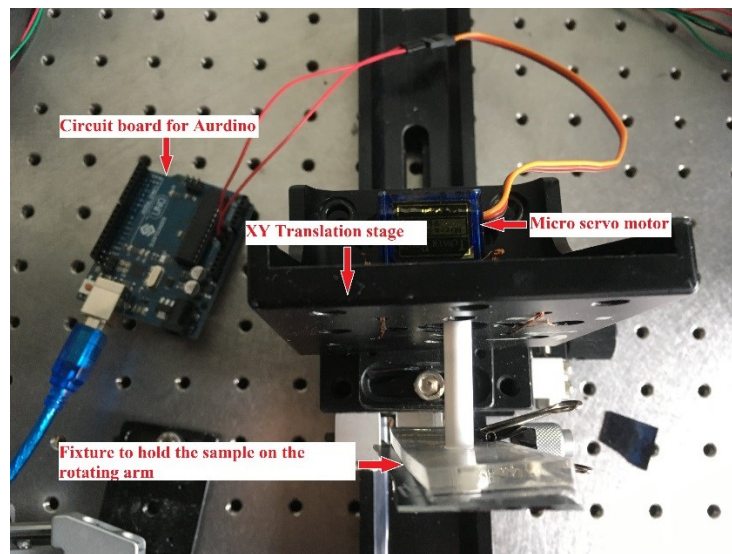


Figure 2.9 Servomotor and the sample holder

2.8 Design of experiments

In the first set of experiments, the geometrical coordinates of the designed shape are extracted and machined on the silicon wafer specimen using a high repetition rate Nano second laser. Known magnitudes of translational and rotational movements were given to the specimen. The images of machined area are captured before and after transformation.

MATLAB algorithm, which was programmed based on linear algebraic calculations, processes the images to find the initial point of machined area on the transformed specimen. The laser beam is guided to that point and the machining is repeated. To validate the repeatability of the process, the specimen was measured under microscope to find the errors between the former and latter machined paths.

To control the laser on the specimen and to analyse the captured images before and after transformation, a MATLAB algorithm was developed using an image processing toolbox. In the beginning, input parameters such as, spot diameter is fixed at 40 microns; the distance of the specimen from the lens was fixed at 150mm. The dimensions of the quadrilateral, scaling factor and percentage of overlap were parameterised. The overlap calculation was already explained earlier.

The machining was carried out using the laser. Once the machining was over, by using machine vision set up the image of the machined sample was taken. Without disturbing the machine vision setup, the translational and rotational movements were given to specimen. After the transformation, another image of the sample was captured. Both the images were then imported into MATLAB. Figure 2.10 shows the captured images of the sample before and after the rotation.

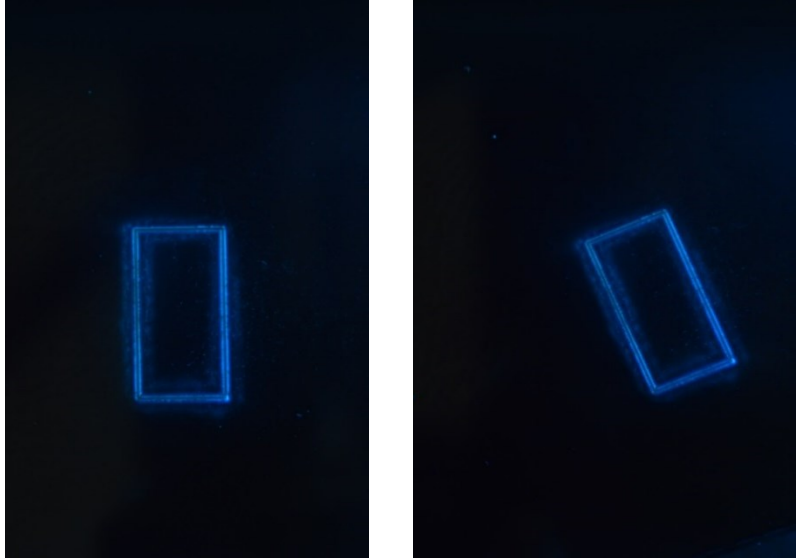


Figure 2.10(a) Sample before rotation (b) Sample rotated 30 degrees

The resolution of the image was calculated. This step is necessary for the reconstruction of the geometry in the later stages. We know the dimensions of the specimen in terms of distance. For the calculations we need the number of pixels corresponds to that distance. It was found out with an image viewer tool in MATLAB. Once the pixel data is known in the form of matrix, both the images are compared to calculate the transformation. The comparison was done by selecting the two pixels along the length of the geometry. First pixel corresponds to starting point of the machining and the second one corresponds to the direction of machining. The selections were made in both the images. The translation was calculated by taking a difference of the pixel data of selected points. Finding the difference in columns gives the horizontal translation and difference in the rows gives the vertical translation. The angle of rotation was calculated by taking tangent of the angle between the corresponding selected points from both the images. We found out the magnitude of the displacement and rotation. We need to send the laser to the transformed position. This was done by adding the translations to the first matrix and angular displacement was added by multiplying the transformation matrix with the image data matrix of the first image. We got the new matrix in terms of pixels data. To get the coordinates in the real world for laser machining, we need to multiply the resolution the image with resultant matrix. The machining was performed on the sample again, the errors corresponds to former, and latter machined paths were tabulated and discussed.

In this section, 27 experiments were conducted. 18 experiments were conducted by moving the specimen at the distances (9 in X direction and 9 in Y direction) 6mm, 10mm and 13mm in horizontal and vertical directions. Three sets of three experiments (total 9) were conducted for the rotation. The angles of rotations used are from 30^0 to 80^0 . For translation $4mm \times 6mm$ rectangles and for rotation $4mm \times 8mm$ rectangles were machined. Known magnitudes of translations were given to specimen using XY stage and rotations were given using a servomotor.

In the second set, to analyse the effect of different process parameters on the depth and roughness of the laser-textured surface, a rectangular shape with dimensions of 5mm by 3mm was textured on the silicon wafer specimen. Series of experiments were conducted with different laser power and DAQ sampling rate. Initially the experiments were conducted with five different laser powers (at 2.9W, 3.1W, 3.68W, 4.57W and 4.87W) and three different percentage overlaps (at 0%, 30% and 60%). The frequency of the DAQ was maintained constant at 10 KHz. Later, the average power of the laser was maintained constant at 3.68W. The sampling rate of the DAQ card was varied for three different overlaps in different coordinate axes and the roughness was measured.

In the third set of experiments, to analyse the best approach for the extraction of coordinates of the complex geometry, curved shapes such as circle, sine function and a microfluidic channel were machined on the silicon wafer specimen with 3 different percentage overlaps. In the Table 2.1, the list of experiments conducted and the variables considered are shown.

2.9 Summary

In this chapter, experimental setup and major components that were used for conducting the experiments and their technical details are explained. The design and development of algorithms for laser micromachining and image processing based algorithm are addressed. The description of the total number of experiments that were conducted by varying different process parameters are also explained. In the next chapter, preliminary results from the first set of experiments will be discussed. Different types of errors that occurs during machining of transformed samples will be addressed.

Table 2.1 List of experiments and the variables

<i>Sl No</i>	<i>Experiment</i>	<i>Variables</i>	<i>Total</i>
<i>a</i>	<i>Sampling rate of DAQ at 2KHz, 5KHz and 10KHz</i>		
<i>1</i>	<i>Texturing rectangle of 5mmX3mm with constant power at 4.87W</i>	<i>X Direction - 0% overlap</i>	<i>3</i>
<i>2</i>		<i>X Direction - 30% overlap</i>	<i>3</i>
<i>3</i>		<i>X Direction - 60% overlap</i>	<i>3</i>
<i>4</i>		<i>Y Direction - 0% overlap</i>	<i>3</i>
<i>5</i>		<i>Y Direction - 30% overlap</i>	<i>3</i>
<i>6</i>		<i>Y Direction - 60% overlap</i>	<i>3</i>
<i>7</i>		<i>XY Direction - 0% overlap</i>	<i>3</i>
<i>8</i>		<i>XY Direction - 30% overlap</i>	<i>3</i>
<i>9</i>		<i>XY Direction - 60% overlap</i>	<i>3</i>
<i>b</i>	<i>Laser power varied at 2.9W, 3.1W, 3.68W, 4.57W and 4.87W</i>		
<i>1</i>	<i>Texturing rectangle of 5mmX3mm with constant DAQ sampling rate at 10KHz</i>	<i>X Direction - 0% overlap</i>	<i>5</i>
<i>2</i>		<i>X Direction - 30% overlap</i>	<i>5</i>
<i>3</i>		<i>X Direction - 60% overlap</i>	<i>5</i>
<i>4</i>		<i>Y Direction - 0% overlap</i>	<i>5</i>
<i>5</i>		<i>Y Direction - 30% overlap</i>	<i>5</i>
<i>6</i>		<i>Y Direction - 60% overlap</i>	<i>5</i>
<i>7</i>		<i>XY Direction - 0% overlap</i>	<i>5</i>
<i>8</i>		<i>XY Direction - 30% overlap</i>	<i>5</i>
<i>9</i>		<i>XY Direction - 60% overlap</i>	<i>5</i>
<i>c</i>	<i>Displacement of the sample</i>		
<i>1</i>	<i>Transformation of the rectangle 4mmX8mm and 4mmX6mm</i>	<i>X direction at 6mm,10mm and 13mm</i>	<i>9</i>
<i>2</i>		<i>Y Direction at 6mm,10mm and 13mm</i>	<i>9</i>
<i>3</i>		<i>Rotation of the sample in 30, 50 and 80 degrees</i>	<i>9</i>
<i>d</i>	<i>Different percentage overlap at 0%, 30% and 60%</i>		
<i>1</i>	<i>Coordinate extraction of curved shapes</i>	<i>Function based- Sinusoidal function</i>	<i>3</i>
<i>2</i>		<i>Function based- Circle</i>	<i>3</i>
<i>3</i>		<i>Function based-Microfluidic channel</i>	<i>3</i>
<i>4</i>		<i>Image based- Sinusoidal function</i>	<i>3</i>
<i>5</i>		<i>Image based- Circle</i>	<i>3</i>
<i>6</i>		<i>Image based-Microfluidic channel</i>	<i>3</i>
	<i>Total</i>		<i>117</i>

Chapter 3. Preliminary Results and Analysis of Errors

Laser micromachining is precision manufacturing process in which accuracy and repeatability are the two important factors to be considered. In the previous chapter, the algorithms were designed to carry out the experiments by transforming the sample from its initial position to a new position with a varied orientation and displacement. To achieve the repeatability of machining, a rectangular shape was machined and after the transformation of the sample, the laser must reach the new position of the sample and carry out the machining. To estimate the accuracy of machining, the difference in the laser paths for repeated machining on the same sample are analysed. To estimate the propagation of errors, known amount of translational variations and angular variations were given to sample. After the experiments, the machined samples were measured under the digital microscope to determine the errors. Translational errors and angular errors are measured for various transformation of the sample. The average of the obtained errors are plotted to analyse the effect of sample movement on the propagation of errors. Figure 3.1 Measured 4mmX8mm sample for errors shows the measured errors under the microscope for the sample rotated to 30° with respect to X-axis.

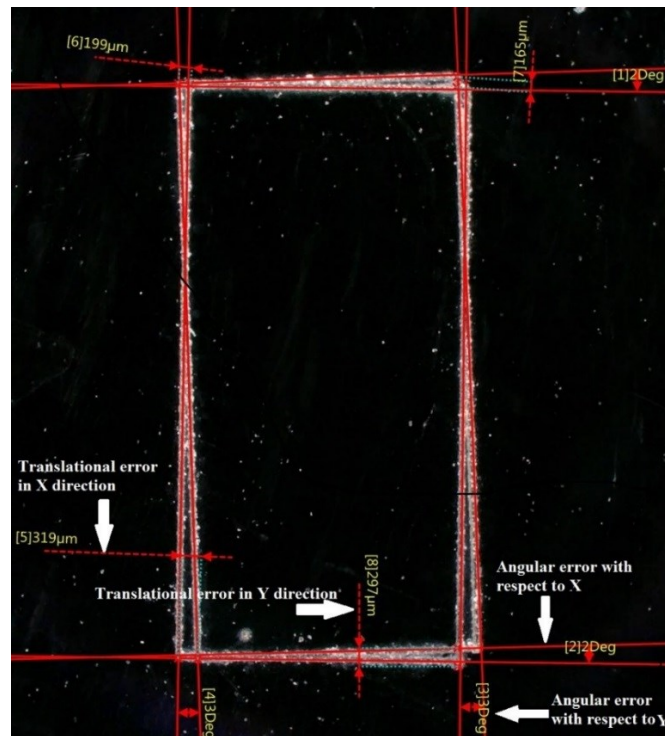


Figure 3.1 Measured 4mmX8mm sample for errors

3.1 Angular shift

As discussed in the previous chapter, the experiments were conducted for the repeatability of micromachining process by extracting the coordinates of the transformed geometry. In this section, different angular transformations such as from 30° , 50° and 80° rotations were given to the sample. A micro servomotor was used for the rotation of the sample. The translational and rotational errors occurred between the former and latter machined paths were measured using the captured images. Three set of experiments were conducted by giving rotations in both directions. The average of the measured errors are plotted in the Figure 3.2 Figure 3.3

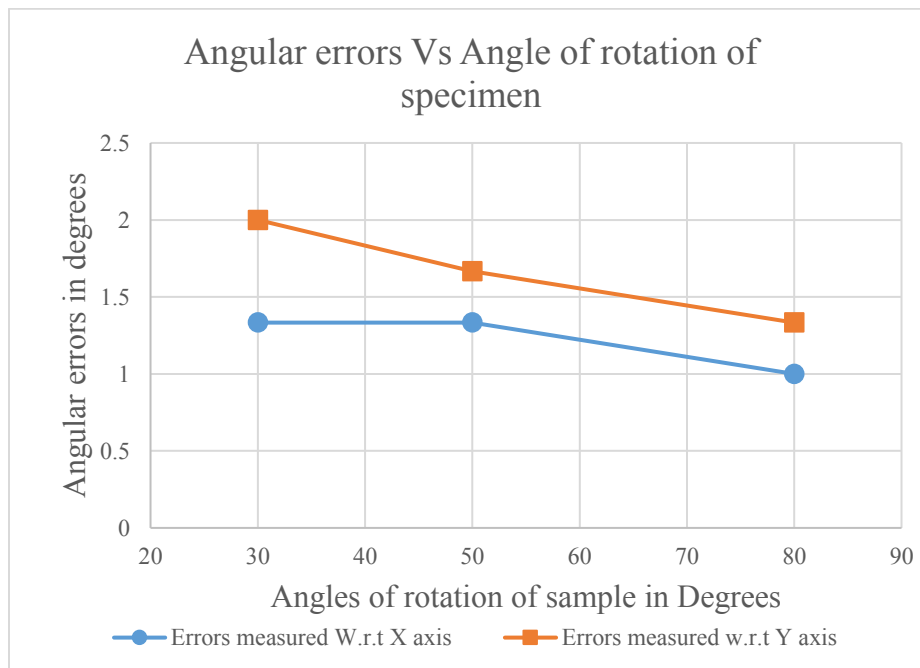


Figure 3.2 Angular errors Vs Angle of rotation of 4mmX8mm sample

In the Figure 3.2, the graph is plotted with X axis as the input angles of rotations of the sample and in Y-axis as the measured errors. With reference to Figure 3.1 after the transformation, the variations in angles measured from the 4mm side of the sample is referred as the errors with respect to X axis and the variations in angles measured from the 8mm side of the rectangular sample is referred as the error with respect to Y axis. It can be observed that, error propagation in both X and Y directions for different angles of rotation of the sample follow the same pattern with small variation. They have the maximum angular errors of 1.33° with respect to X-axis and 2° with respect to Y-axis at 30° and minimum values of 1° and 1.33° at 80° respectively.

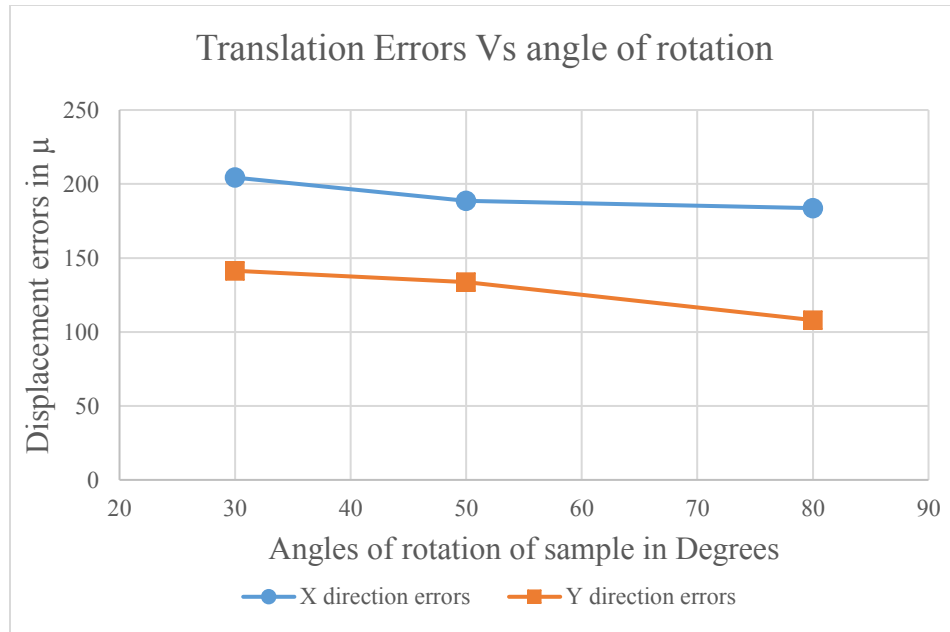


Figure 3.3 Translation Errors Vs Angle of rotation of 4mmX8mm sample

Figure 3.3 shows the translational errors in X and Y directions for different angles of rotation of the sample. The graph is plotted with Y-axis as the displacement of the sample in microns and X-axis as the angles of rotation of the sample. With reference to Figure 3.1, Translational errors are measured as the variations in distance moved between the initial and latter machined paths. The distance moved with respect to 8mm side of the sample is the X-axis translational error and the distance moved with respect to 4mm side of the rectangular sample is the translational error in Y direction. X and Y-axis translational errors are maximum for 30⁰ rotation of the sample with 204μ in X direction and 141μ in Y direction. Both X and Y-axis translation errors follow the similar characteristic curve with X direction errors having a higher magnitude for all angles of rotation.

3.2 Translational Shift

In this section of the experiments, once the machining is over, the images of machined sample were taken and the sample was moved in both x and y directions. Displacements were given to sample at 6mm, 10mm and 13mm in both axis. After translation, another image of sample was taken and compared with the previously captured image. With the MATLAB algorithm, we got the transformed coordinates of the sample and machining was repeated. Errors between former and latter machined paths were measured. Measurements were divided into errors in angle (vertical

and horizontal) and errors in displacement (x axis errors and y-axis errors). Three set of experiments were conducted in this section. Average of the measured errors were considered and plotted in the below section.

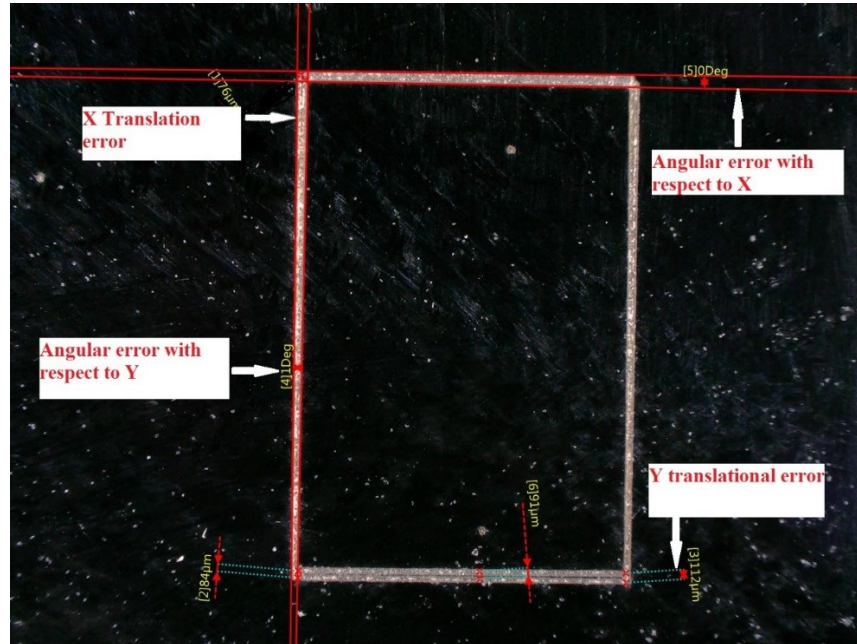


Figure 3.4 Measured 4mmX6mm sample for errors

Figure 3.4 shows the measured 4mmX6mm sample machined for analysing the errors for the translational movements given to the sample. With reference to Figure 3.4 after the transformation, the variations in angles measured from the 4mm side of the sample is referred as the angular errors with respect to X axis and the variations in angles measured from the 6mm side of the rectangular sample is referred as the error with respect to Y axis. With reference to Figure 3.4, Translational errors are measured as the variations in distance moved between the initial and latter machined paths. The distance moved with respect to 6mm side of the sample is the X-axis translational error and the distance moved with respect to 4mm side of the rectangular sample is the translational error in Y direction.

In the Figure 3.5 the graph is plotted with X as the distance of the sample moved in X direction and in Y-axis as the measured angular errors. It can be observed that, the angular errors occurred in X and Y directions for the sample moved in X direction is constant for all the distances.

The errors exactly coincide in x and y direction, which can be seen as an overlapping plots in the Figure 3.5.

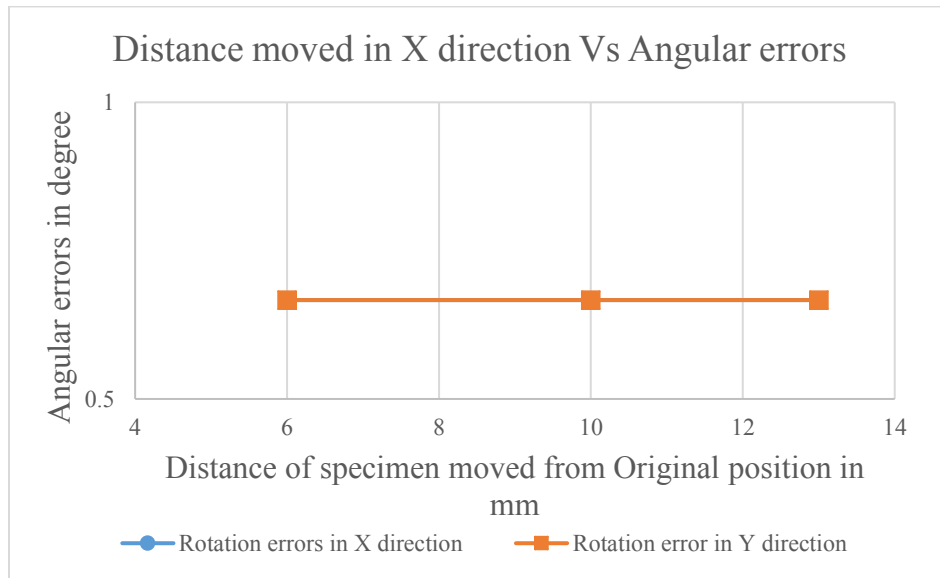


Figure 3.5 Distance moved in X Direction Vs Angular errors

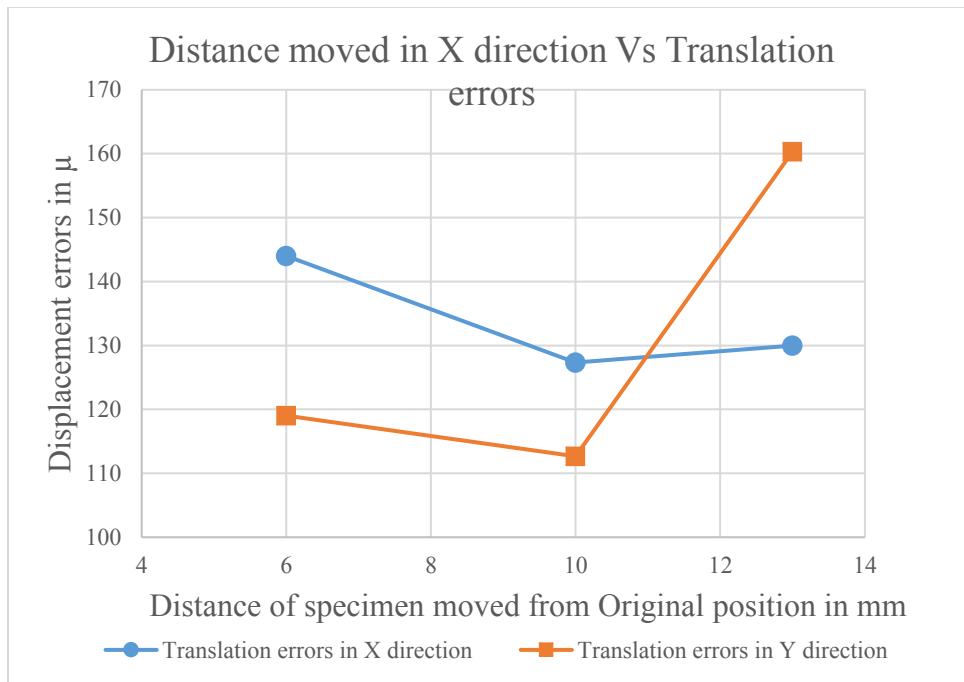


Figure 3.6 Distance moved in X direction Vs Translation errors

The Figure 3.6 shows the translational errors when the sample is moved in the X direction. The graph is plotted with X as the distance of the sample moved in X direction and in Y-axis as the

measured translational errors. It can be seen that, the translation errors in X direction are higher for the distance of the sample moved to 6mm and 10mm. But for the 13mm shift of the sample, average values of errors increases in Y direction and reaches maximum value of 160.3μ .

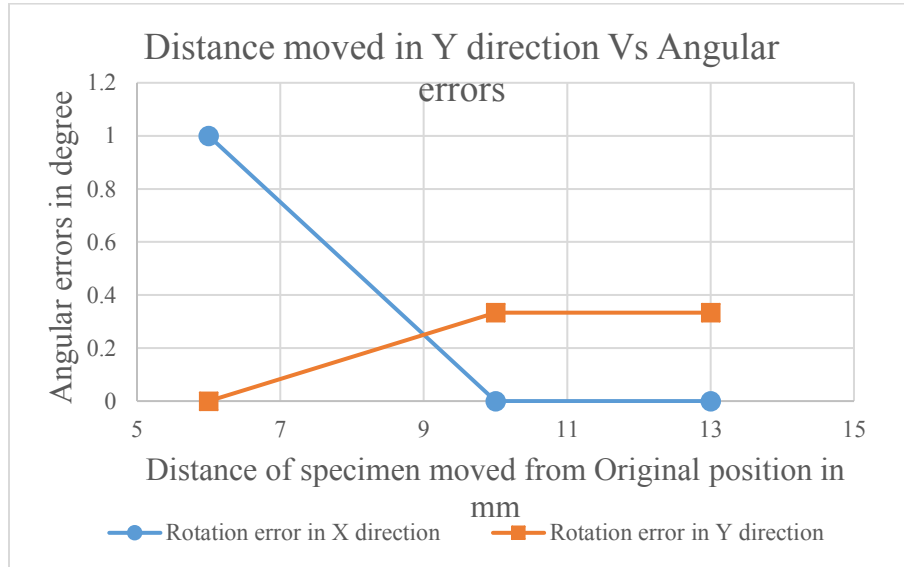


Figure 3.7 Distance moved in Y direction Vs Angular errors

In Figure 3.7, the angular errors in vertical and horizontal directions for the displacement of the sample in Y direction are plotted. As like in the X direction error measurements, displacement variations were given to sample in both directions of Y-axis from 6mm to 13mm. It can be observed that, the X direction angular error was maximum for the 6mm and it reduced to zero degrees for 10mm and 13mm displacement of the sample. On the other hand, Y direction angular errors were zero in the beginning at 6mm, increased to 0.33 degree, and remained constant value for 10mm and 13mm.

The variation in the X and Y direction translational errors for the sample moved in Y directions is displayed in the Figure 3.8. It can be observed that the propagation of translational errors in x and y directions follows the same pattern. At 6mm displacement of the sample in y direction, errors are maximum in both x and y directions, as the distance of the increases, the errors in both x and y directions started reducing and reached minimum value at 13mm.

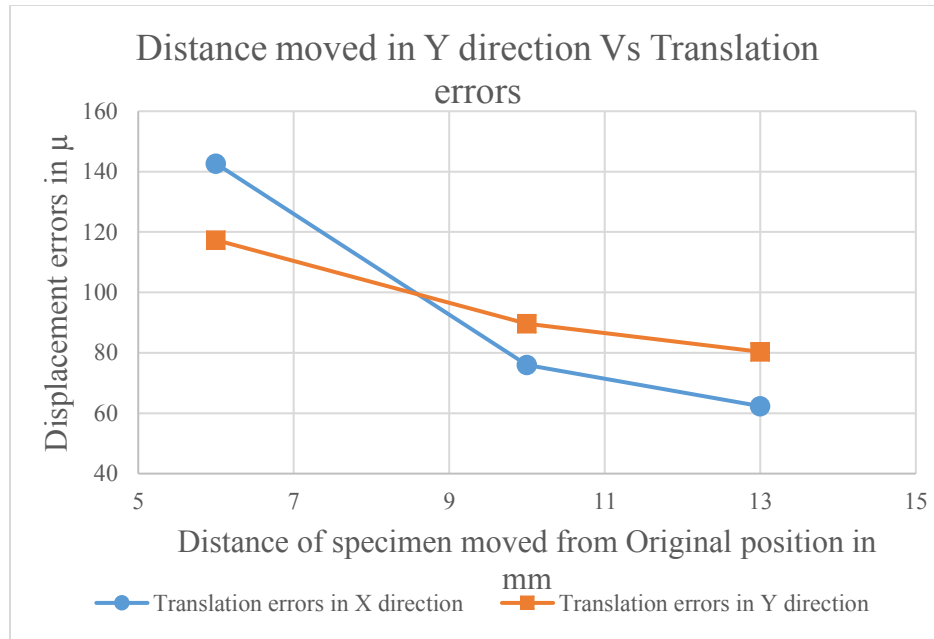


Figure 3.8 Distance moved in Y direction Vs Translation errors

3.3 Error reduction strategies

As seen from the above-plotted graphs two different types of errors that can occur which are translational errors and angular errors. It was discussed earlier that, we have to choose two pixels to begin the extraction of transformed coordinates. One corresponds to the starting point of the geometry and another pixel corresponds to the direction of the path that the geometry follows from the starting point. Therefore, selection of improper pixels is major source of the generation of errors. Selection of wrong pixel at the starting point of the geometry results in translational errors and the selection of wrong pixel along the path i.e., the second pixel results in the angular errors. Care should be taken while selecting the right pixel. It also depends on the resolution of the captured images. Higher the resolution, lesser will be the chances of making errors in selection of right pixel. We are operating with a laser of 40μ spot diameter and the size of each pixel of the image sensor we used was 5.32μ . Therefore, there will be almost 7 pixels corresponds to each spot of laser. While selecting the starting point of the machining path, we have to select centre pixel and to indicate the direction of the path, we have to select the pixel exactly in line with the pixel, which was selected earlier. If there is variation in the selection of one pixel, the machining path changes and the error propagate along the length of machining path. This can be avoided by

developing the advanced algorithm to choose the exactly centre pixel for whatever the manual selection.

Focussing also plays a major role in selection of pixel; from the Figure 3.9, it can be observed that, as the image goes out of focus it will become more difficult to select the exact pixel for the machining. It can be avoided by using the autofocus lenses, which automatically capture the sharp images. In addition, image-enhancing features like filtering of the image, increasing the dynamic contrast range and focus-sensing techniques can be employed to make the pixel more clearly visible for the manual selection of pixels. Some of the advanced techniques such as automatic edge and corner detection techniques can be used. For this setup, with the laser spot diameter of 40μ , the minimum translational error that we can achieve is 56μ and no angular error.

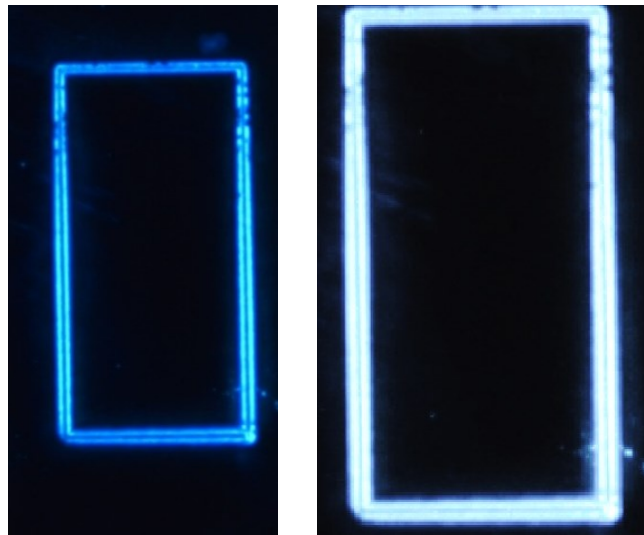


Figure 3.9 Focussed and out of focus images

3.4 Summary

In this chapter, preliminary results that are concerned with measurement of the different types of errors that can occur while machining the transformed coordinates are analysed. For different movements of the sample in X and Y directions and also by rotating the samples the transitional and angular errors were found out. Three set of experiments were conducted for the displacements and rotations of the samples. The graphs were plotted for the average of the three values of the errors. The major sources of errors and the probable solutions to overcome the errors are also

discussed. For this setup, with the laser spot diameter of 40μ , the minimum translational error that we can achieve is 56μ and the angular error can be eliminated.

This chapter is concerned with the extraction of coordinates and error analysis for the simple shape such as rectangle. In the next chapter, a detailed analysis for the extraction of coordinates of the curved shapes in two different approaches and their compatibility to use with the best possible efficiency are analysed.

Chapter 4. Coordinate Extraction of Curved Shapes

Laser micromachining is a technology that facilitates component miniaturisation and is characterised by improved performance. It is widely used across many industries, including semiconductors, electronics, automotive, medical devices, defence/aerospace, instrumentation, communications and renewable energy etc. The distinct feature of laser micromachining is a combination of greater flexibility, contactless machining, and the possibility of automation as well as easy integration. This enables micro processing of many materials including silicon, ceramics, metal and polymer. The laser ablation is a complex process and the exact nature of the interaction differs from material to the material and laser processing parameters. Ablation is usually a combination of evaporation and melt expulsion.

In laser micromachining, it is necessary to analyse the effect of different process parameters on the depth and quality of machining. In the following sections extraction of the coordinates of a geometry in two different approaches and study of the effect of different laser parameters on the roughness of the micro machined surface are discussed.

4.1 Function based approach:

In function-based approach, the coordinates of the geometry to be machined are calculated using first and second derivative of the function. If we consider a microfluidic channel to be plotted, we should know the dimensions of the geometry. In MATLAB, we have to define the geometry with a parameterised lengths and radius.

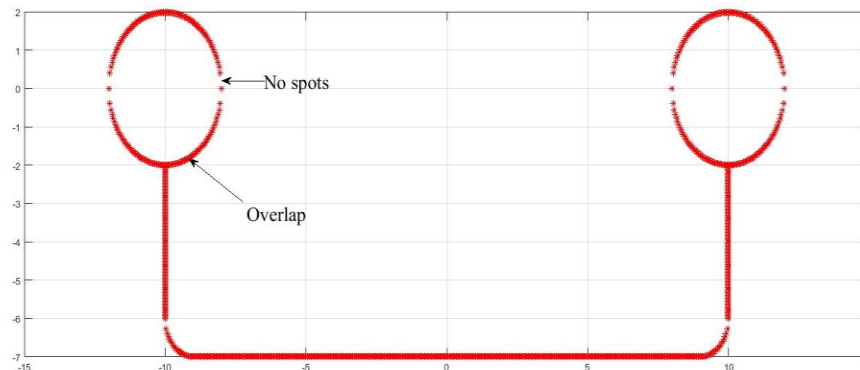


Figure.4.1 Microfluidic channel without interpolation

It can be observed from the Figure.4.1, all the spots are not equally spaced and there are overlaps in certain regions and there are no spots in some other regions of the extracted curve. To extract the adjacent points, slope has to be found out at each instant. In curved surfaces, the slope will be too high so that for small change in the value of x coordinate, there will be huge change in the value of y coordinate and vice versa. As a result, we miss the points in the high slope regions and similarly in the lesser slope regions, we get overlap. For the cases where the overlap is not desired this is a drawback and the machined profile will not be uniform. So in order to avoid this, we developed an algorithm to make the laser spots equidistant along the length of the curve to achieve zero overlap. The schematic representation of the developed algorithm is shown in the Figure 4.2.

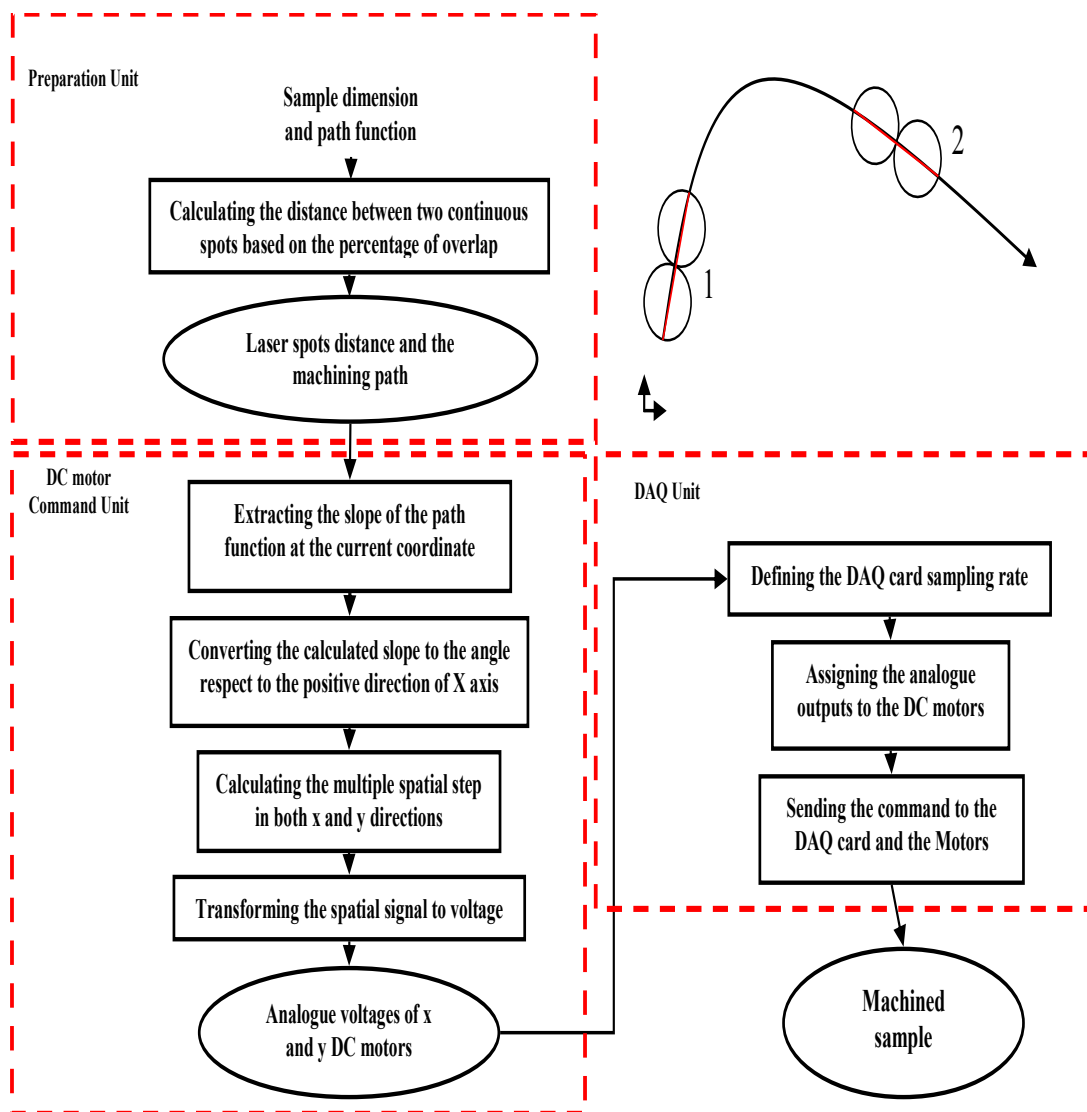


Figure 4.2 Schematic of the developed algorithm for curved shapes

The algorithm interpolates the new points at any fractional point along the length of the curve. In the beginning, we have to define the number points to be generated along the arc length. Then the algorithm calculates how many points to be interpolated and how many already exist on the curve itself. By integrating each segment and summing the results, it generates the total arc length along the curve. An ODE solver in MATLAB will carry out the integration of the each segment. The improved version with the equidistant points is as shown in the Figure.4.3. We have also tried with the sine function and circle for the conformity of the equidistant points and got the desired results.

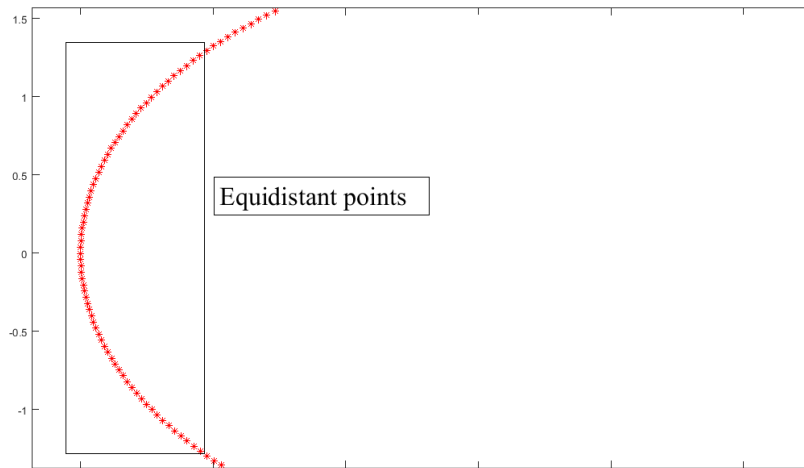


Figure.4.3 Equidistant points after interpolation

4.2 Image based approach

To check the feasibility of the image processing based algorithm, similar microfluidic channel was drawn and tried to extract the coordinates. When the image is imported into the MATLAB, the number of pixels in x, y directions are calculated, and the corresponding specimen size to be machined are noted down. Then the ratio of the actual size of the specimen and the corresponding size of the specimen in the image in terms of pixels are taken. Required percentage overlap, scaling factor are given as input parameters. The imported image in RGB is converted into grey scale and then into binary image. In the binary image, the program looks for all the edges by canny edge detection tool. Now, the edges of the specimen are created. These edges are then machined in similar way as we did in the function-based approach. The images of the sine function and circle were also machined with this algorithm.

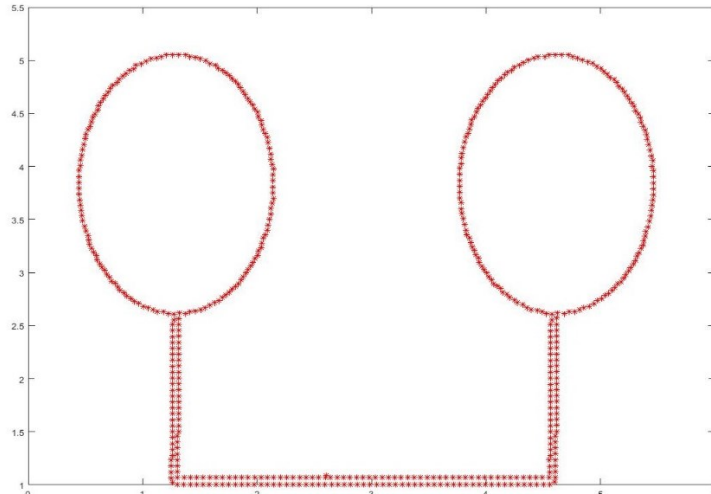


Figure.4.4. Image based coordinate extraction

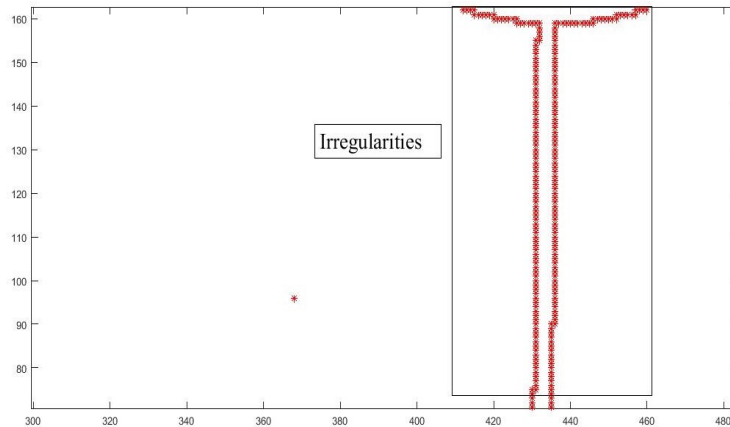


Figure.4.5 Irregularities in the extracted curves

From the Figure.4.4 and Figure.4.5, it can be observed that the coordinates extracted from image processing approach are not uniform. This is due to the resolution of the image. Higher the resolution more uniform the extracted coordinates are. However, increased resolution leads to higher computational cost.

From above discussed methods, function based approach is more accurate. Overlapping was the only issue, which was solved by an interpolation algorithm to achieve the equidistant points along the length of the curve. On the other hand, image processing based approach is more convenient to use, as there is no tedious process of writing the mathematical functions and calculating their derivatives to find the required coordinates. With a single algorithm, any image can be imported in to MATLAB and the coordinates can be extracted. However, the quality has to be compromised.

4.3 Experimental results

As described in the algorithm, the slope of the curves may not be constant. To achieve a constant overlap in curved surface, the system should have the capability to move the laser spot in variable in x and y direction to get the same overlap along the length of the curve. Figure 4.6 illustrates the machined complete circle and magnified arc of the circle with zero overlap. It is observed that along the length of the curve the spots are equally distributed.

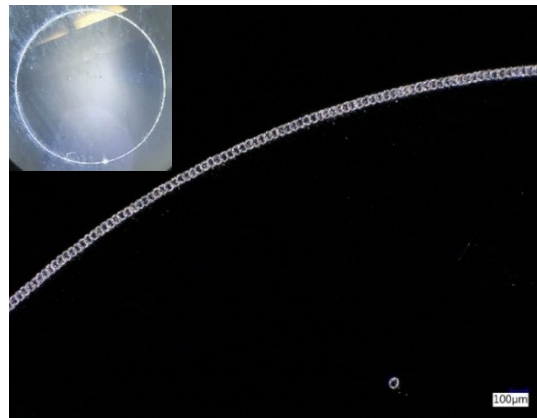


Figure 4.6 Machined circle of 4mm diameter with zero overlap

The circle has constant change in the slope. In order to check the robustness of the algorithm for abrupt changes in the slope, we tried to machine the sinusoidal function with different overlaps. Figure 4.7 shows the machined sinusoidal function with zero overlap. It can be observed that, each spot is equidistant.

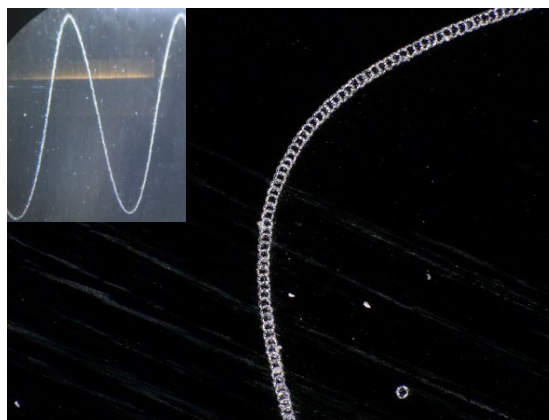


Figure 4.7 Sine wave with a magnified section

The study investigated the function based and image based approaches to evaluate the quality of machining for the curved surfaces. Figure 4.8 and Figure 4.9 show the interferometry images of the machined samples of circle and sinusoidal functions with two different approaches. It can be seen that, in the function based approach the spot of the laser was guided to the exact and accurate position compared to the image based approach therefore it has better quality of machining.

In the function-based approach, the coordinates are derived from the first and second derivative of the functions so the machining is uniform. On the other hand, extracted coordinates from the image-based method depends on the resolution of the image. Higher resolutions can extract the exact coordinates as delivered by function-based approach, but it leads to higher computational cost. The lower resolution results in irregularity of the extracted coordinates. The irregularity in the derived coordinates can be seen in the Figure 4.8(a) and Figure 4.8(b).

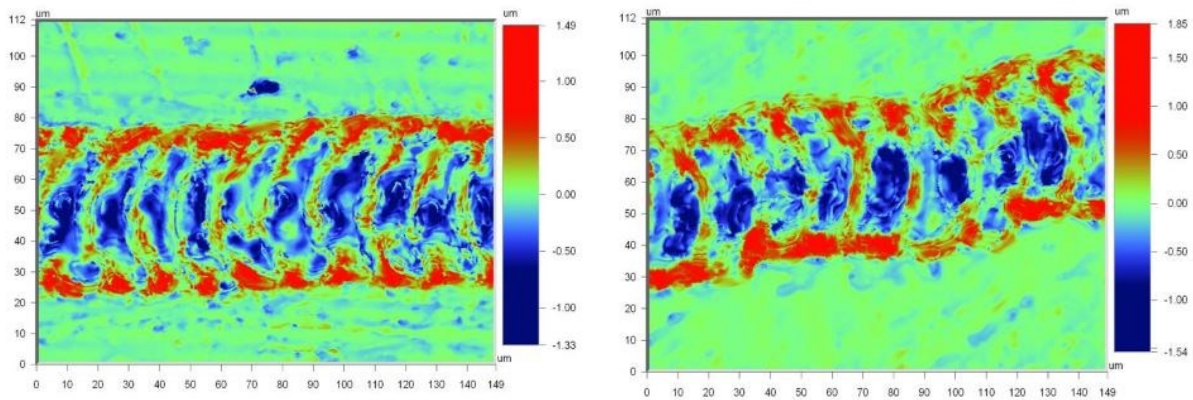


Figure 4.8 Coordinates of the circle - Function based approach (a) & Image based approach (b) with 60% overlap

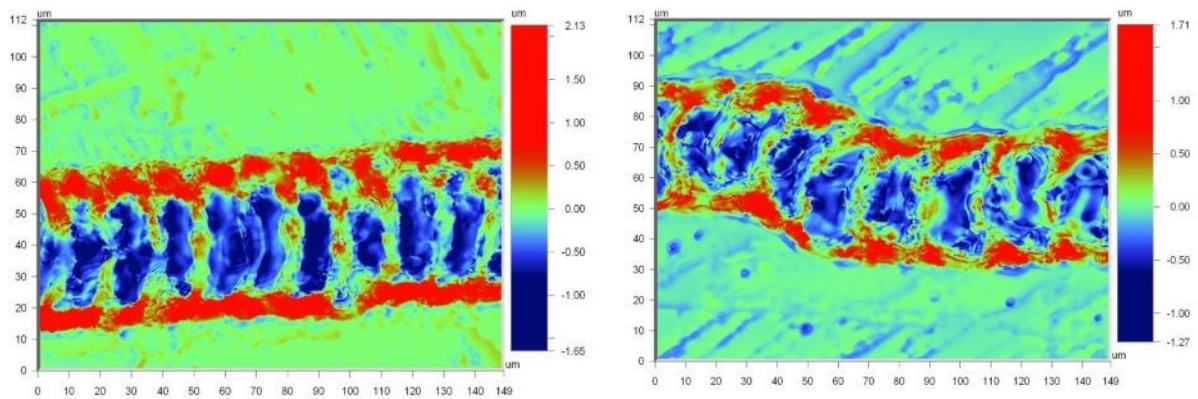


Figure 4.9 Interferometry images of the Sine curve - Function based approach (a) & Image based approach (b) with 60% overlap

The function-based approach is more accurate. In the manufacturing of microfluidic channel, the uniformity and the quality of the path must be precise and controllable. With the presented algorithm, microfluidic channel can be machined with different roughness and depth by varying different process parameters.

From the Figure 4.10 and Figure 4.11 it can be observed that for the same dimensions of the microfluidic channel sample, with zero percent overlap, the extracted coordinates and quality of machining of the function-based approach is uniform. All the laser spots in the function-based approach are perfectly aligned as compared to image-based approach.

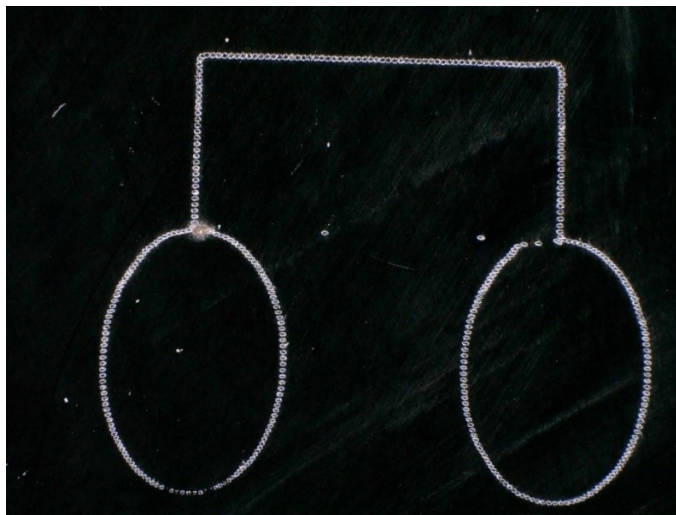


Figure 4.10 Machined microfluidic channel in Image based approach with zero overlap

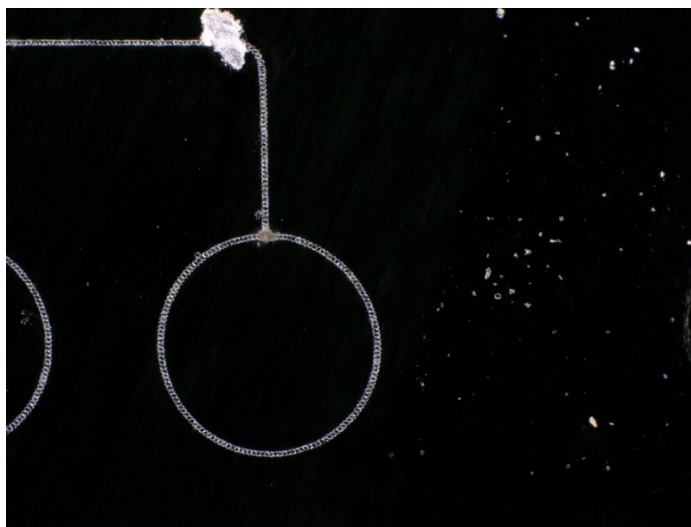


Figure 4.11 Machined microfluidic channel in function based approach with zero overlap

To compare two approaches for the quality of the machining, set of experiments were conducted to machine the curved shapes such as circle and sinusoidal function. The roughness of the machined area is given in the Figure 4.14 and Figure 4.15 for different overlaps (0%, 30% and 60%) for image, and function based approaches. It is observed from the figure that, the approach for finding coordinates does not have significant effect on the roughness due to the constant laser power and repetition rate. The machined sinusoidal functions in 2 different approaches with different percentage overlap are shown in the Figure 4.12 and Figure 4.13.

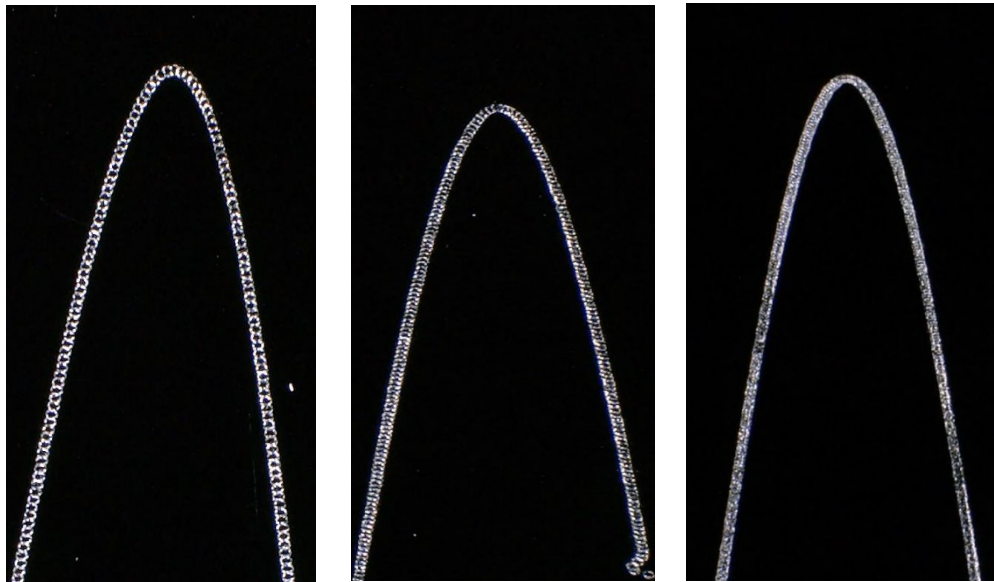


Figure 4.12 Sinusoidal function in Function based approach with (a) 0% overlap (b) 30% overlap and (c) 60% overlap

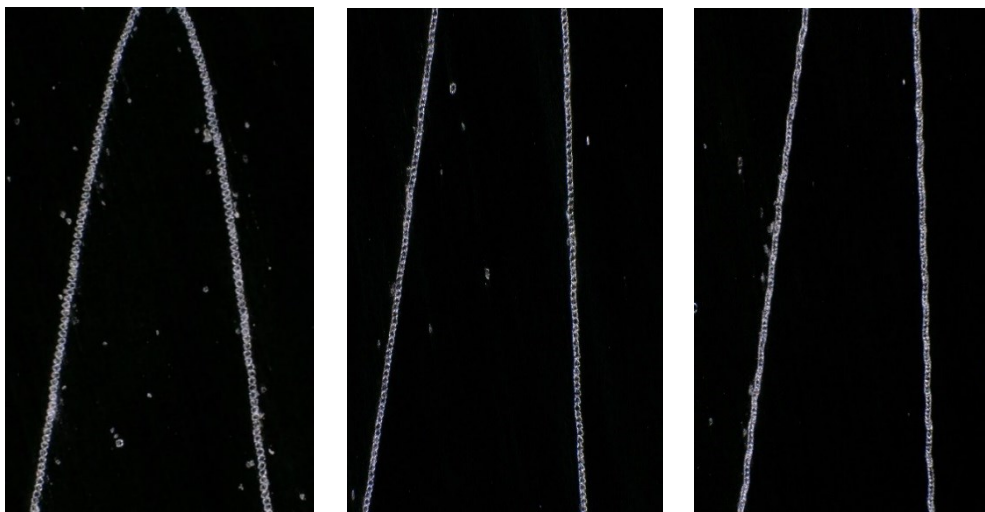


Figure 4.13 Sinusoidal function in Image based approach with (a) 0% overlap (b) 30% overlap and (c) 60% overlap

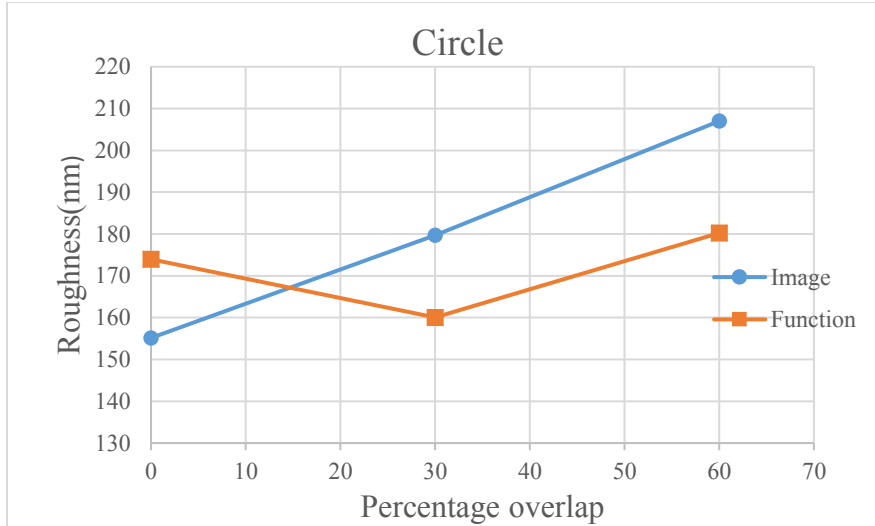


Figure 4.14 Roughness vs percentage of overlap for Circle

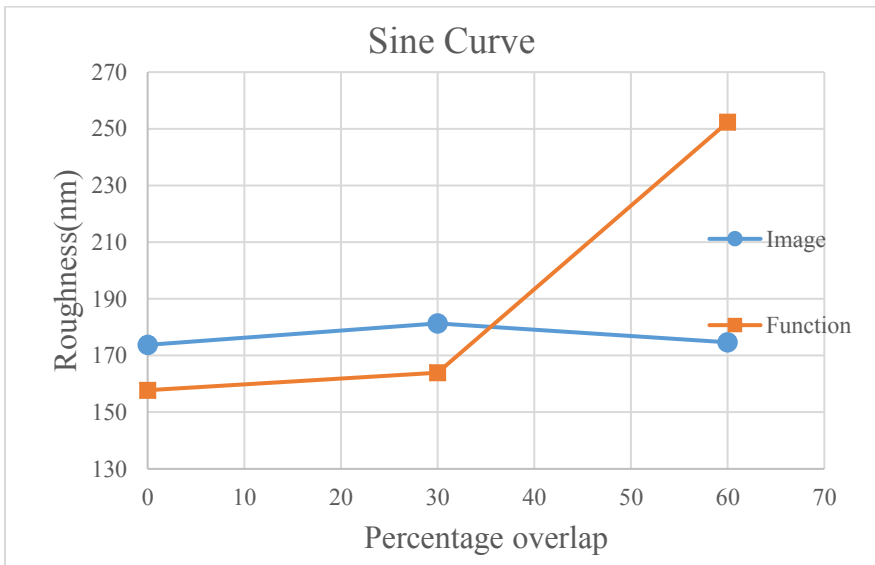


Figure 4.15 Roughness vs percentage of overlap for Sinusoidal function

4.4 Summary

In this chapter, two different coordinate extraction methods for curved surfaces are discussed. A new method of interpolation was proposed to get the equidistant points along the length of the curve. Different examples such as circle and sinusoidal function with different slopes are analysed for coordinate extraction. It can be seen from the results that, the uniformity of the extracted coordinates from the function-based approach is much higher than that of image processing based approach. For precision micro manufacturing of curved shapes, the proposed algorithm provides

excellent results as it is demonstrated by machining a microfluidic channel with different percentage of overlaps. In addition, the study shows that both approaches for coordinate extraction has considerably least or no effect on the roughness of the machined surface. Different process parameters and their effect on roughness of the surface are analysed. With the optimum combination of the different process parameters, required depth and roughness can be achieved.

In the next chapter, an attempt has been made to simulate the texturing of the complex geometry by modelling different process parameters in COMSOL software package and compared with the experimental results.

Chapter 5. Texturing complex geometry – Experiments and Simulation

The effect of the laser and the optomechanical parameters in the micromachining process of the complex geometry is the challenging part in the manufacturing industry due to wide range of materials. There are limited ways to find the best process parameters for machining and texturing with specific depth, thickness and roughness. The COMSOL software was used to model all the laser parameters like laser power, sampling rate, and optomechanical parameters like pulse overlap. Presented simulation demonstrates the roughness, depth and thickness of machined path. In addition, from the simulation point of view, the laser and optomechanical parameters can be optimized for the specific depth and thickness. To validate the numerical model, experiments are conducted for different process parameters by changing the laser power, varying the sampling rate of the laser and data acquisition card, changing the pulse overlap and the results are tabulated. In addition, the same input parameters are given to numerical simulation and the results are in good agreement with experimental outcomes. In conclusion, the simulated model can be used to estimate the effect of the process parameters before the machining. Therefore, the presented model has the control over the machined surface quality and the process can be optimized by giving different material properties in the simulation.

5.1 Finite element simulation

The design of laser micromachining model requires an understanding of laser theory and heat transfer such as conduction and convection. This understanding can be obtained through a reliable simulation. According to the aforementioned, the simulation will calculate the temperature distributions through a defined physical domain while it is exposed to a moving laser beam with known parameters. This will increase understanding of laser heat flow in material processing which in turn will help in prediction and process improvement. The heat conduction principle is considered and solved as the main physics for this problem. Eq. 5.1 presents the dependency between the speed of conduction and the material density, specific heat capacity and thermal conductivity, the difference in temperatures, and the shape of the conductor [59].

$$\rho C_p \frac{\partial T}{\partial t} + \rho C_p u \cdot \nabla T = \nabla \cdot (k \nabla T) + Q \quad \text{Eq. 5.1}$$

where:

Q , k , ρ , C_p , A , T and x are heat, thermal conductivity, density, specific heat capacity, the cross section area of the material, the temperature, the distance between the heat sources, respectively.

Eq.5.1 is solved for its transient response under two different conditions:

- Fixed laser beam with different sampling rates to measure the effect of laser sampling rate and power.
- Moving laser beam with the frequency of 10 KHz with different overlaps along a straight line to measure the effect of overlap on the machining depth and roughness.

40 μm laser spot is considered as a moving heat flux boundary condition with $Q=0$ and Gaussian distribution is assumed for heat flux distribution over the laser spot.

5.2 Physics explanation

The heat transfer in solid module of COMSOL has been used to model the laser ablation in the silicon to provide the transient behaviour. The 2D axisymmetric and 2D models of the physical domain were developed in COMSOL. The investigated geometry is a rectangle with dimensions $0.1\text{mm} \times 0.05\text{mm}$. To define the effect of laser on the sample, the boundary conditions have been defined. The laser beam trajectory of movement has been given as a moving heat source with following equations Eq. 5.2.

$$X_0 = D(1 - Op) \times t [\mu\text{s}] \quad \text{Eq. 5.2}$$

X_0 , D and Op are laser spot position, size and overlap, respectively. All other surfaces have been selected as insulation surfaces.

To simulate the material removal the deformed geometry module was added to the simulation and based on the convection heat flux, the velocity of the meshes that are exposed to the laser heat is defined in the Eq. 5.3.

$$v = \frac{Q}{\rho H_s} \quad \text{Eq. 5.3}$$

where v is the surface normal velocity. ρ and H_s are density and enthalpy of sublimation.

The next step for the simulation part is to define the mesh. In order to, reduce the computational cost and have the best convergence, the meshing procedure is significantly more important than other part of simulation. The finer mesh causes the accurate result but it could cause over estimation at different parts of the sample where there are not any laser spot. On the other hand, the coarse mesh influences the convergence to the inaccurate values. Due to the mentioned reasons, different distribution could be one of the best choices. As the laser spot (heat source) moves on the surface we applied the adaptive mesh, which can change the meshing close to the rapid variation of the heat distribution, based on the step times Figure 5.1 depicts the adaptive mesh distribution at 3 micro second step time. The triangular meshes with maximum element size of 2 micrometre and minimum element size of 7.5 nm have been used with the consideration of adaptive mesh.

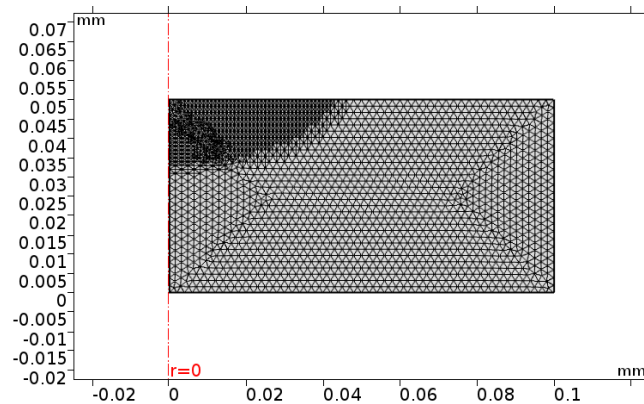


Figure 5.1. Adaptive mesh close to the laser spot at 3 microseconds

5.3 Experimental results

To analyse the effect of different process parameters, a rectangular shape with dimensions of 5mm by 3mm was textured on the silicon wafer specimen. Series of experiments were conducted with different laser power and DAQ sampling rate. We used *WYKO NT1100* white light interferometer to investigate the surface profile of the textured samples. In order to calculate the average surface roughness we measured R_a , which is defined by the arithmetic mean deviation of surface height from mean value, at 5 different points of the textured area (including the four corners and the

centre) and attributed the average of these values to each sample as their Ra. The results are tabulated for roughness values with different percentage of overlaps of laser spot. Set of experiments were conducted with five different laser powers (at 2.9W, 3.1W, 3.68W, 4.57W and 4.87W) and three different percentage overlaps (at 0%, 30% and 60%). The frequency of the DAQ was maintained constant at 10 KHz.

The effect of variation in the laser spot overlap in X direction, Y direction and combination of X and Y, on the average surface roughness (Ra) values are shown in fig 5.2, 5.3 and 5.4 for different laser powers. It has been discussed earlier that the laser spot overlap can be varied in X, Y coordinate axes.

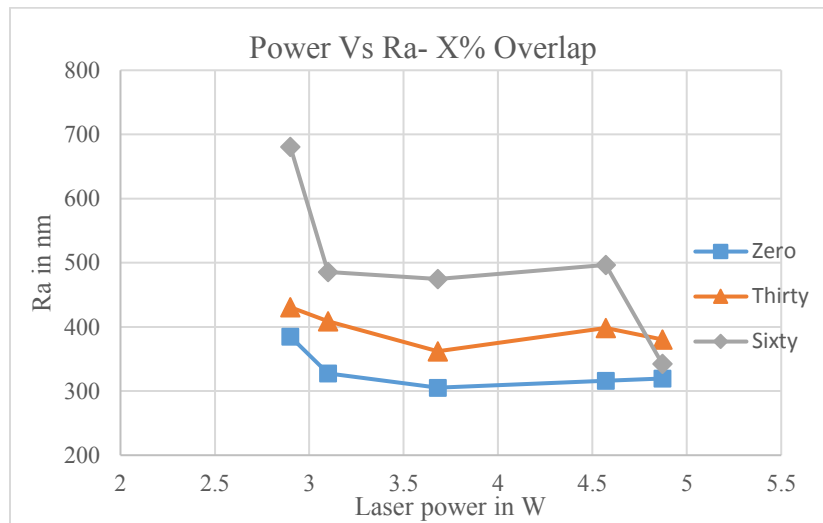


Figure 5.2 Roughness (Ra) Vs Laser power in (W) for different percentage X overlaps at 10 KHz

From the Figure 5.2, it can be observed that, X direction overlap with minimum average power of 2.90W, the roughness is maximum for all three cases. As the laser power increases, the roughness values reduces and reaches a minimum value. For 0% and 30% overlaps, there is no significant reduction in the roughness values. They are almost in the same range throughout the curve. However, for 60% overlap, roughness was 680nm in the beginning at 2.90W and there was a drop in Ra to 342nm at 4.87W. There is almost 50% reduction in the roughness value.

Figure 5.3 shows the roughness values for different percentage overlaps in Y direction for varying average power. For zero overlap, the Ra is minimum in the beginning and it increase to maximum value at 3.1W. Later the trend changes and roughness starts reducing as the laser power increases.

The curve for 30% overlaps maintains a constant trend such that the roughness values decreases with increased laser power. On the other hand, for 60% overlap, roughness slightly increases from 2.90W to 3.1W then it starts decreasing up to 4.57W. There is a sudden increase in the roughness at 4.87W.

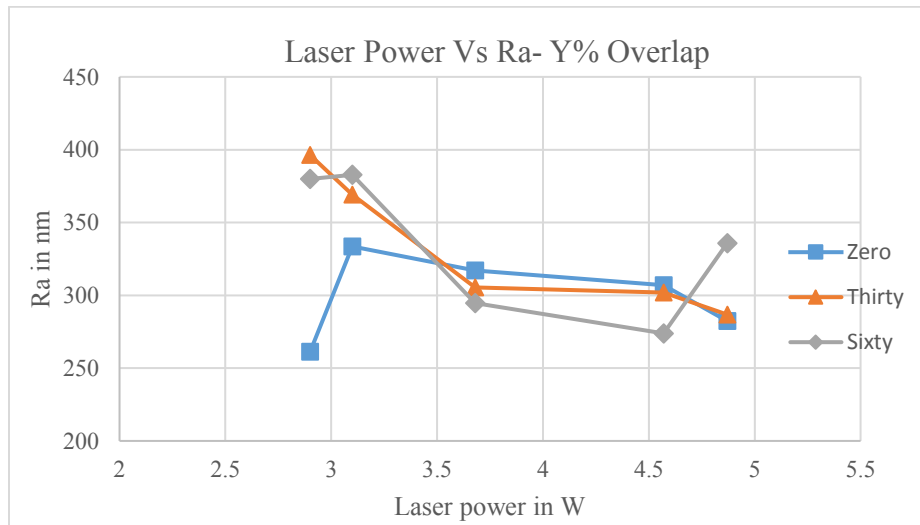


Figure 5.3 Roughness (Ra) Vs Laser power in (W) for different percentage Y overlaps at 10 KHz

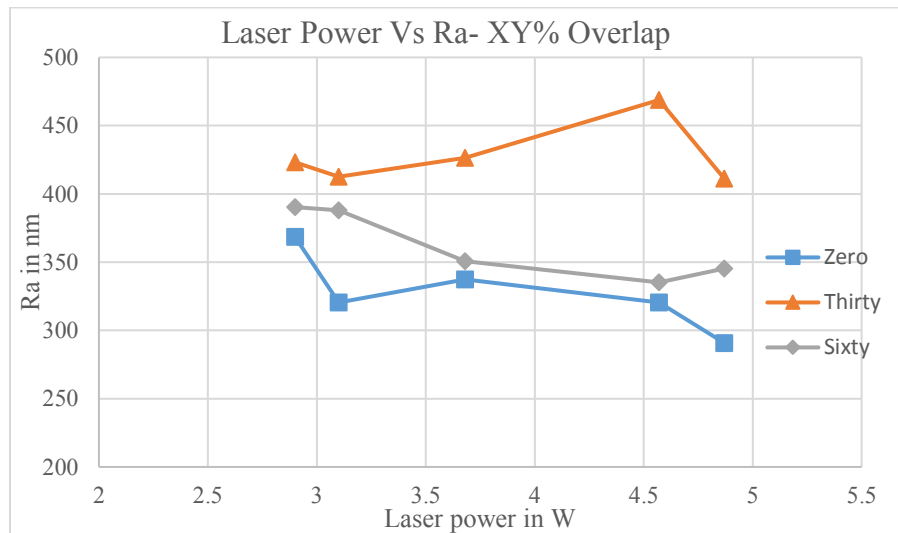


Figure.5.4. Roughness (Ra) Vs Laser power in (W) for different percentage XY overlaps at 10 KHz

Figure.5.4 shows the average roughness values for different percentage overlaps in both X and Y directions for different laser powers. For zero overlap, the roughness is maximum in the beginning and it reduces up to 3.1W. There was a slight increase in the roughness and again it starts reducing and reaches the minimum value. 60% overlap has constant trend of decreased roughness as the

average power increases and there was a slight rise in the roughness at 4.87W power. However, 30% overlap curve follows a different pattern. In the beginning, the roughness is 423nm and there is a slight decrement in the roughness to 412nm at 3.1W then it starts raising and reaches a maximum value of 468nm at 4.57W and again there is a sudden drop in the roughness to 411nm at 4.87W.

In the second set of experiments, the average power of the laser was maintained constant at 3.68W. The sampling rate of the DAQ card was varied for three different overlaps in different coordinate axes and the roughness was measured using the same interferometer.

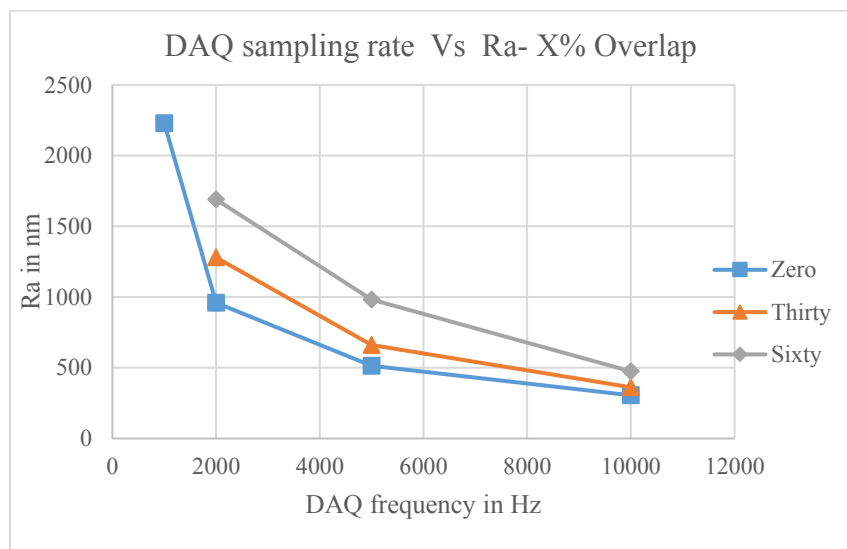


Figure 5.5 Roughness (Ra) Vs DAQ frequency in (Hz) for different percentage X overlaps at 4.8 W laser power

From the Figure 5.5, Figure 5.6 and Figure.5.7, it can be observed that, increase in the sampling rate of the DAQ card reduces the roughness of the surface for different percentage overlaps. Therefore, at parametric combinations of high sampling rate and high percentage overlap helps in uniform removal of material from laser-irradiated surface, which ultimately reduces the surface roughness value.

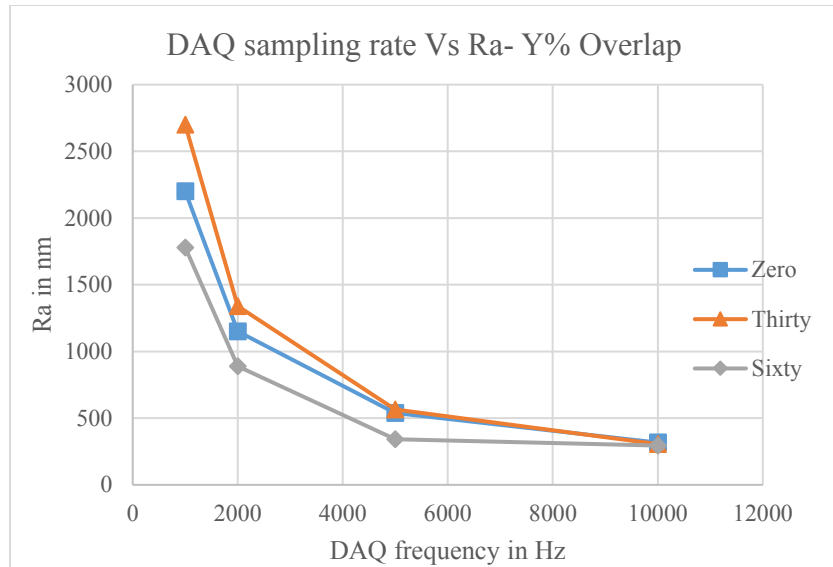


Figure 5.6 Roughness (Ra) Vs DAQ frequency in (Hz) for different percentage Y-overlaps at 4.8 W laser power

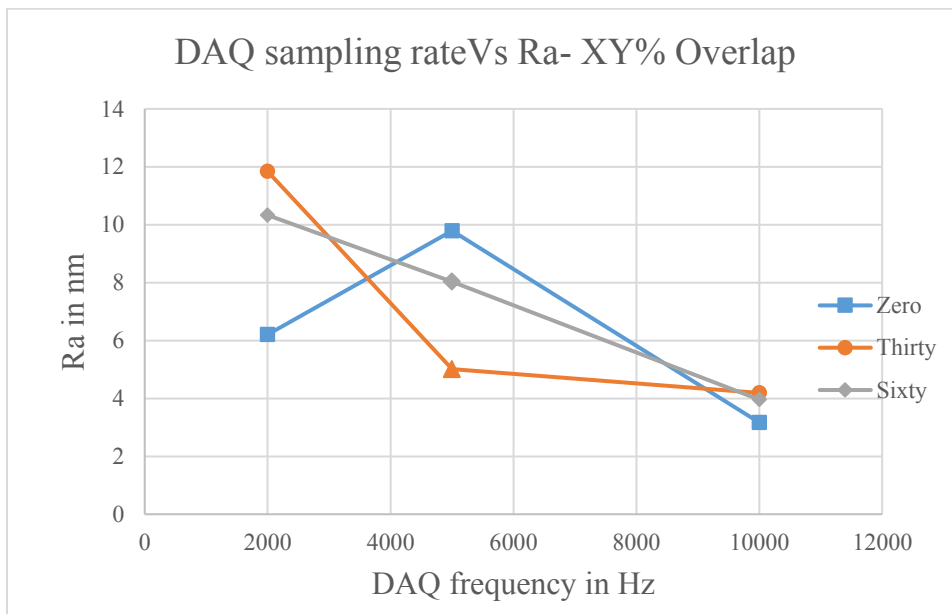


Figure 5.7 Roughness (Ra) Vs DAQ frequency in (Hz) for different percentage XY-overlaps at 4.8 W laser power

Due to high percentage of spot overlap, the material removal from the workpiece surface occurs uniformly throughout the scan area. Therefore, small amount of surface irregularities and roughness is accounted. Furthermore, it is observed from the plots that for any particular value of spot overlap percentage, the surface roughness is more at lower sampling rates. When both the pulse frequency and frequency of the DAQ card are equal at 10 KHz there will be one spot at each point. If the DAQ sampling rate is reduced, the number of spots at each point increases, which

creates uneven removal of material leaving behind the rough surface. Keeping pulse frequency constant, high average power of laser beam causes huge amount of material removal from workpiece surface, causing high depth of machining.

Figure 5.8 and Figure 5.9 shows the image data taken from the Wyko NT1100 Optical Profiling System. The images were captured with a resolution of 640X480. Optical phase-shifting and white light vertical scanning interferometry technique was used to capture the images. The set of data points were extracted from the image, which corresponds to intensity of the reflected light from the sample. When these points are plotted, we got roughness profile. From roughness profile, depth was calculated. Figure 5.8 shows the depth created by single spot of laser for different sampling rates of DAQ. The depth data was taken for 0% overlap with the power of laser maintained at 3.68W. It can be observed from the plot that, as the DAQ frequency increases, the depth of machining decreases. The depth values for different percentage overlaps were also calculated by maintaining the power at 3.68W by varying the DAQ frequency. The results are plotted and analyzed in the Figure 5.10.

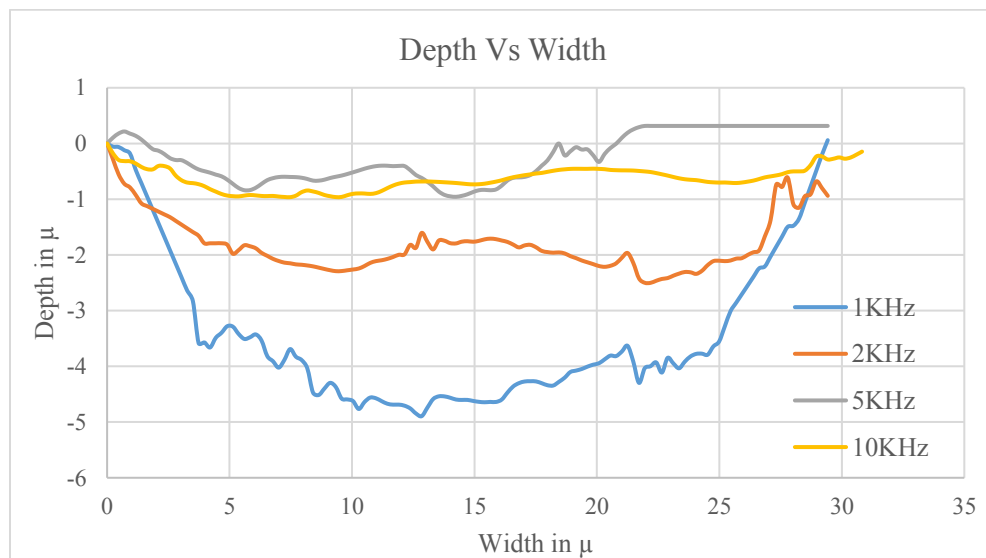


Figure 5.8 Interferometric image data for different DAQ frequency with 0% overlap with Laser power at 3.68W

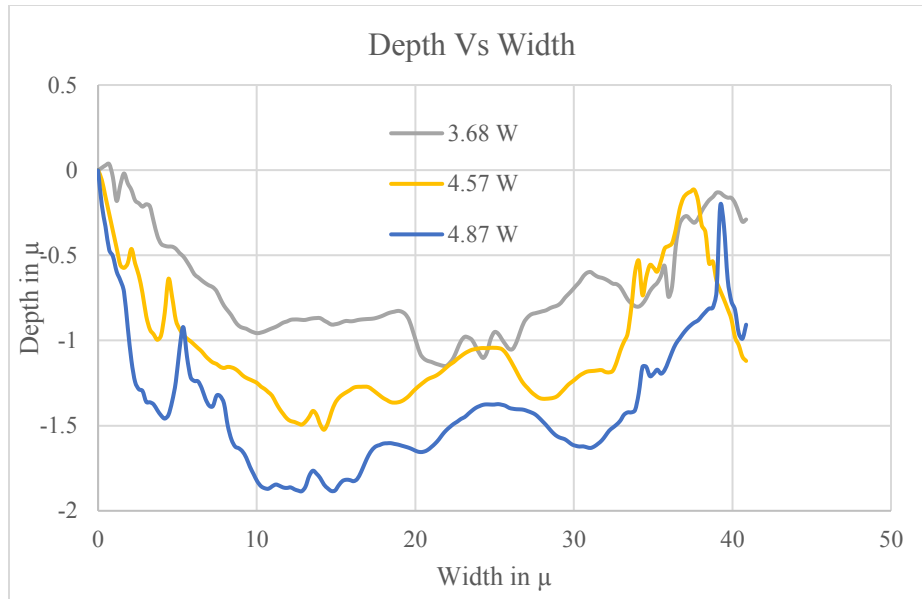


Figure 5.9 Interferometric image data for different laser powers with 0% overlap at 10 KHz DAQ frequency

In the Figure 5.9, depth data of the machined area of single spot of laser for different laser powers are shown. The DAQ frequency was maintained at 10 KHz with 0% laser spot overlap. It is seen from that plot that, increase in magnitude of laser power, increases the depth of machining. Depth values are measured for different laser powers and different percentage of laser spot overlap. The results are plotted in the Figure 5.11 and discussed.

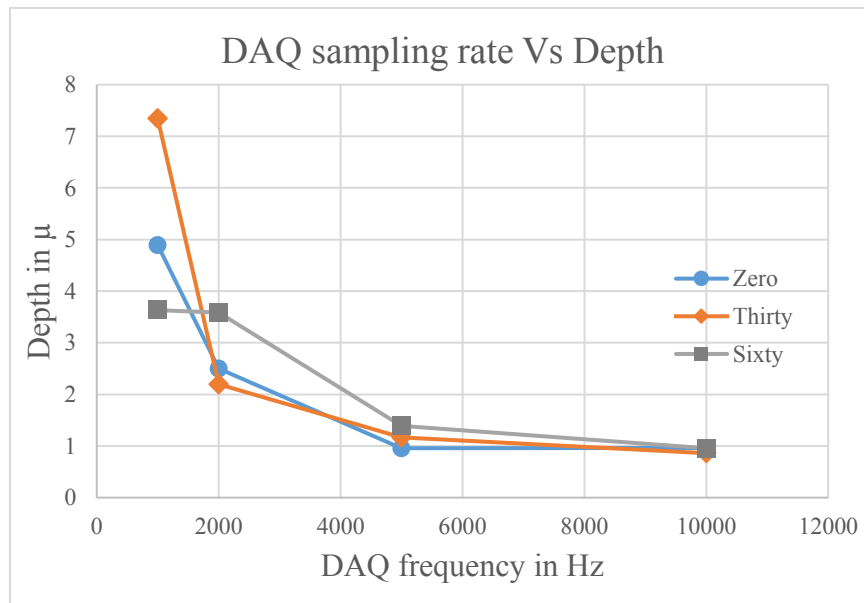


Figure 5.10 Depth (μ) Vs DAQ frequency in (Hz) for different percentage X overlaps at 3.68 W laser power

From the Figure 5.10, it can be observed that, increase in the sampling rate of the DAQ card reduces the depth of machining for different percentage overlaps. Therefore, at parametric combinations of high sampling rate and high percentage overlap helps in uniform removal of material from laser-irradiated surface, which ultimately reduces the surface roughness value. Due to high percentage of spot overlap, the material removal from the workpiece surface occurs uniformly throughout the scan area. Therefore, small amount of surface irregularities and roughness is accounted. Furthermore, it is observed from the plot that, for any particular value of percentage overlap, depth is more at lower sampling rates. When both the pulse frequency and frequency of the DAQ card are equal at 10 KHz there will be one spot at each point. If the DAQ sampling rate is reduced, the number of spots at each point increases, which creates uneven removal of material with larger depths leaving behind the rough surface.

Figure 5.11 shows the variations in the depth values of the machined surface for different magnitudes of power keeping the DAQ sampling rate constant at 10 KHz. It can be observed that, at lower powers the amount of material removal is less for all percentage overlaps. As the laser power increases, the amount of heat flux applied on the sample increases, which increases the ablation tendency of the material results in the increased material removal. At 3.8W power, the depth of machining for zero overlap is 1.14μ . When the power reached maximum value of 4.87W, depth increased to 1.88μ . For 20% variation the laser power there is almost 40% rise in the depth values. If we consider the curve for 30% overlap, the machined surface has the lowest depth value of 0.6μ and as the power increased to maximum, the depth was almost doubled. Therefore, from the results it can be determined that, there is a linear relation between the laser power and depth of micromachining. As the power increases, the depth of machining increases for all percentage overlaps. Keeping pulse frequency constant, high average power of laser beam causes huge amount of material removal from workpiece surface, causing high depth of machining.

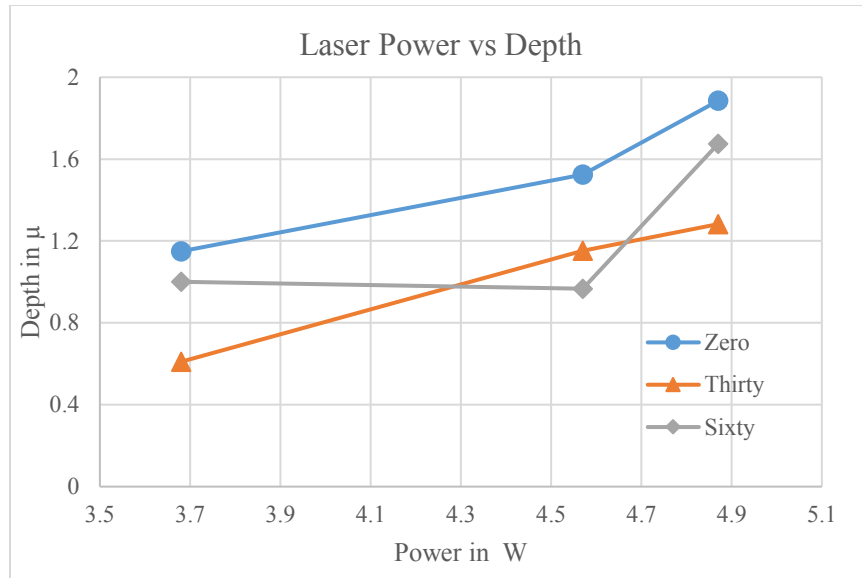


Figure 5.11 Depth (μ) Vs DAQ frequency in (Hz) for different percentage X overlaps with DAQ frequency at 10 KHz

5.4 Simulation results

According to the above mentioned, there are two approaches for the simulation of laser spot:

- 2D axisymmetric: Fixed laser beam with different sampling rates to measure the effect of sampling rate and power
- 2D: Moving laser beam with the frequency of 10KHz with different overlaps along a straight line to measure the effect of overlap on the machining depth and roughness

Figure 5.12 presents the 2D axisymmetric simulation results when the sampling rate and the power are 2000Hz and 4.87W, respectively. As the sampling rate increases the depth of the machined area decreases. Rising the overlap causes more heat flux in specific area, therefore, the depth of the machined area increases when the percentage of overlap increases.

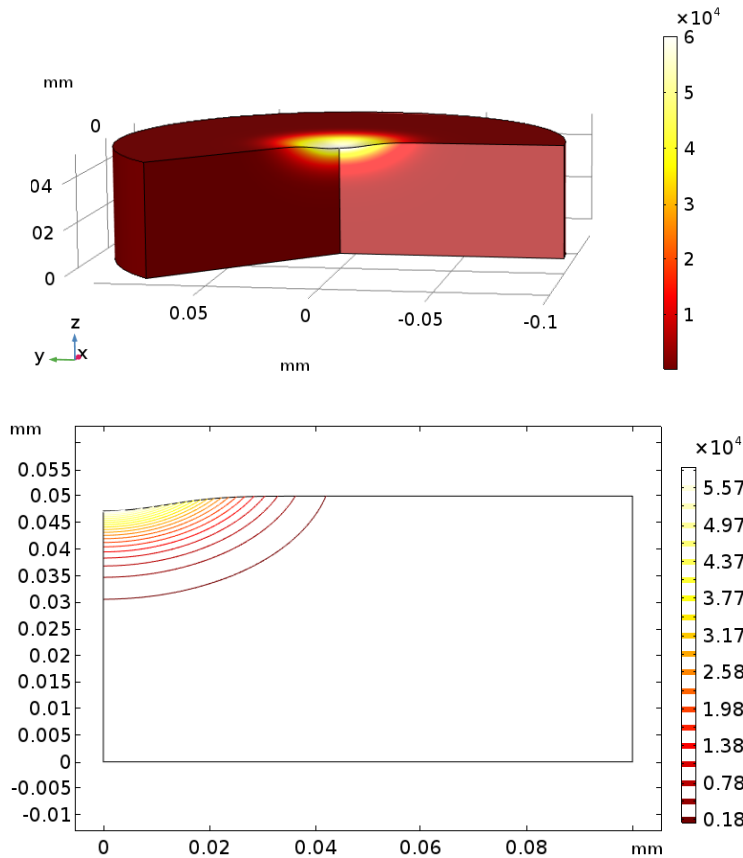


Figure 5.12. 2D Axisymmetric simulation result for 2 KHz and 4.8 W laser power

Figure 5.13 and Figure 5.14 shows the 2D simulation and experimental results for zero overlap with DAQ frequency at 10 KHz and laser power at 4.8W. Figure 5.15 shows the results for the depth measured for the simulation with 1 KHz sampling rate, zero overlap at 4.87W power. To compare the simulation and experiments, the depth of the machined part in the simulation and experiment have been extracted and tabulated in Table 5.1 and Table 5.2 for different laser spot sampling rate and power respectively.

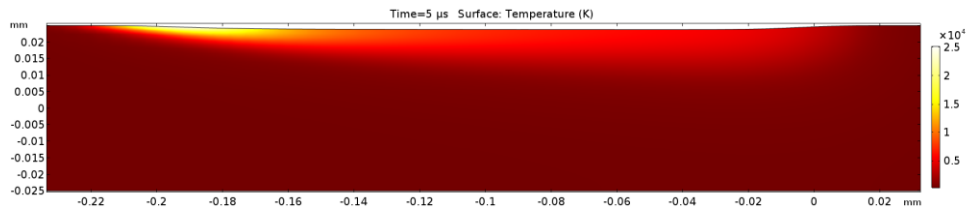


Figure 5.13 2D simulation results of 0 overlap for 10 KHz and 4.8 W laser power

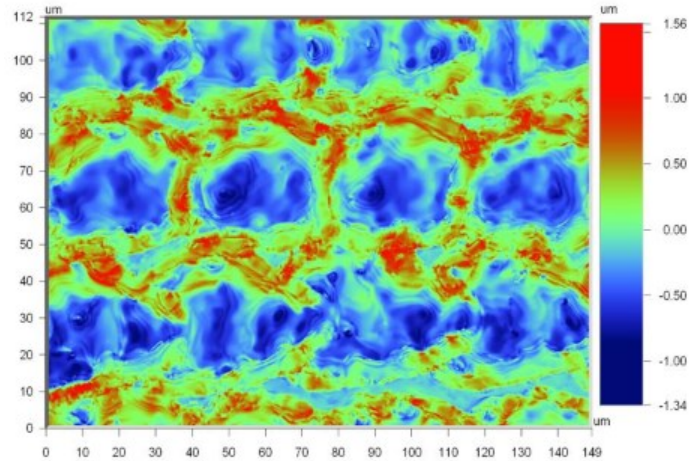


Figure 5.14. Experimental results of 0 overlap for 10 KHz and 4.8 W laser power

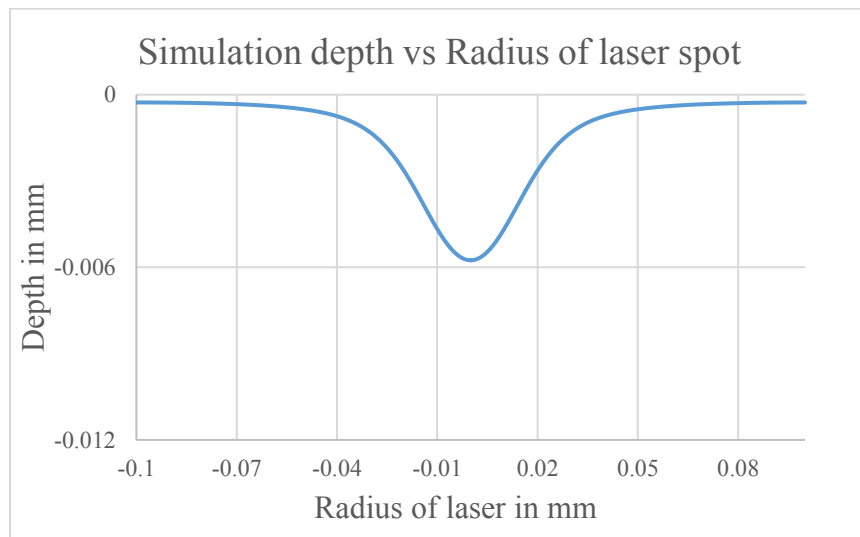


Figure 5.15 Simulation result for depth with 1 KHz sampling rate of laser at 4.87W, 0% overlap

Table 5.1 The depth of machined area for three different sampling rates from the experiment and simulation

Sampling rate (KHz)	Laser pulse depth (experiment)(μ)	Laser pulse depth (simulation)(μ)	% Variation from experiment
1	4.89	5.75	17.58
2	2.74	2.3	16.05
5	0.96	0.72	25
10	1.9	1.3	31.58

Table 5.2 The depth of machined area for three different power from the experiment and simulation with DAQ frequency at 10 KHz

Laser power (W)	Laser pulse depth (experiment)(μ)	Laser pulse depth (simulation)(μ)	% Variation
3.68	1.14	0.9	21.05
4.57	1.52	1.3	14.47
4.87	1.88	1.4	25.53

The comparison of the simulation with the experiment shows that the depth of the machined area is close to each other but still it is not showing the accurate match to the experiments due to the lack of light reflection and scattering consideration and the effect of pulse duration in the simulation. This could also be due the fact that when the depth is higher, the measurement accuracy is limited as to which point we are measuring along the depth.

5.5 Summary

In this chapter, the effect of laser pulse sampling rate and power has been investigated. When the laser power increases the roughness of zero-overlap surface in most of the cases is less than other two overlaps. The increase in laser pulse sampling rate resulted in the reduction of roughness in all cases. However, 60 percent overlap in the direction of y or xy, can make the surface smoother than zero and 30 % overlaps.

The presented simulation in this chapter has modelled the laser pulse as a heat flux. The two different approaches (2D and 2D axisymmetric) are discussed to observe the effect of the sampling rate, power and overlap. As it is presented in table 5.1 and table 5.2, the simulations and the experiment results are showing the same trend in all cases and they are in the same order. However, percentage of relative error is high due to the lack of consideration of optical parameters such as light reflection and scattering in the simulation.

In conclusion, the simulated model can be used to estimate the effect of the process parameters before the machining. So that the presented model has the control over the machined surface quality and the process can be optimized by giving different material properties in the simulation.

Chapter 6. Conclusion and Future Works

The primary objective of this work is to develop a machine vision system for the nanosecond pulsed laser micromachining workstation in the optical metrology and micromachining lab. To perform this task, extensive review of available literature on the evolution of machine vision, different fields related to machine vision, components of machine vision, different types of vision systems, resolution and accuracy requirements, machine vision for manufacturing and inspection, machine vision for laser micromachining are overviewed. The gap in the literature defined our problem and the objectives of this thesis were structured based on the review.

6.1 Conclusion

Experimental setup and major components used for conducting the experiments and their technical details are explained. The design and development of algorithms for laser micromachining and image processing based algorithms are addressed. The description of the total number of experiments that were conducted by varying different process parameters are also explained. There are 117 experiments were conducted in total.

Preliminary results concerned with measurement of the different types of errors that can occur while machining the transformed coordinates are explained. For different movements of the sample in X and Y directions and by rotating the samples, the transitional and angular errors were found out. Three set of experiments were conducted for the displacements and rotations of the samples. The results were plotted for the average of the three values of the errors. The major sources of errors and the probable solutions to overcome the errors are also discussed.

Two different coordinate extraction methods for curved shapes are discussed. A new method of interpolation was proposed to get the equidistant points along the length of the curve. Different examples such as circle and sinusoidal function with different slopes are analysed for coordinate extraction. It can be seen from the results that the uniformity of the extracted coordinates from the function-based approach is much higher than that of image processing based approach. For precession micro manufacturing of curved shapes, the proposed algorithm provides excellent results as it is demonstrated by machining a microfluidic channel with different percentage of overlaps. In addition, the study shows that both approaches for coordinate extraction has

considerably least or no effect on the roughness of the machined surface. Different process parameters and their effect on roughness of the surface are analysed. With the optimum combination of the different process parameters, required depth and roughness can be achieved.

The effect of laser pulse sampling rate and power has been investigated in the COMSOL simulation model. The presented simulation has modelled the laser pulse as a heat flux. The two different approaches (2D and 2D axisymmetric) are discussed to observe the effect of the sampling rate, power and overlap. The simulations and the experimental results have shown the same trend in all cases and they are in the same order. However, percentage of relative error is high due to the lack of consideration of optical parameters such as light reflection and scattering in the simulation. The simulated model can be used to estimate the effect of the process parameters before the machining. Therefore, the presented model has the control over the machined surface quality and the process can be optimized by giving different material properties in the simulation.

6.2 Future Works

While the primary aim of the thesis for the development machine vision assisted laser micromachining, workstation was successfully met. There is lot of potential for future direction of research in this area. Some of which are summarized below.

The developed system can be made online. As seen in the chapter two of the presented work, images were taken before and after the transformation of sample with the usage of beam splitter and screen arrangements. With the available low power laser, it was not possible for us to machine the sample keeping the beam splitter in the same position. There was almost 60% loss in the laser beam energy after the beam splitter. Therefore, with the usage of high power laser, the developed system can be made online and the laser micromachining can be seen on the camera screen, which makes the system more reliable.

Error reduction can be done by implementing few methods such as increasing the contrast of the image to locate the right pixel. Some of the advanced techniques such as automatic edge and corner detection techniques can be used and advanced algorithms can be developed to choose the exactly centre pixel for whatever the manual selection to carry out the same path of machining without

causing error. By using autofocus lens, the depth of focus can be increased automatically which helps in capturing sharp images.

We have the control over the laser spot on the sample. From the experimental results and simulation, we have the relation between the laser power, sampling rate, depth and roughness. There is a scope for the significant improvement in the scanning protocol to be able to machine the 3Dimensional microstructures. Based on the captured images of a 3D structure, the intensity profile can be extracted. With the intensity data, the number of laser pulses to be sent to specific point on the surface for the required depth of machining can be decided by the feedback protocol. The roughness variations can be made by changing percentage overlap of laser spot. One of the potential application where it largely helps in the manufacturing of Micro Electro Mechanical Devices. Keeping this in mind, we tried to machine a microfluidic channel in 2D. It can be advantageous over polymer-based manufacturing in terms of production time. Curing time can be avoided while maintaining the same accuracy of manufacturing.

References

- [1] “visionoverview @ www.bmva.org.” .
- [2] D. Gries and F. B. Schneider, *Texts in Computer Science*, vol. 42. 2010.
- [3] O. Fields, “Machine Vision Background,” pp. 27–50.
- [4] “4a710cf1403b68a3baed15599b2167954c1002f6 @ www.edmundoptics.com.” [Online]. Available: <https://www.edmundoptics.com/resources/application-notes/imaging/camera-types-and-interfaces-for-machine-vision-applications/>.
- [5] “f24bb57c9fdee5df2385ff0bedcb238b791b1726 @ www.teledynedalsa.com.” [Online]. Available: <http://www.teledynedalsa.com/en/learn/knowledge-center/machine-vision-101-an-introduction/>.
- [6] “lighting @ www.cognex.com.” [Online]. Available: <https://www.cognex.com/what-is/machine-vision/components/lighting>.
- [7] “Advantages-of-Pulsing @ www.gardasoft.com.” [Online]. Available: <http://www.gardasoft.com/Glossary-of-Terms/LED-Pulse-and-Strobe-controllers/Advantages-of-Pulsing.aspx>.
- [8] “Introduction To Machine Vision.”
- [9] B. G. Batchelor, *Machine vision handbook*. 2012.
- [10] “03c78e3da99959624e33d21920989e705ac9499c @ www.stemmer-imaging.co.uk.” [Online]. Available: <https://www.stemmer-imaging.co.uk/en/technical-tips/line-scan-cameras/>.
- [11] “Accuracy-Repeatability-and-Resolution-in-Machine-Vision @ blog.xiris.com.” .
- [12] P. Chen, P. Wang, J. Wang, and Y. Yao, “Design and motion tracking of a strip glove based on machine vision,” *Neurocomputing*, vol. 288, pp. 20–29, 2018.

- [13] F. Lahajnar, R. Bernard, F. Pernuš, and S. Kovačič, "Machine vision system for inspecting electric plates," *Comput. Ind.*, vol. 47, no. 1, pp. 113–122, 2002.
- [14] D. M. Bulanon, T. Kataoka, and S. Hata, "Development of a Real-time Machine Vision System for the Apple Harvesting Robot," *Hokkaido Inst. Technol.*, pp. 595–598, 2004.
- [15] C. Bradley and Y. S. Wong, "Surface texture indicators of tool wear - a machine vision approach," *Int. J. Adv. Manuf. Technol.*, vol. 17, no. 6, pp. 435–443, 2001.
- [16] J. C. Su and Y. S. Tarn, "Measuring wear of the grinding wheel using machine vision," *Int. J. Adv. Manuf. Technol.*, vol. 31, no. 1–2, pp. 50–60, 2006.
- [17] A. Mendikute and M. Zatarain, "Automated raw part alignment by a novel machine vision approach," *Procedia Eng.*, vol. 63, pp. 812–820, 2013.
- [18] Y. D. Chethan, H. V Ravindra, and Y. T. Krishne, "ScienceDirect Machined Surface Monitoring in Turning Using Histogram Analysis by Machine Vision," *Mater. Today Proc.*, vol. 5, no. 2, pp. 7775–7781, 2018.
- [19] F. Luk, V. Huynh, and W. North, "Measurement of surface roughness by a machine vision system," *J. Phys. E.*, vol. 22, no. 12, pp. 977–980, 2000.
- [20] Y. D. Chethan, H. V. Ravindra, Y. T. gowda, and S. Bharath Kumar, "Machine Vision for Tool Status Monitoring in Turning Inconel 718 using Blob Analysis," *Mater. Today Proc.*, vol. 2, no. 4–5, pp. 1841–1848, 2015.
- [21] "Lasers_Understanding_the_Basics @ www.photonics.com." [Online]. Available: https://www.photonics.com/a25161/Lasers_Understanding_the_Basics.
- [22] B. N. Chichkov, C. Momma, S. Nolte, F. von Alvensleben, and A. Tünnermann, "Femtosecond, picosecond and nanosecond laser ablation of solids," *Appl. Phys. A Mater. Sci. Process.*, vol. 63, no. 2, pp. 109–115, 1996.
- [23] A. Y. Vorobyev and C. Guo, "Metal colorization with femtosecond laser pulses," no. May 2008, p. 70051T, 2008.

- [24] J. Yao *et al.*, “Selective appearance of several laser-induced periodic surface structure patterns on a metal surface using structural colors produced by femtosecond laser pulses,” *Appl. Surf. Sci.*, vol. 258, no. 19, pp. 7625–7632, 2012.
- [25] T. Yong Hwang *et al.*, “Enhanced efficiency of solar-driven thermoelectric generator with femtosecond laser- textured metals,” *J. Phys. Chem. B Sol. Cells Sci. Sol. Energy Mater. Adv. Mater. (dearf. Beach Fla.) A. Reja R. J. Ram*, vol. 114, no. 7, pp. 14339–14342, 2010.
- [26] L. Yalçın and R. Öztürk, “Performance comparison of c-Si, mc-Si and a-Si thin film PV by PVsyst simulation,” *J. Optoelectron. Adv. Mater.*, vol. 15, no. 3–4, pp. 326–334, 2013.
- [27] T. Yong Hwang *et al.*, “Enhanced efficiency of solar-driven thermoelectric generator with femtosecond laser- textured metals,” *J. Phys. Chem. B Sol. Cells Sci. Sol. Energy Mater. Adv. Mater. (dearf. Beach Fla.) A. Reja R. J. Ram*, vol. 114, no. 7, pp. 14339–14342, 2010.
- [28] A. M. Kietzig, S. G. Hatzikiriakos, and P. Englezos, “Ice friction: The effects of surface roughness, structure, and hydrophobicity,” *J. Appl. Phys.*, vol. 106, no. 2, 2009.
- [29] A. Y. Vorobyev and C. Guo, “Metal pumps liquid uphill,” *Appl. Phys. Lett.*, vol. 94, no. 22, pp. 2007–2010, 2009.
- [30] F. Liang, J. Lehr, L. Danielczak, R. Leask, and A. M. Kietzig, “Robust non-wetting PTFE surfaces by femtosecond laser machining,” *Int. J. Mol. Sci.*, vol. 15, no. 8, pp. 13681–13696, 2014.
- [31] V. Zorba *et al.*, “Biomimetic artificial surfaces quantitatively reproduce the water repellency of a lotus leaf,” *Adv. Mater.*, vol. 20, no. 21, pp. 4049–4054, 2008.
- [32] J. Yang, Y. Yang, B. Zhao, Y. Wang, and X. Zhu, “Femtosecond laser-induced surface structures to significantly improve the thermal emission of light from metals,” *Appl. Phys. B Lasers Opt.*, vol. 106, no. 2, pp. 349–355, 2012.
- [33] E. Fadeeva, S. Schlie, J. Koch, and B. N. Chichkov, “Selective cell control by surface structuring for orthopedic applications,” *J. Adhes. Sci. Technol.*, vol. 24, no. 13–14, pp. 2257–2270, 2010.

- [34] E. Fadeeva *et al.*, “Bacterial retention on superhydrophobic titanium surfaces fabricated by femtosecond laser ablation,” *Langmuir*, vol. 27, no. 6, pp. 3012–3019, 2011.
- [35] J. E. Carey, C. H. Crouch, M. Shen, and E. Mazur, “Visible and near-infrared responsivity of femtosecond-laser microstructured silicon photodiodes,” *Opt. Lett.*, vol. 30, no. 14, p. 1773, 2005.
- [36] K. M. Tanvir Ahmmed, C. Grambow, and A. M. Kietzig, “Fabrication of micro/nano structures on metals by femtosecond laser micromachining,” *Micromachines*, vol. 5, no. 4, pp. 1219–1253, 2014.
- [37] S. . Durbin, A. . Deshmukh, T. . Brooks, and L. . van de Burgt, “Precision laser-based decontamination of microcavities,” *Appl. Surf. Sci.*, vol. 127–129, pp. 810–814, 1998.
- [38] M. S. Amer, M. A. El-Ashry, L. R. Dosser, K. E. Hix, J. F. Maguire, and B. Irwin, “Femtosecond versus nanosecond laser machining: Comparison of induced stresses and structural changes in silicon wafers,” *Appl. Surf. Sci.*, vol. 242, no. 1–2, pp. 162–167, 2005.
- [39] P. Simon and J. Ihlemann, “Machining of submicron structures on metals and semiconductors by ultrashort UV-laser pulses,” *Appl. Phys. a-Materials Sci. Process.*, vol. 63, no. 5, pp. 505–508, 1996.
- [40] J. Li and G. K. Ananthasuresh, “Quality study on the excimer laser micromachining of electro-thermal-compliant micro devices,” *J. Micromechanics Microengineering*, vol. 11, no. 1, pp. 38–47, 2001.
- [41] H. Y. Zheng and T. Lee, “Studies of CO₂ laser peeling of glass substrates,” *J. Micromechanics Microengineering*, vol. 15, no. 11, pp. 2093–2097, 2005.
- [42] A. Mathis *et al.*, “Micromachining along a curve: Femtosecond laser micromachining of curved profiles in diamond and silicon using accelerating beams,” *Appl. Phys. Lett.*, vol. 101, no. 7, 2012.
- [43] N. Rizvi, “Production of novel 3D microstructures using excimer laser mask projection techniques,” *Proc. SPIE*, no. March 1999, 1999.

- [44] S. Ameer-Beg, W. Perrie, S. Rathbone, J. Wright, W. Weaver, and H. Champoux, "Femtosecond laser microstructuring of materials," *Appl. Surf. Sci.*, vol. 127–129, pp. 875–880, 1998.
- [45] S. Rusu, A. Buzaianu, D. G. Galusca, L. Ionel, and D. Ursescu, "Aluminum alloy nanosecond vs femtosecond laser marking," *Bull. Mater. Sci.*, vol. 36, no. 6, pp. 1037–1042, 2013.
- [46] J. Diaci, D. Braun, A. Gorki, and J. Moina, "Rapid and flexible laser marking and engraving of tilted and curved surfaces," *Opt. Lasers Eng.*, vol. 49, no. 2, pp. 195–199, 2011.
- [47] M. F. Chen, W. T. Hsiao, W. L. Huang, C. W. Hu, and Y. P. Chen, "Laser coding on the eggshell using pulsed-laser marking system," *J. Mater. Process. Technol.*, vol. 209, no. 2, pp. 737–744, 2009.
- [48] L. Scime and J. Beuth, "Anomaly detection and classification in a laser powder bed additive manufacturing process using a trained computer vision algorithm," *Addit. Manuf.*, vol. 19, pp. 114–126, 2018.
- [49] M. Grasso, A. G. Demir, B. Previtali, and B. M. Colosimo, "In situ monitoring of selective laser melting of zinc powder via infrared imaging of the process plume," *Robot. Comput. Integr. Manuf.*, vol. 49, no. July 2017, pp. 229–239, 2018.
- [50] Y. Ding, X. Zhang, and R. Kovacevic, "A laser-based machine vision measurement system for laser forming," *Meas. J. Int. Meas. Confed.*, vol. 82, pp. 345–354, 2016.
- [51] M. Schweier, M. W. Haubold, and M. F. Zaeh, "Analysis of spatters in laser welding with beam oscillation: A machine vision approach," *CIRP J. Manuf. Sci. Technol.*, vol. 14, pp. 35–42, 2016.
- [52] A. Müller, S. F. Goecke, P. Sievi, F. Albert, and M. Rethmeier, "Laser beam oscillation strategies for fillet welds in lap joints," *Phys. Procedia*, vol. 56, no. C, pp. 458–466, 2014.
- [53] C. C. Ho, J. J. He, and T. Y. Liao, "On-line estimation of laser-drilled hole depth using a machine vision method," *Sensors (Switzerland)*, vol. 12, no. 8, pp. 10148–10162, 2012.

- [54] M. Nilsen, F. Sikström, A. K. Christiansson, and A. Ancona, "Vision and spectroscopic sensing for joint tracing in narrow gap laser butt welding," *Opt. Laser Technol.*, vol. 96, pp. 107–116, 2017.
- [55] L. Qi, Y. Zhang, S. Wang, Z. Tang, H. Yang, and X. Zhang, "Laser cutting of irregular shape object based on stereo vision laser galvanometric scanning system," *Optics and Lasers in Engineering*, 2015. .
- [56] M. Aghayan, "Laser Surface Texturing of Multicrystalline Silicon to Reduce Solar Weighted Reflectance," no. November, 2015.
- [57] "1be9c2d6a563ec7418d1413377c81b877d178af3 @ impremedia.net." [Online]. Available: <https://impremedia.net/galvano-scer-motor/>.
- [58] L. Production, "100 Optical Profiling System Quantitative 3D Topography for Research and Low-Volume Production," *Production*, pp. 3–4.
- [59] H. Karbasi, A. Learning, and I. Technology, "COMSOL Assisted Simulation of Laser Engraving," 2010. .